Department of Physics and Astronomy
University of Heidelberg

Master Thesis in Physics
submitted by

Patrick Knauer

born in Cambridge (UK)

2021

Automatic mode optimization of an optical resonator via hill climbing

This Master Thesis has been carried out by Patrick Knauer
at the Max Planck Institute for Nuclear Physics in Heidelberg
under supervision of Prof. Dr. José R. Crespo López-Urrutia

Abstract

The ultra-high precision spectroscopy of highly charged ions (HCI) paves way for a new atomic clock standard. To match the larger transition energies in HCI, a near-infrared (NIR) frequency comb operating at 100 MHz is extended into the extreme ultraviolet (XUV) regime via high harmonic generation (HHG) inside a femtosecond-enhancement cavity (fsEC). Large HHG yield is favored by correct coupling of the incident beam to the desired Gaussian mode of the fsEC. Optimal alignment induces a small focus size, reduces residue plasma between pulses, and allows for the desired focus intensity of up to $\sim 10^{14}$ W/cm^2. Manual mode optimization can be time consuming, prone to error, and requires far off-resonance operation. This thesis concentrates on the automatic mode optimization. A hill climb (HC) algorithm is adapted for close to resonance operation and demonstrates intensity gain of up to 300% in less than 100 iterations, while correcting for resonance shifts and successfully depleting higher order transverse electromagnetic modes (TEM) in favor of the desired Gaussian mode.

Zusammenfassung

Die Ultrahochpräzisionsspektroskopie von hochgeladenen Ionen bereitet den Weg für einen neuen Atomuhrstandard. Um die hohen Übergangsenergien der Ionen zu erreichen wird ein Frequenzkamm im nahen Infrarotbereich bei 100 MHz betrieben und per Generation von hohen Harmonischen in einem Überhöhungsresonator in den extrem ultravioletten Bereich erweitert. Eine hohe Ausbeute an hohen Harmonischen wird durch die korrekte Einkopplung des einfallenden Gauß-Strahls in den Überhöhungsresonator begünstigt. Die optimale Justierung führt zu einem kleinen Fokusvolumen, reduziert das Restplasma zwischen aufeinanderfolgenden Pulsen und ist maßgebend für eine Intensität von bis zu 10^{14} W/cm^2 im Laserfokus. Die manuelle Modenoptimierung erfordert Zeit, ist anfällig für Fehler und muss weit von der Resonanzlänge durchgeführt werden. Diese Arbeit konzentriert sich auf die Automatisierung der Spiegelausrichtung. Ein Bergsteigeralgorithmus demonstriert einen Zuwachs in Intensität von bis zu 300% des erwünschten Gauß-Strahls in weniger als 100 Iterationen bei resonanznaher Anwendung.

Contents

List of Figures

List of Tables

1 Motivation

1.1 Fundamental research

Modern physics stands divided between the smallest and largest scales; between the Standard Model (SM) [1], which describes the interactions of the most fundamental particles, and General Relativity (GR) [2] interpreting the interactions that form stars, solar systems, galaxies, and superclusters. Experiments express the success of the SM, by confirming its predictions at high precision. However, evidently a substantial amount of our universe consists of dark matter and dark energy, making up 26% [3] and 69% [4] of our universe, respectively. When it comes to their existence, the SM is incapable of predicting either. Furthermore, the asymmetry between baryonic and antibaryonic matter hints at unexplained interactions tracking back to the early stages of the universe [5], another shortcoming of the SM. As modern physics is unable to describe 95% of what makes up our universe, fundamental research is probing for new physics.

As opposed to collider experiments, which probe for new particles and fields at energies in the range of TeV, high precision spectroscopy is being conducted at small scale. Colliders, such as the Large Hadron Collider (LHC) at CERN, were able to detect and confirm the existence of all particles predicted by the SM, including the finding of the Higgs boson as of lately [6]. On the other hand, table-top experiments, which run at considerably lower energies in the range of eV, can probe for deviations from the SM instead, by studying atomic transitions at high precision. These high precision measurements were enabled by laser technology advances [7, 8].

1.2 Variation of fundamental constants

Paul Dirac was one of the first physicist to consider the variation of fundamental constants in 1937 [9], influenced by Edward Milne's work in 1935 [10]. While the SM declares the values of these fundamental constants as unchanging, the search for unity between the SM and GR led to the rise of theories that propose variation of fundamental constants. A wide range of work was committed to the search of variation: investigating natural nuclear reactors, Big Bang nucleosynthesis, and quasar absorption spectra [11]. The typical candidates for probing of variation are dimensionless constants, as their variation can be distinguished from variation of units. Most noteworthy are the proton-to-electron mass ratio $\mu = m_p/m_e$ and the fine structure constant, with the vacuum permittivity $\in_0$, elementary charge e, Planck constant h, and speed of light c:

$$\alpha = \frac{1}{4\pi \in_0} \frac{e^2}{hc} \tag{1.1}$$

In 2005 analysis of distant quasar spectroscopy led to the proposal of the so-called Australian Dipole [12, 13], which characterizes a spatial variation of the fine structure constant. However, the data largely produced by the Keck telescope and the New Very Large (VLT) telescope is under debate, as systematic errors are suspected to have had influence on the results [14]. Nonetheless, or just because of these debates, laboratory research sparked. As the earth traverses the Australian Dipole, the fine structure constant is expected to vary with time in the laboratory frame. When assuming a stationary dipole with respect to the cosmic microwave background (CMB), a limit to the variation of $\dot{\alpha}/\alpha = 1.35 \times 10^{-18} cos(\psi)$ yr^{-1} can be expected, where ψ is the angle between the motion of our solar system and the dipole [15].

This estimation lies far beyond the fractional uncertainty of the Cs *microwave* frequency standard at 10^{-16} [16], which was used to define the second in 1967. Since then *optical* atomic clocks have overtaken in accuracy and the current most accurate limit to the variation of the fine structure constant was set via quantum logic spectroscopy (QLS) [17] in 2008 by the frequency ratio of Al^+ and Hg^+ [18] with fractional uncertainties of 2.3×10^{-17} and 1.9×10^{-17}, respectively. At this accuracy, measurements over the course of a year resulted in a limit of:

$$\frac{\dot{\alpha}}{\alpha} = (-1.6 \pm 2.3) \times 10^{-17} \text{ yr}^{-1}. \tag{1.2}$$

As it stands, the accuracy of atomic clocks still has room for improvements and fractional uncertainties in the order of 10^{-18} are feasible [19, 20].

1.3 Highly charged ions

The energy dependence of atomic transitions on the variation of the fine structure constant can be quantified by [21]:

$$E = E_0 + q\left[\left(\frac{\alpha}{\alpha_l}\right)^2 - 1\right], \tag{1.3}$$

with the factor q, $E_0 = hf_0$ as the fine structure splitting within one multiplet, and α_l as the laboratory value of the fine structure constant. Frequency variations can thus be linked to the ratio K between the q factor and the frequency f_0 by:

$$\frac{\dot{f}}{f_0} = \frac{2q\ \dot{\alpha}}{f_0\ \alpha_0} \equiv K\frac{\dot{\alpha}}{\alpha_0}. \tag{1.4}$$

As a result, the sensitivity of two atomic transitions to the variation of α strongly relies on the difference in their K factors. This is where the charge state Q of HCI becomes advantageous. At optical transitions, close to the level crossings of HCI [22], the frequency scaling of $f_0 \propto (Q+1)$ is being suppressed. Consequently, the K factor becomes proportional to the charge state [23]:

$$K \propto 2q \propto 2(Q+1)^2. \tag{1.5}$$

Forbidden transitions with long lifetimes provide higher accuracy and can be found in a multitude of HCI. These optical transitions appear at level crossings with near degeneracy. Following these considerations, a range of suitable candidates were proposed [24, 25, 26], including HCI with K factors of several hundreds.

Another advantage is given by the reduced influence of external perturbations on HCI; the few remaining electrons experience increased binding energies and systematical effects, such as Stark shifts and Zeeman shifts, are less impactful [27]. The importance of HCI for a new atomic clock standard was already proposed in 2007 in conjunction with the variation of fundamental constants [28].

1.4 Electron beam ion traps

Despite evident practical challenges, the aforementioned advantages of HCI provoked further studies. The production and manipulation of HCI is far from trivial and calls for a specialized trap. Figure 1.1 depicts a schematic of an electron beam ion trap (EBIT). An EBIT [29] utilizes an electron beam, to strip the injected species of their electrons and trap the produced HCI. This high-intensity electron beam is collimated by a magnetic field, which is produced by two Helmholtz coils. After injection, the beam quickly ionizes the atoms and provides radial confinement for the now positively charged ions. Along the electron beam, the confinement is provided by several drift tubes. As a result, the HCI are heated up to temperature levels of 10^6 K by the electron beam, reproducing conditions usually found in the Sun's corona or solar winds. Spectroscopy of the HCI fluorescence is of high interest, not exclusively for the determination of the charge state. An abundance of ions and their decay channels remain unstudied, which is referred to as the spectral desert [22].

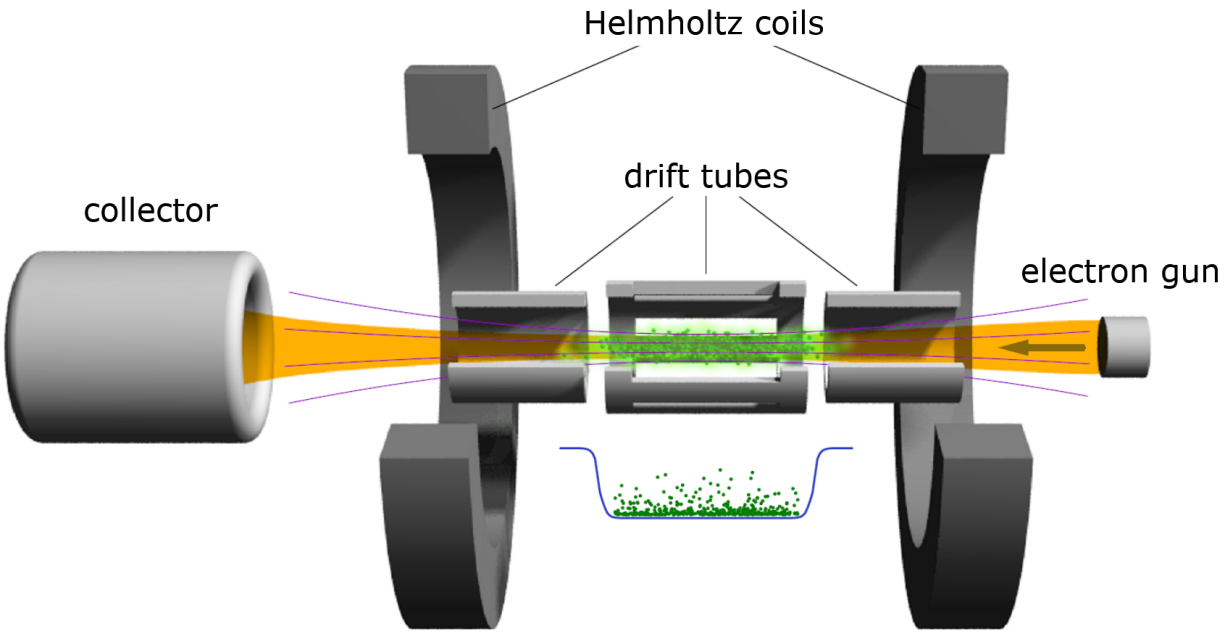

Figure 1.1: *Schematic of an EBIT: Figure from S. Bernitt [30]. The electron beam (yellow), emitted at the electron gun, ionizes atoms (green) at the trap center before it is being absorbed at the collector. Together with the drift tube potential (blue), a radial and axial confinement for the HCI is produced. The beam is collimated by the magnetic field (purple) of two Helmholtz coils.*

Returning to the topic of high precision spectroscopy, these conditions are rather inconvenient. The cooling process is complicated by the scarcity of fast-cycling optical transitions, as standard laser cooling becomes inaccessible for most HCI. However, the Cryogenic Paul Trap Experiment (CryPTEx) [31] presented successful sympathetic cool-

ing of HCI in 2015. CryPTEx accomplished the cooling of a single Ar^{+13} ion by a single Be^{+} ion, achieving a seven-order-of-magnitude decrease in temperature. Furthermore, the Be^{+} ion provides access to QLS. Conclusively, CryPTEx paved way for the promising high precision spectroscopy of HCI and was realized recently, in 2020, via the forbidden optical transition at 441 nm in $^{40}Ar^{13+}$ [32].

1.5 Extreme ultraviolet spectroscopy

As mentioned earlier, optical atomic clocks have overtaken the microwave standard in accuracy. This phenomenon can be tracked back to the so-called Allen deviation σ [33]. The statistical errors that are being accumulated during a Ramsey interrogation scheme of a clock frequency can be quantified by:

$$\sigma = \frac{1}{2\pi\nu_0\sqrt{NT_m t}}, \tag{1.6}$$

where ν_0 is the probed frequency, N the number of uncorrelated atoms, T_m the probe time, and t the total averaging time. The deviation can be suppressed by increasing the number of atoms, the averaging time, and the probe time. While the first two depend on each other, the probe time is limited by the coherence time of the laser or the lifetime of the probed transition. The remaining factor, the transition frequency, is partly responsible for the shift from microwave clocks to optical clocks. Consequently, XUV transitions are expected to outperform both.

Unfortunately, XUV transitions are hard to come by, as most atomic systems are ionized, when exposed to XUV radiation. This leads right back to HCI. Their high charge state results in higher binding energies and XUV transitions become available. Additionally, for the same reason, HCI are not ionized as easily. On the other hand, the technical realization poses multiple challenges. As most matter absorbs XUV radiation, the experimental realization requires a vacuum. To complicate matters, coherent XUV radiation sources are limited. Free-electron lasers and synchrotrons only provide quasi-coherent radiation and the resulting HCI spectroscopy [34, 35, 36] is limited to fractional uncertainties above 10^{-6}.

1.6 Frequency combs

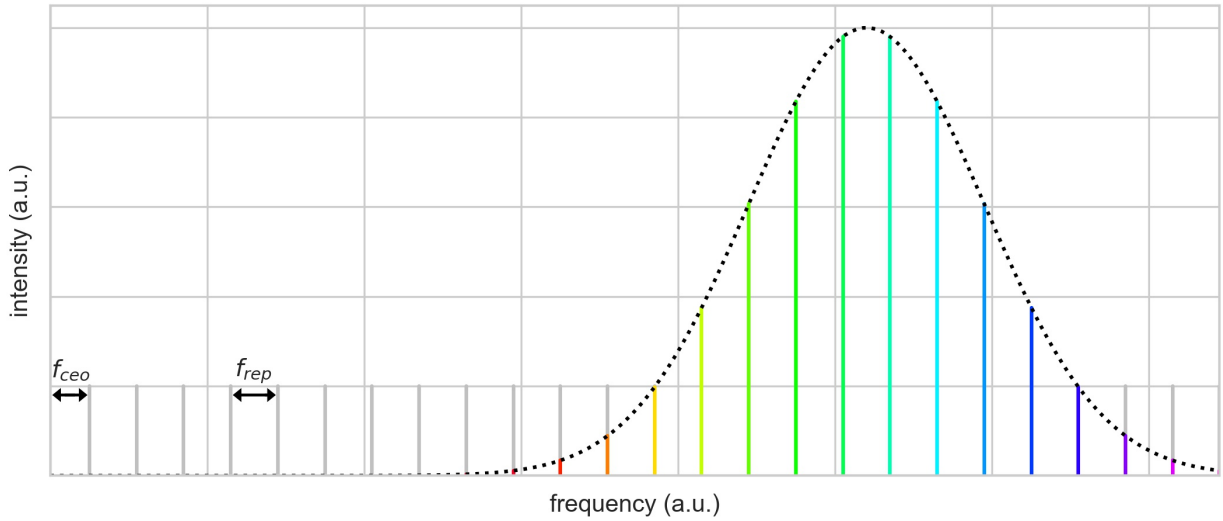

Figure 1.2: *Frequency comb illustration: The frequency spectrum of a frequency comb with marked repetition rate and carrier-envelope offset. The evenly spaced comb teeth provide an optical ruler for absolute and relative high precision measurements.*

The arise of optical atomic clocks transpired hand in hand with advances in laser technology. Pulsed lasers provide an optical measurement tool: so-called frequency combs, which get their name from their comb-like frequency spectrum. Repeated pulses result in evenly spaced teeth in the frequency domain, effectively providing an optical ruler. Each nth tooth can be found via the repetition rate of the pulses f_{rep} and the carrier-envelope offset (CEO) f_{ceo}, which quantifies the phase-slip between subsequent pulses:

$$f_n = n f_{rep} + f_{ceo} \tag{1.7}$$

Early *relative* frequency measurements via pulse trains were already presented in 1970 [37]. However, without control of the carrier-envelope offset, *absolute* measurements remained inaccessible.

This was until in 2000 a new method was presented [38, 39]; utilizing a so-called optical octave, the teeth on the low-frequency end of the spectrum can be compared to the high-frequency end, by means of frequency doubling. This self-referencing technique finally allowed for the extraction and control of the carrier-envelope offset. As time went on, frequency combs were extended far into the XUV regime by a technique called high harmonic generation, which allows for the production of coherent sub 100 nm radiation [40]. Typically, a noble gas injected at the resonators focus point is repeatedly exposed to laser pulses. The Coulomb potential of the atom is being modified during each laser cycle, initially allowing the outer electron to tunnel, to then be accelerated back, and finally recombine with the ion, where coherent high-energy photons are being emitted

[41]. As it stands, XUV frequency combs have the potential to revolutionize frequency metrology and provide an indispensable tool for ultra-high precision spectroscopy.

1.7 Resonator stabilization and alignment

HHG requires high laser power at a focal volume. Pulse amplification can be realized by employing an enhancement cavity, in the scope of this thesis a fsEC [42]. Multiple pulses are being overlapped coherently and the repetition rate determines the optimal resonance length of the longitudinal fsEC modes, while the transverse modes are being controlled by the resonators alignment. Minimal deviations from the resonance length or resonator alignment rapidly eliminate the required enhancement, as subsequent pulses are mismatched and the laser power is shifted to higher modes.

The reflected fsEC signal can be studied, to lock the resonator length. This signal follows a parabolic shape and initially, lasers were locked by operating the resonator length on either side of the resonance [43]. The resulting linear response uncovers the required length correction. With this method operation on resonance is inaccessible, as the linearity of the response signal is lost. Furthermore, intensity fluctuations are not distinguishable from variations in resonator length. Initially, attempts were made to stabilize the intensity separately [44], until an advanced locking technique was published in 1983 [45]. The Pound-Drever-Hall frequency stabilization takes advantage of the beat signal produced by side bands, to recover linearity while operating on resonance and has become state of the art.

Resonator alignment is often controlled manually, by performing beam walks and observing the intra-cavity intensity distribution. Automatic adjustments can save time and provide better alignment. Genetic algorithms [46] and stochastic parallel gradient descents [47] have been shown to actively optimize alignment. Since UHV is required at XUV operation, shortage of space as well as the difficulty of implementing diagnostics complicate the automated adjustment setup and absolute mirror positions become unobtainable. Therefore, a simple but effective position independent search algorithm for transverse resonator alignment is advantageous. In this thesis, the development and implementation of such an algorithm for close to resonance operation is presented.

2 Theoretical background

2.1 Laser pulses and enhancement cavities

2.1.1 Laser pulses

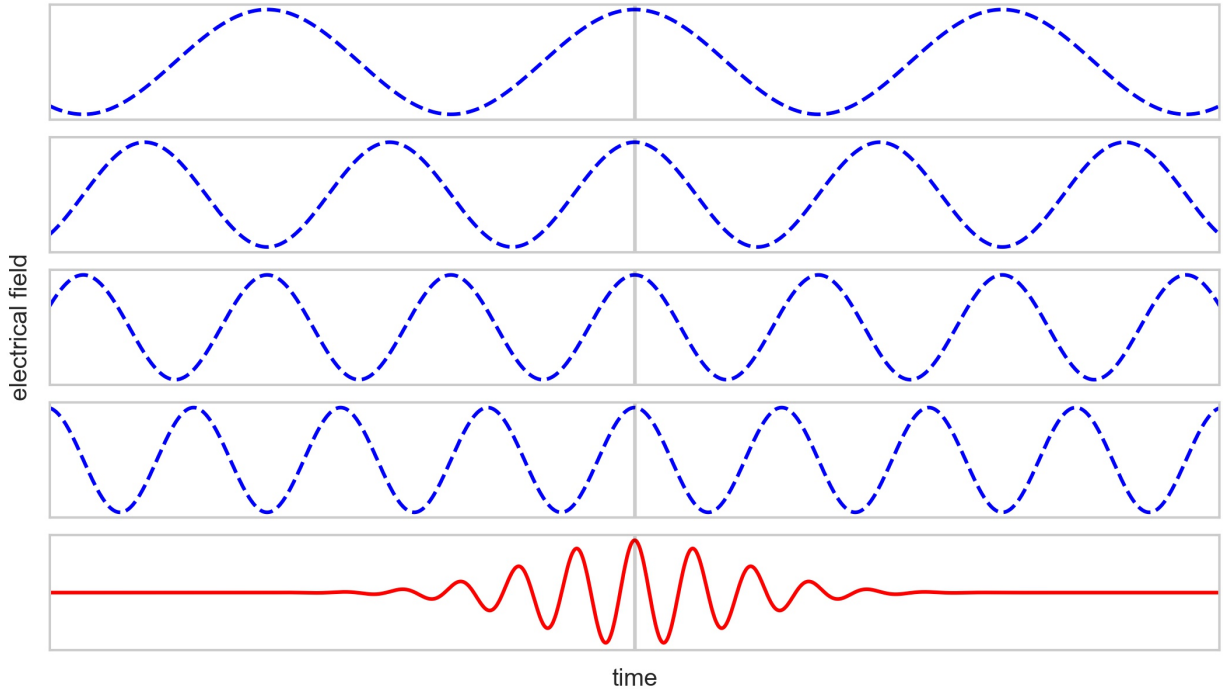

Figure 2.1: *Illustration of superposition of several plane waves producing a pulse: From top to bottom this figure shows four plane waves with decreasing wavelength. Their maxima align at the center. The fifth illustration, in red, depicts a pulse produced by superposition of an infinite amount of plane waves; it consists of a carrier frequency modified by a Gaussian envelope. An intuitive understanding can be acquired, as the constructive interference at the center of the illustration results in a peak for the pulse.*

In order to describe the nature of laser pulses one can start at the electromagnetic wave equation in a vacuum, absent of charges and currents, as obtained from Maxwell's equations in one dimension [48]:

$$\left(\frac{\partial^2}{\partial z^2} - \frac{1}{c^2}\frac{\partial^2}{\partial t^2}\right) E(z,t) = 0. \tag{2.1}$$

This equation describes the change in the electric field $E(z,t)$ along the axis of propagation z at the time t, which travels with the speed of light c. Together with the identical equation for the magnetic field $B(z,t)$ they characterize the propagation of electromagnetic waves in one dimension. The most simple solution, the plane wave, is given by:

$$E(z,t) = A_0\, e^{\,i(\omega t - kz)}, \tag{2.2}$$

where $k = 2\pi/\lambda$ is the wave number with λ as the wavelength, $\omega = ck$ the frequency, and A_0 the amplitude. Furthermore, a sum of solutions to the wave equation provides a new solution. This is known as the superposition principle. A Fourier transform allows a pulse to be described as an integral over many plane waves, each with a distinct frequency. Intuitively, their superposition leads to constructive and destructive interference, which approximates a laser pulse for an infinite amount of superposed frequencies, as illustrated in Figure 2.1. A pulse can be represented by integration as:

$$E_t(z,t) = \frac{1}{2\pi}\int_{-\infty}^{\infty} A(\omega-\omega_c)e^{\,i\omega t}e^{\,-i(k+k_c)z}\,d\omega, \tag{2.3}$$

where ω_c is the central carrier frequency and $A(\omega-\omega_c)$ are the amplitudes of each plane wave. A separation of $A(\omega-\omega_c) = A(\omega)e^{\,i\omega_c t}$ can be made, if the spectral bandwidth is sufficiently small compared to the carrier frequency [49], resulting in:

$$E_t(z,t) = e^{\,i(\omega_c t-k_c z)}\int_{-\infty}^{\infty} A(\omega)e^{\,i\omega t}e^{\,-ikz}\,d\omega = A(z,t)e^{\,i(\omega_c t-k_c z)}. \tag{2.4}$$

Consequently, a pulse consists of a carrier wave and an envelope $A(z,t)$ which determines the pulse shape. The typical pulse shape is Gaussian, that being said other shapes, such as Lorentzian, are also feasible. A Gaussian envelope in the time domain is mapped onto another Gaussian in the frequency domain by a Fourier transform and their relation becomes:

$$A(\omega-\omega_c) = A_0\,\tau\sqrt{\frac{\pi}{4\;ln\;2}}\;\exp\left[-\frac{\tau^2(\omega-\omega_c)^2}{16\;ln\;2}\right], \tag{2.5}$$

$$A(t) = A_0\,\exp\left[-\frac{4\;ln\;2\;t^2}{\tau^2}\right], \tag{2.6}$$

where the pulse duration τ is chosen to equal the full-width half-maximum (FWHM) in the time domain $\tau = 2\sqrt{2\;ln\;2}\sigma$, with σ as the standard deviation.

2.1.2 Frequency combs

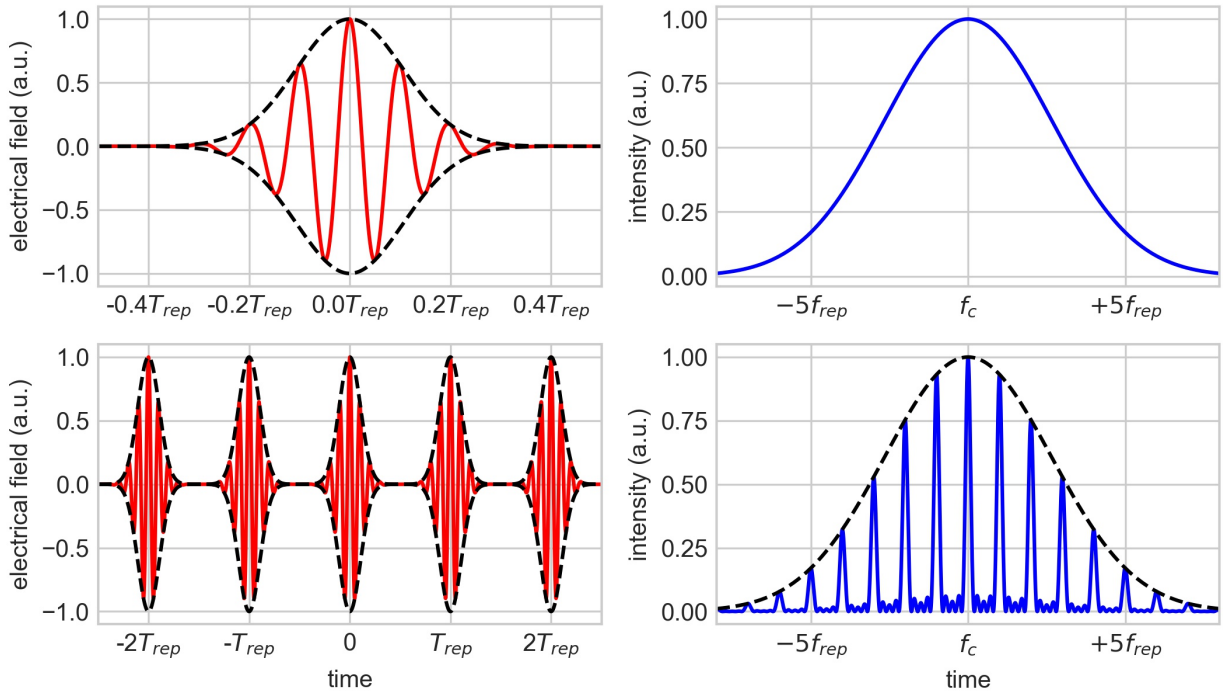

Figure 2.2: *Fourier transform of a single pulse compared to a pulse train: The pulses are depicted in red, the envelopes in black, and the spectra in blue. The pulses are spaced by T_{rep} in the time domain and the comb teeth are separated by $f_{rep} = 1/T_{rep}$ in the frequency domain. As more pulses are added, the comb teeth grow more narrow. In order to achieve a short pulse duration τ the width of the spectrum envelope has to be increased; more available frequencies produce shorter pulses.*

As the fsEC used in this thesis is fed by a pulse train, it is requisite to study the interference of N pulses at a fixed position $z = 0$, spaced by the repetition time T_{rep}, and shifted by the carrier-envelope phase $\Delta\phi_{cep}$ [49]. Accordingly, Equation 2.4 can be summed up to yield the electric field of such a pulse train:

$$E(t) = \sum_{n}^{N-1} A(t - nT_{rep}) \exp[i(\omega_c t - n\omega_c T_{rep} + n\Delta\phi_{cep})]. \tag{2.7}$$

The carrier-envelope phase leads to a shift in phase between the carrier and its envelope, as the name suggests. Therefore, each subsequent pulse increases its offset between carrier maximum and envelope maximum, known as carrier-envelope offset, until they eventually align again at multiple of 2π. After applying the Fourier transform:

$$E(\omega) = \sum_{n}^{N-1} \exp[i\, n(-\omega_c T_{rep} + \Delta\phi_{cep})] \int_{-\infty}^{\infty} A(t - nT_{rep}) \exp[-i(\omega t - \omega_c)]\, dt, \tag{2.8}$$

the following equation is recovered:

$$E(\omega) = A(\omega - \omega_c) \sum_{n}^{N-1} \exp[i\ n(-\omega_c T_{rep} + \Delta\phi_{cep})]. \tag{2.9}$$

Simplifying the sum with the identity $\sum_{n=0}^{N-1} x^n = \frac{1-x^N}{1-x}$ and applying some trigonometric identities yields the intensity spectrum for the pulse train via $I_{pt}(\omega) = |E(\omega)|^2$:

$$I_{pt}(\omega) = |A(\omega - \omega_c)|^2 \ \frac{\sin^2(N(\omega T_{rep} + \Delta\phi_{cep})/2)}{\sin^2((\omega T_{rep} + \Delta\phi_{cep})/2)}. \tag{2.10}$$

To lay this result side by side with a single pulse of sufficiently small bandwidth compared to its carrier frequency, the Fourier transform of Equation 2.4 is calculated as:

$$I_{pulse}(\omega) = |E_\omega|^2 = |\int_{-\infty}^{\infty} E_t(z,t)\ e^{\,-i\omega t}\, dt|^2 = |A(\omega - \omega_c)e^{-ikz}|^2 = |A(\omega - \omega_c)|^2 \tag{2.11}$$

and it can now be seen that for $N = 1$ the spectrum of a single pulse $I_{pt} = I_{pulse}$ is recovered. Consequently, the spectrum of a pulse train consists of an envelope $|A(\omega - \omega_c)|^2$ modified by a periodic function. While the spectrum of a single pulse is continuous, a pulse train forms a sort of "comb" of increasingly narrow lines for $N \to \infty$, as is presented in Figure 2.2. This comb is known as a frequency comb. The repetition rate, which describes the spacing between the teeth of the comb, is given by $f_{rep} = 1/T_{rep}$ and the combs offset, the so-called carrier-envelope offset (CEO) frequency, becomes $f_{ceo} = \Delta\phi_{cep}/2\pi T_{rep}$. Finally the nth comb tooth frequency can be found by applying:

$$f_n = f_{ceo} + n f_{rep}. \tag{2.12}$$

2.2 Resonator optics

2.2.1 Gaussian modes

Consider the plane wave that is traveling along the z direction at $t = 0$:

$$U(\mathbf{r}) = A(\mathbf{r})\exp(-ikz), \tag{2.13}$$

with $A(\mathbf{r})$ as a slowly varying envelope depending on the position $\mathbf{r}$ [48]. Solving the Helmholtz equation $\nabla^2 U + k^2 U = 0$ imposes a restriction on the complex envelope:

$$\nabla^2 A - i2k\frac{\partial A}{\partial z} = 0. \tag{2.14}$$

This can be shown to be solved by the complex envelope of a Gaussian beam as:

$$A(x, y, z) = \frac{A_1}{q(z)}\exp\left(-ik\frac{x^2 + y^2}{2q(z)}\right), \qquad q(z) = z + iz_0, \tag{2.15}$$

with A_1 as a constant and z_0 as the Rayleigh range. This solution resembles a paraboloidal solution with the addition of the imaginary shift in the so-called q-parameter $q(z)$. It also can be expanded to non-Gaussian intensity distributions, that retain their wavefronts, as described by Equation 2.15. The q-parameter is separated in order to describe the beam width and the wavefront radius of curvature. Consider the inverted q-factor $1/q(z) = 1/(z + iz_0)$ which can be rewritten as $1/q(z) = 1/R(z) - i\lambda/\pi W^2(z)$ with $W(z)$ and $R(z)$ as:

$$W(z) = W_0\sqrt{1 + \left(\frac{z}{z_0}\right)^2}, \tag{2.16}$$

$$R(z) = z\left[1 + \left(\frac{z_0}{z}\right)^2\right]. \tag{2.17}$$

Equation 2.16 describes the beam width with the waist radius W_0, while Equation 2.17 describes the wavefront radius of curvature. In order to get a better understanding of their properties and why they describe these features of a Gaussian beam, a look at the intensity distribution of a Gaussian beam is necessary. By inserting Equation 2.15 into Equation 2.2 the following equation is retrieved:

$$U(\mathbf{r}) = \frac{A_1}{iz_0}\frac{W_0}{W(z)}\exp\left[-\left(\frac{\rho}{W(z)}\right)^2\right]\exp\left[-ikz - ik\frac{x^2 + y^2}{2R(z)} + i\arctan\left(\frac{z}{z_0}\right)\right], \tag{2.18}$$

with $\rho = \sqrt{x^2 + y^2}$ as the radius. The intensity calculation $I(\mathbf{r}) = |U(\mathbf{r})|^2$ will cancel the imaginary parts and results in a Gaussian-like intensity distribution perpendicular to the propagation in z direction:

$$I(x, y, z) = I_0\left[\frac{W_0}{W(z)}\right]^2\exp\left[-\frac{2(x^2 + y^2)}{W^2(z)}\right], \tag{2.19}$$

with $I_0 = A_1^2/iz_o^2$ as the complex amplitude. The intensity distribution can be seen in Figure 2.3. At the focus position $z = 0$ the minimal beam size width of W_0 is reached, from which the beam diverges along the optical axis. The beam width follows an hourglass-like shape along the optical axis and approximates a linear function in z for large z. At this point it is important to note that the theoretical intensity distribution in Figure 2.3 remains point symmetric at any distance. Depending on the mirror setup the beam width in the sagittal plane can differ from the tangential plane, leading to astigmatism. The bow-tie resonator used for this thesis focuses the beam at an angle and compensates the resulting astigmatism to produce a point symmetric intensity distribution at the focus position. This leads to distorted images in the observational plane and the transmitted intensity distribution appears oval at a distance. The integra-

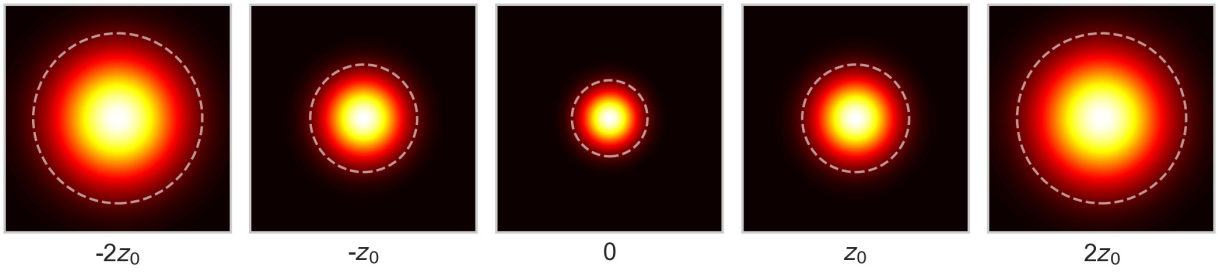

Figure 2.3: *Gaussian beam intensity distribution along the optical axis in units of the Rayleigh range: The dashed circles depict the beam width $W(z)$, which becomes the beam waist W_0 at $z = 0$. Within the dashed line approximately 86% of the beam power is located.*

tion over the intensity distribution from $\rho = 0$ to $\rho = \infty$ results in the beam power of $P = \frac{1}{2} I_0(\pi W_0^2)$. Consequently, the normalized integration up to ρ_0 can now be calculated as:

$$\frac{1}{P} \int_0^{\rho_0} I(\rho, z) 2\pi\rho d\rho = 1 - \exp\left[-\frac{2\rho_0^2}{W^2(z)}\right]. \tag{2.20}$$

Coming back to the beam width from Equation 2.16, it is now trivial to show that within a radius of $\rho_0 = W(z)$ approximately 86% and within a radius of $1.5W(z)$ almost 99% of the beam power of a Gaussian beam is located, which is why $W(z)$ is referred to as the beam width. Another look at Equation 2.18 reveals the phase of the Gaussian beam as:

$$\phi(\rho, z) = kz - \chi(z) + \frac{k\rho^2}{2R(z)}, \qquad \chi = \arctan\left(\frac{z}{z_0}\right). \tag{2.21}$$

It consists of the phase of a plane wave, a phase retardation χ along the z direction, and the wavefront radius of curvature. The phase retardation shifts the phase from $-\pi/2$ to $\pi/2$. This effect can be seen in Figure 2.4 and is called Gouy effect. The third component of Equation 2.21 depends on ρ and is only non-zero off axis. It describes the bending of the wavefronts perpendicular to the beam propagation, as shown in Figure 2.5. At $z = 0$ the Gaussian beam wavefront resembles that of a plane wave, while for increasing z the wavefronts behave like spherical waves. Due to this property, the Gaussian

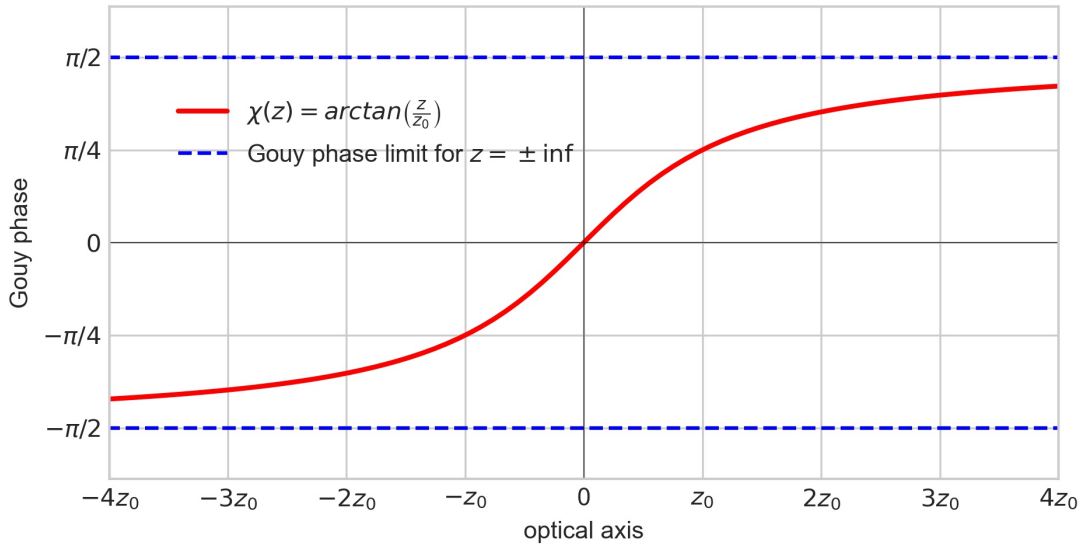

Figure 2.4: *Gouy effect: The phase shift reaches $\pm\pi/4$ at the Rayleigh range. For $z = \pm\infty$ the Gouy phase shift approaches its limit of $\pm\pi/2$.*

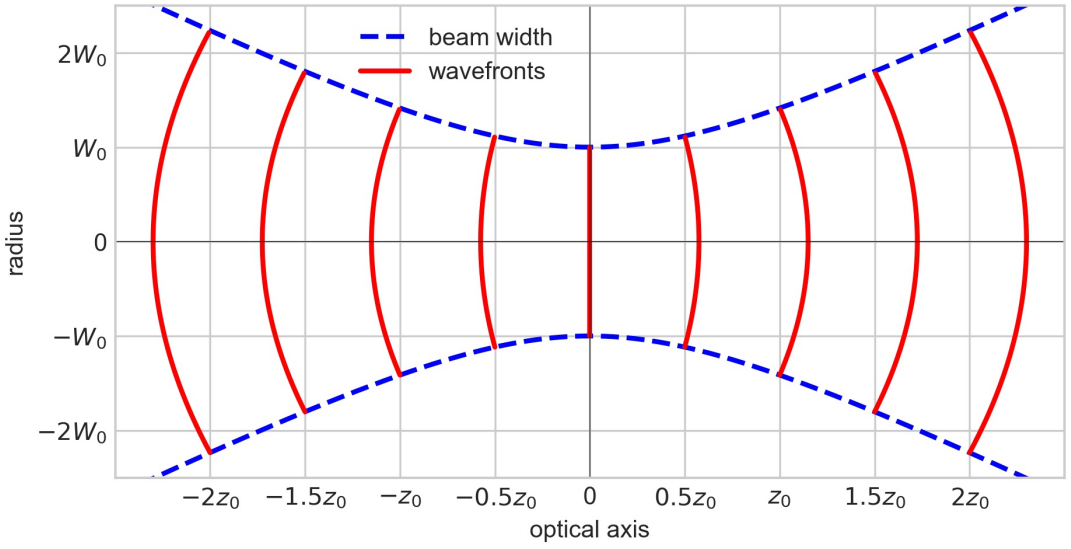

Figure 2.5: *Gaussian beam wavefronts for $k = 0.3z_0$: At $z = 0$ the wavefront resembles a plane wave, while for higher z the wavefront curvature becomes spherical. Consequently, a spherically curved mirror can match the wavefronts in good approximation.*

wavefronts can match the curvature of spherical mirrors and can reproduce themselves between them, laying the basis for optical resonators. As mentioned prior, not exclu-

sively Gaussian beams posses the ability to reproduce and result in so-called resonator eigenmodes, also referred to as modes. Solutions to the Helmholtz equation which share this wavefront behavior but exhibit non-Gaussian intensity distributions are also able to build modes in a resonator. This applies for example to Bessel, Hermite-Gaussian and Laguerre-Gaussian beams. The next chapter will focus on Hermite-Gaussian beams, considering their relevance in the scope of this thesis. While Laguerre-Gaussian beams result from cylindrical symmetry, Hermite-Gaussian beams are found when solving the Helmholtz equation for Cartesian symmetry.

2.2.2 Hermite-Gaussian modes

To further investigate Hermite-Gaussian modes, consider the modulated Gaussian beam A with the Gaussian envelope A_G from Equation 2.15:

$$A(x,y,z) = \ \alpha\left[\sqrt{2}\frac{x}{W(z)}\right]\ \beta\left[\sqrt{2}\frac{y}{W(z)}\right]\exp(i\ \gamma(z)\ )A_G(x,y,z), \tag{2.22}$$

where α, β, and γ are real functions [48]. Since $\gamma(z)$ is independent of ρ, the same wavefront radius of curvature from Equation 2.17 appears in this modulated Gaussian, which in return implies that this beam is able to produce resonator modes. Inserting this function into the Helmholtz equation leads to:

$$\frac{1}{\alpha}\left(\frac{\partial^2\alpha}{\partial u^2} - 2u\frac{\partial\alpha}{\partial u}\right) + \frac{1}{\beta}\left(\frac{\partial^2\beta}{\partial v^2} - 2v\frac{\partial\beta}{\partial v}\right) + kW^2(z)\frac{\partial\gamma}{\partial z} = 0, \tag{2.23}$$

where for simplicity x and y were replaced by the dimensionless variables $u = \sqrt{2}x/W(z)$ and $v = \sqrt{2}y/W(z)$, respectively. Each term of Equation 2.23 has its own independent variable and a separation of variables can be applied, which yields three differential equations:

$$-\frac{1}{2}\frac{d^2\alpha}{du^2} + u\frac{d\alpha}{du} = \mu_1\alpha, \tag{2.24}$$

$$-\frac{1}{2}\frac{d^2\beta}{dv^2} + v\frac{d\beta}{dv} = \mu_2\beta, \tag{2.25}$$

$$z_0\left[1 + \left(\frac{z}{z_0}\right)^2\right]\frac{d\gamma}{dz} = \mu_1 + \mu_2, \tag{2.26}$$

where the constants μ_1 and μ_2 are chosen to simplify later calculations. The first two differential equations are solved by Hermite polynomials, hence the name of the modes. For the first differential equation, these are be given by:

$$H_n(u) = (-1)^n\exp(u^2)\frac{d^n}{du^n}\exp(-u^2), \qquad n = 0,1,2,... \tag{2.27}$$

The first four polynomials are $H_0(u) = 1$, $H_1(u) = 2u$, $H_2(u) = 4u^2 - 2$, and $H_3(u) = 8u^3 - 12u$. In similar fashion, the second differential equation is solved by Hermite polynomials, by replacing u and n with v and m. Now, $\mu_1 = n$ and $\mu_2 = m$ can be substituted, allowing for the last differential equation to be solved via integration, which yields $\gamma = (l+m)\chi(z)$. Inserting and rearranging the results into the initial Equation 2.22 finally gives rise to the Hermite-Gaussian beam equation:

$$U_{nm} = A_{nm}\left[\frac{W_0}{W(z)}\right]G_n\left[\frac{\sqrt{2}x}{W(z)}\right]G_m\left[\frac{\sqrt{2}y}{W(z)}\right]\exp[i\phi_{nm}], \tag{2.28}$$

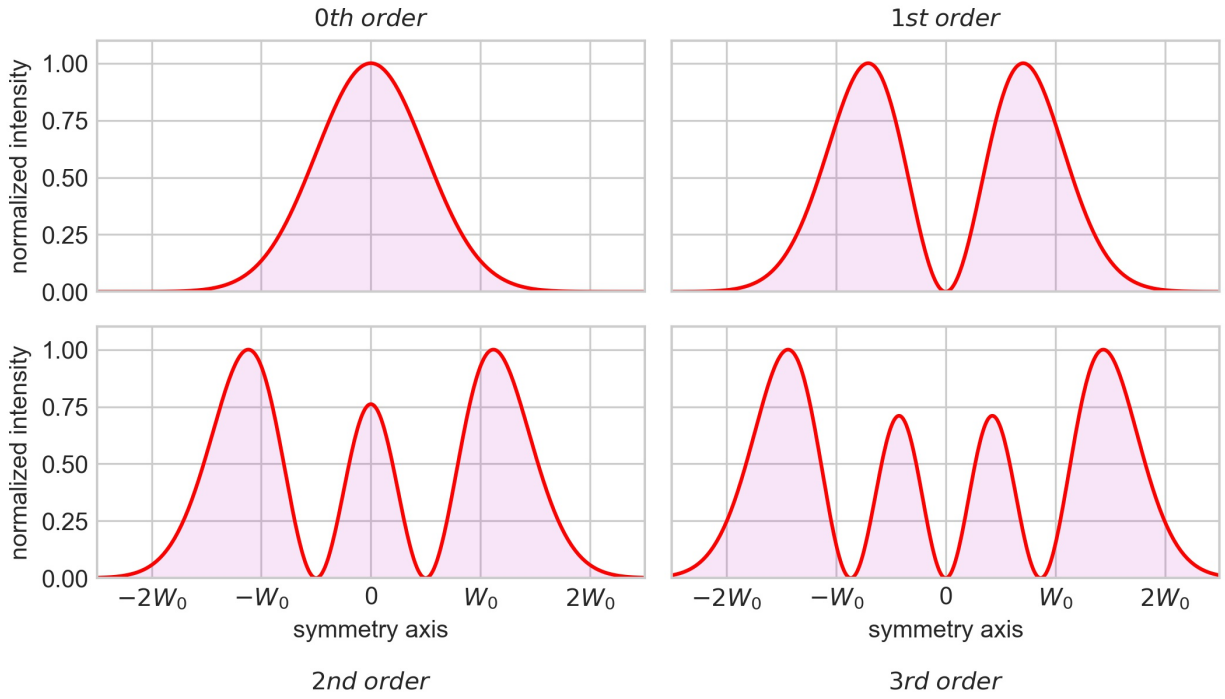

Figure 2.6: *Normalized intensity of a Hermite-Gaussian beam along one of its symmetry axes for $W_0 = z_0 = A_{nm} = 1$: The intensity distribution drastically deviates from the Gaussian beam for higher orders, while the wavefront curvature stays the same. Note that the normalization hides the intensity maxima decrease for increasing orders. The integrated beam power does not change.*

with the phase:

$$\phi_{nm} = -kz - \frac{k\rho^2}{2R(z)} + (n + m + 1)\chi, \tag{2.29}$$

the amplitude A_{nm}, and the Hermite-Gaussian equations for n and m:

$$G_n(u) = H_n(u)\exp\left(\frac{-u^2}{2}\right), \tag{2.30}$$

$$G_m(v) = H_m(v)\exp\left(\frac{-v^2}{2}\right). \tag{2.31}$$

This group of modes is referred to as transverse electromagnetic modes and often denoted as TEM_{nm}. The Gaussian mode is a transverse electromagnetic mode of order $(n, m) = (0, 0)$ or TEM_{00}, since for the order $n = m = 0$ the Gaussian mode is recovered. The higher orders result in $G_1(u) = 2u\ \exp(-u^2/2)$, $G_2(u) = (4u^2 - 2)\ \exp(-u^2/2)$, and so on. The intensity distribution for different Hermite-Gaussian beam modes can be

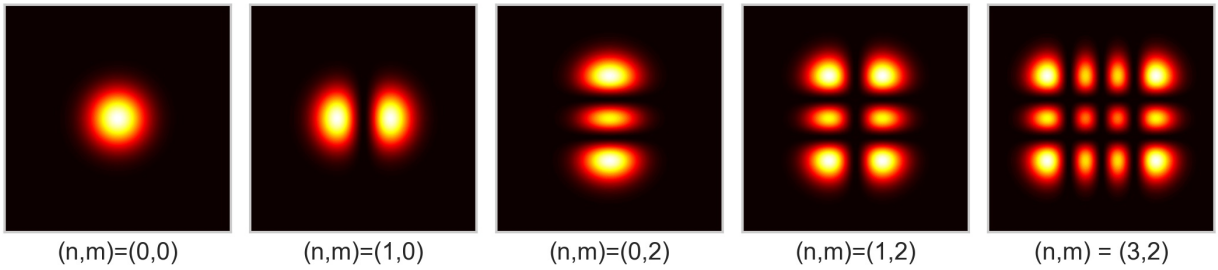

Figure 2.7: *Hermite-Gaussian beam intensity distribution for different orders* (n, m).

seen in Figure 2.6 and Figure 2.7, and is calculated via:

$$I_{nm}(x, y, z) = |A_{nm}|^2 \left[\frac{W_0}{W(z)}\right]^2 G_n^2 \left[\frac{\sqrt{2}x}{W(z)}\right] G_m^2 \left[\frac{\sqrt{2}y}{W(z)}\right]. \tag{2.32}$$

2.2.3 Resonance frequencies

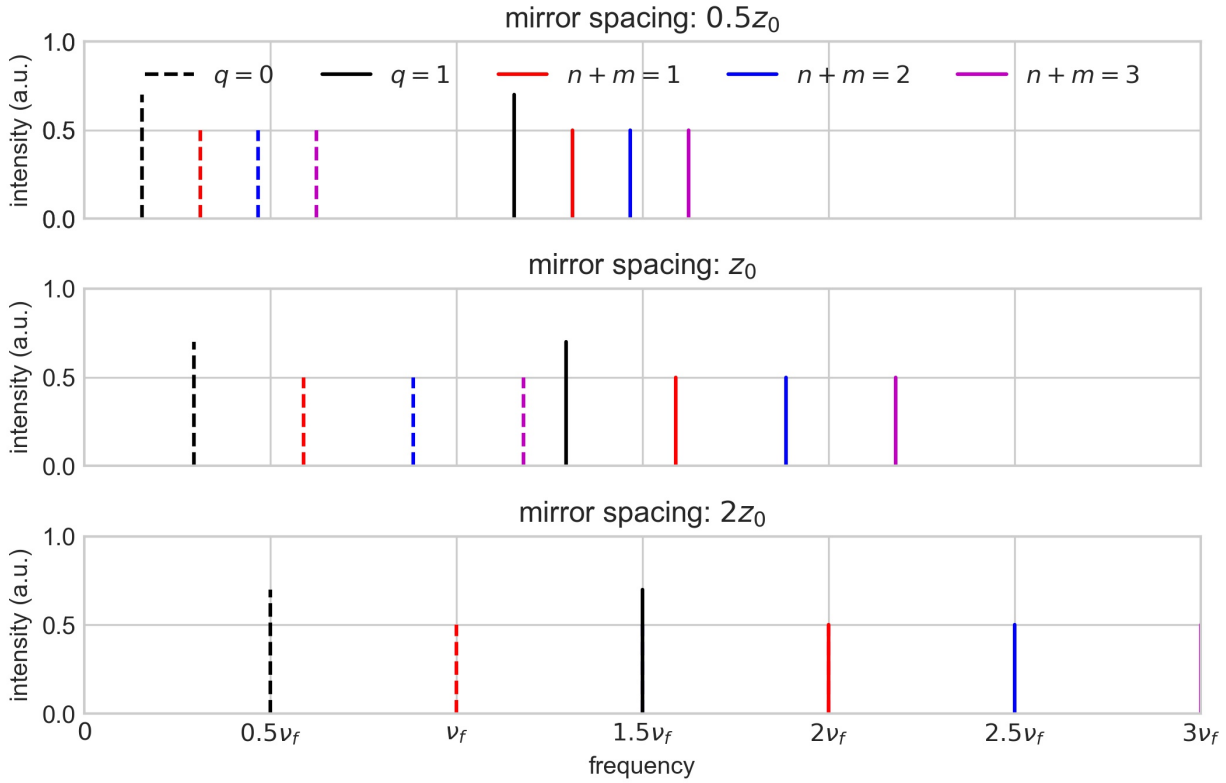

Figure 2.8: *Resonance frequencies for Hermite-Gaussian modes in units of ν_f for varying mirror distances: The dashed resonances are of order $q = 0$, solid ones are of order $q = 1$, and color denotes a change in the sum of (n, m). The intensities are chosen to visually amplify the TEM_{00} and have no physical relevance.*

Consider the phase of the Gaussian beam from Equation 2.21 along the optical axis, with two mirrors located at z_1 and z_2:

$$\phi(0, z_1) = kz_1 - \chi(z_1), \tag{2.33}$$

$$\phi(0, z_2) = kz_2 - \chi(z_2). \tag{2.34}$$

As mentioned earlier, a stable resonator mode requires the Gaussian beam wavefronts to fit the mirror curvature, which requires a shared phase on each point of each mirror. It is therefore sufficient to only regard the phase change on the optical axis, to discuss the resonance frequencies of the resonator [48]. The phase gained due to the reflection on the mirrors will be neglected in the following calculations, since it usually equates to an additional phase shift of 2π. The phase accumulated during the propagation between mirror one and mirror two then becomes:

$$\phi(0, z_2) - \phi(0, z_2) = k(z_2 - z_1) - (\chi(z_2) - \chi(z_1)) = kd - \Delta\chi, \tag{2.35}$$

with d as the distance between both mirrors and $\Delta\chi = \chi(z_2) - \chi(z_1)$. For the beam to reproduce itself, the phase accumulated in one round-trip needs to equal a multiple of 2π. Note that the total phase accumulated in one round-trip is equal to $2(kd - \Delta\chi)$. In a linear cavity the wave needs to travel the mirrors distance twice before it retraces itself. This is not directly applicable for more complicated resonator geometries, for which the round-trip length may be calculated differently. For a linear cavity the resonance frequencies are determined as:

$$\nu_q = q\nu_f + \frac{\Delta\chi}{\pi}\nu_f, \tag{2.36}$$

here $\nu_f = c/2d$ is the so-called free spectral range (FSR) and q an integer. As to be expected, the Gouy phase needs to be respected when considering the resonances of a Gaussian beam. When extending this approach to Hermite-Gaussian beams, the resonance frequencies include another dependency; the orders (m, n) of the Hermite-Gaussian beam phase ϕ_{nm} from Equation 2.29. A similar calculation [48] results in:

$$\nu_{qnm} = q\nu_f + (n + m + 1)\frac{\Delta\chi}{\pi}\nu_f. \tag{2.37}$$

These resonances are visualized in Figure 2.8. The resonance frequencies of the Hermite-Gaussian beam differ from the Gaussian beam by $(n + m)\Delta\chi\nu_f/\pi$. For the same longitudinal mode q this results in a spacing between two transverse modes of:

$$\nu_{qnm} - \nu_{qn'm'} = [(n + m) - (n' + m')]\frac{\Delta\chi}{\pi}\nu_f. \tag{2.38}$$

Note that for different orders with the same sum $n + m$ the resonances coincide.

2.2.4 Lossy resonators

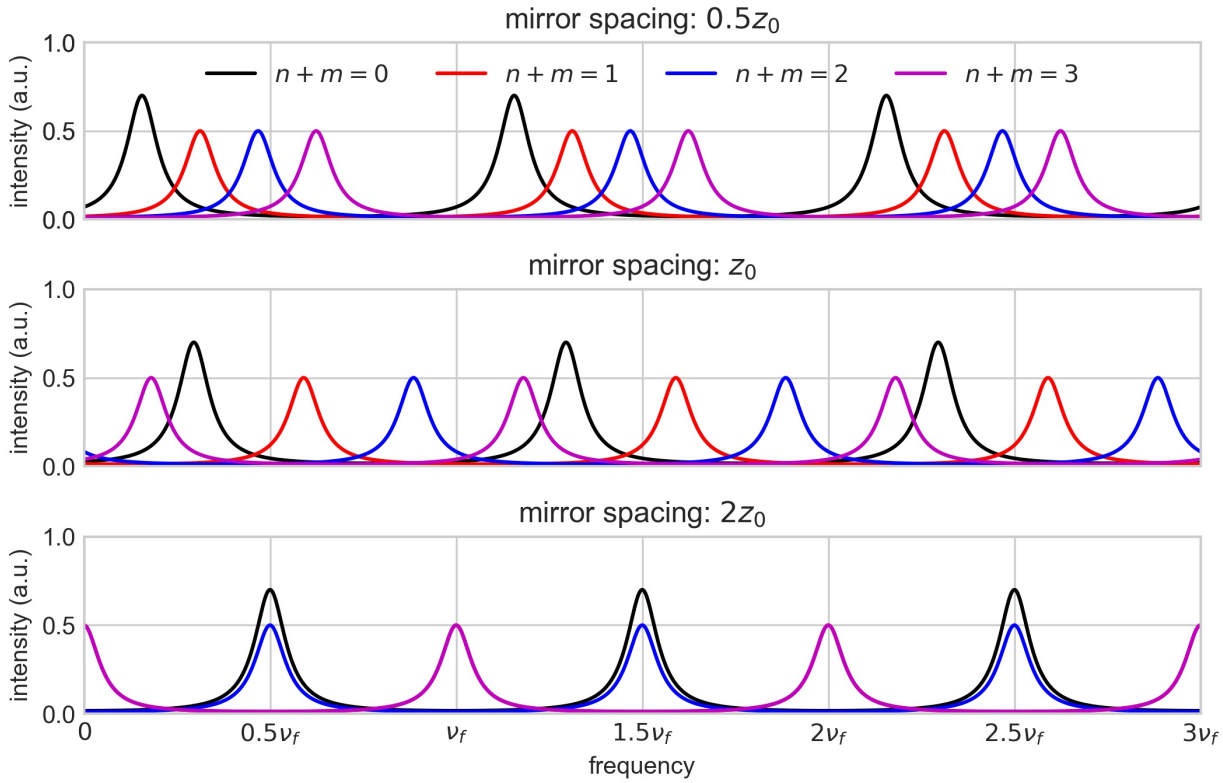

Figure 2.9: *Hermite-Gaussian resonances in units of ν_f for varying mirror distances in a lossy resonator: The maximal intensities are $I_{max} = 5$ and $I_{max} = 3$ for the $(n, m) = (0, 0)$ and $n + m > 0$ modes, respectively, which again are chosen to visually amplify the TEM$_{00}$ and have no physical relevance. The broadening is shown for a Finesse of $\mathcal{F} = 10$ and correctly extends the lossless resonances from Figure 2.8 for any integer q.*

The resonance frequencies as given in Equation 2.37 imply strict resonance conditions, which only apply for lossless resonators [48]. For simplicity consider two mirrors with the same reflectivity $R = |r|^2 < 1$. The round-trip amplitude attenuation factor:

$$h = |r|\exp(-i\phi) \tag{2.39}$$

characterizes the amplitude loss that is linked to each reflection, where ϕ is the phase difference. An incident plane wave U_0 will superpose with the wave $U_1 = hU_0$ after one round-trip, both will superpose with $U_2 = hU_1$, and so on. Unlike the lossless cavity, the result is a geometrical series where each round-trip reduces the previous amplitude by $h < 1$:

$$U_0 + U_1 + U_2 + ... = U_0(1 + h + h^2 + ...) = \frac{U_0}{1 - h} \tag{2.40}$$

The total intensity inside the resonator depending on the attenuation factor and the

incident intensity $I_0 = |U_0|^2$ can now be written as:

$$I = \frac{I_0}{(1-|h|)^2 + 4|h|\sin^2(\phi/2)}. \tag{2.41}$$

This can further be simplified, by defining $I_{max} = I_0/(1-|h|)^2$ and introducing a quantity known as the finesse:

$$\mathcal{F} = \frac{\pi\sqrt{|h|}}{1-|h|}. \tag{2.42}$$

A larger finesse, caused by increased mirror reflectivity and consequently, an attenuation factor $|h|$ that is closer to 1, leads to a more sharply peaked intensity function. Equation 2.41 now takes the form:

$$I = \frac{I_{max}}{1 + (2\mathcal{F}/\pi)^2\sin^2(\phi/2)}. \tag{2.43}$$

This result is visualized in Figure 2.9 for Hermite-Gaussian modes. The phase shift $\phi = k2d = 4\pi\nu d/c$ for one round-trip of the TEM_{00} mode in a Fabry-Perot resonator, neglecting the Gouy effect, can be rearranged to $\nu = (c/4\pi d)\phi$. Inserting the free spectral range $\nu_f = c/2d$ yields:

$$\nu = \frac{\nu_f}{2\pi}\phi. \tag{2.44}$$

Note that the factor of $2d$ in the phase shift and free spectral range in Equation 2.44 cancel each other. The result can thus also be applied to non-linear resonators. The approximation $\sin(\phi/2) \approx \phi/2$ for small deviations around $\phi \approx 2\pi$ is made and Equation 2.43 becomes:

$$I(\phi) \approx \frac{I_{max}}{1 + (\mathcal{F}\phi/\pi)^2}. \tag{2.45}$$

The intensity decreases to half its maximum at $\phi \approx \pi/\mathcal{F}$, consequently the FWHM is equal to $\Delta\phi \approx 2\pi/\mathcal{F}$. The spectral width $\delta\nu \equiv \nu(\phi = \Delta\phi)$, as derived in equation 2.44, of an individual resonator mode therefore depends on the free spectral range and finesse of the resonator as:

$$\delta\nu \approx \frac{\nu_f}{\mathcal{F}}. \tag{2.46}$$

Following the same calculation as before, the spectral width of the Hermite-Gaussian mode of order TEM_{nm} inside a linear resonator results in:

$$\delta\nu \approx \frac{\nu_f}{\mathcal{F}}[1 + (n+m+1)2\Delta\chi]. \tag{2.47}$$

To conclude, the importance of matching the cavity length to the beam frequency for efficient build up of modes has been discussed in detail. Figure 2.9 demonstrates how the intensity inside a resonator behaves for different Hermite-Gaussian modes. The FSR, which depends on the resonator geometry, has to coincide with the frequency of the desired mode.

2.3 Resonator alignment

Resonator alignment refers to the correct coupling of an incident beam to the eigenmodes of the resonator. Consider a resonator with Hermite-Gaussian eigenmodes. An incident TEM_{00} beam will not exclusively couple to the desired eigenmode of the resonator, unless proper alignment can be ensured. Misalignment can present itself in the form of transverse displacement, rotational displacement, waist size mismatching, and axial waist displacement. In 1st order approximation, the rotational displacement can be neglected, this approximation is known as the paraxial approximation. In the scope of this thesis the effects of transverse x-axis displacement in 1st order approximation are derived, assuming that the waist size and axial position are matched with the resonator. Recall the lowest two Hermite-Gaussian equations derived from Equation 2.30 $G_0(u) = \exp(-u^2/2)$ and $G_1(u) = 2u \exp(-u^2/2)$. For simplicity, the following calculations will be carried out in one dimension. The Gaussian equation of the incident beam, with the transverse displacement $\mathrm{d}u$, can then be written as:

$$\Psi_0(u - \mathrm{d}u) = \exp\left(-\frac{(u-\mathrm{d}u)^2}{2}\right) = \exp\left(-\frac{u^2}{2}\right) \exp\left(-\frac{\mathrm{d}u^2}{2}\right) \exp(u\mathrm{d}u). \tag{2.48}$$

For sufficiently small displacements $\mathrm{d}u = \sqrt{2}dx/W(z) < 1$, the terms in 2nd order

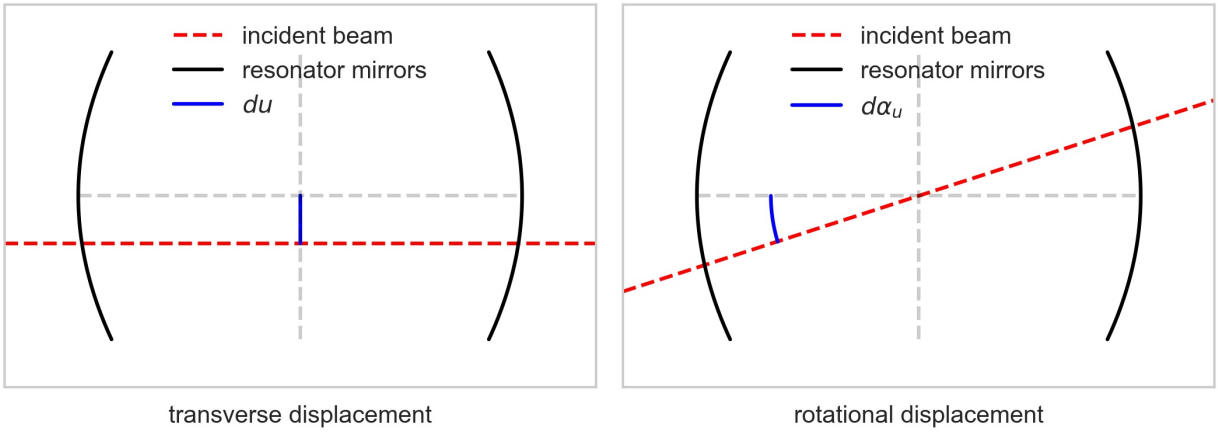

Figure 2.10: *Transverse and rotational displacement of an incident beam in respect to a linear resonator.*

for $\mathrm{d}u^2 \approx 0$ can be ignored. The second exponential function in Equation 2.48 can therefore be neglected, since $\exp(-\mathrm{d}u^2/2) \approx 1$, while the third exponential function can be expanded to the 0th and 1st order: $\exp(u\mathrm{d}u) \approx 1 + u\mathrm{d}u$. When inserting this back into Equation 2.48, the result becomes:

$$\Psi_0(u - \mathrm{d}u) \approx (1 + \frac{\mathrm{d}u}{2}\, 2u) \exp\left(-\frac{u^2}{2}\right). \tag{2.49}$$

Reordering and inserting the 0th and 1st order Hermite-Gaussian equations leads to:

$$\Psi_0(u - \mathrm{d}u) \approx G_0(u) + \frac{\mathrm{d}u}{2}\, G_1(u). \tag{2.50}$$

Thus, it can be seen that small transverse displacements cause an incident Gaussian beam to couple to the TEM_{10} of the resonator. The resulting Hermite-Gaussian beam equation in one dimension can be calculated similar to Equation 2.28:

$$U_0 = \Psi_0(u - \mathrm{d}u)\,\exp(\phi_0) \approx A_\Psi \left[G_0(u) + \frac{\mathrm{d}u}{2}\, G_1(u) \right]\, \exp(i\phi_0), \tag{2.51}$$

with the factor $A_\psi = A_0 W_0 / W(z)$. Note that G_0 and G_1 share a phase, as they originate from the same Gaussian beam. Depending on the resonator length, either G_0 or G_1 can retrace itself and become a resonator mode. The coupling coefficient from the incident beam to the 1st order Hermite-Gaussian mode is $\mathrm{d}u/2$. From here the intensity distribution $I_\Psi(u)$ can be determined:

$$I_\Psi(u) = |A_\Psi|^2\, |G_0(u) + \frac{\mathrm{d}u}{2} G_1(u)|^2 = |A_\Psi|^2\, (G_0^2 + \left(\frac{\mathrm{d}u}{2}\right)^2 G_1^2 + \mathrm{d}u G_0 G_1). \tag{2.52}$$

The result is a superposition between TEM_{00}, TEM_{10}, and the term $G_0(u)G_1(u)$. The resulting intensities are:

$$I_0(u) = |A_\Psi|^2\, \exp(-u^2), \tag{2.53}$$

$$I_1(u) = |A_\Psi|^2\, \mathrm{d}u^2\, u^2\, \exp(-u^2), \tag{2.54}$$

$$2\sqrt{I_0(u) I_1(u)} = 2|A_\Psi|^2\, \mathrm{d}u\, u\, \exp(-u^2), \tag{2.55}$$

respectively, and integration over u from $-\infty$ to ∞ yields the power for each term:

$$P_0 = \sqrt{\pi} |A_\Psi|^2, \tag{2.56}$$

$$P_1 = \frac{\sqrt{\pi}}{2} |A_\Psi|^2\, \mathrm{d}u^2, \tag{2.57}$$

$$P_{01} = 0. \tag{2.58}$$

Now the coupling efficiency $F(\mathrm{d}u)$ for an incident TEM_{00} coupled to the resonator eigenmode TEM_{00} can be determined via $F(\mathrm{d}u) = P_0/(P_0 + P_1)$ and is visualized in Figure 2.11:

$$F(\mathrm{d}u) = \frac{1}{1 + \mathrm{d}u^2/2}. \tag{2.59}$$

For small rotations $\mathrm{d}\alpha_u \ll 1$ the transformation $u' = u\,\cos(\mathrm{d}\alpha_u)$ projects the tilted beam onto the resonator axis. Expanding the cosine and dropping all terms depending on $\mathrm{d}\alpha_u^n$ for $n > 1$ leads to:

$$u' = u \left(1 - \frac{\mathrm{d}\alpha_u^2}{2} + \frac{\mathrm{d}\alpha_u^4}{24} + \mathcal{O}(\mathrm{d}\alpha_u)\right) \approx u. \tag{2.60}$$

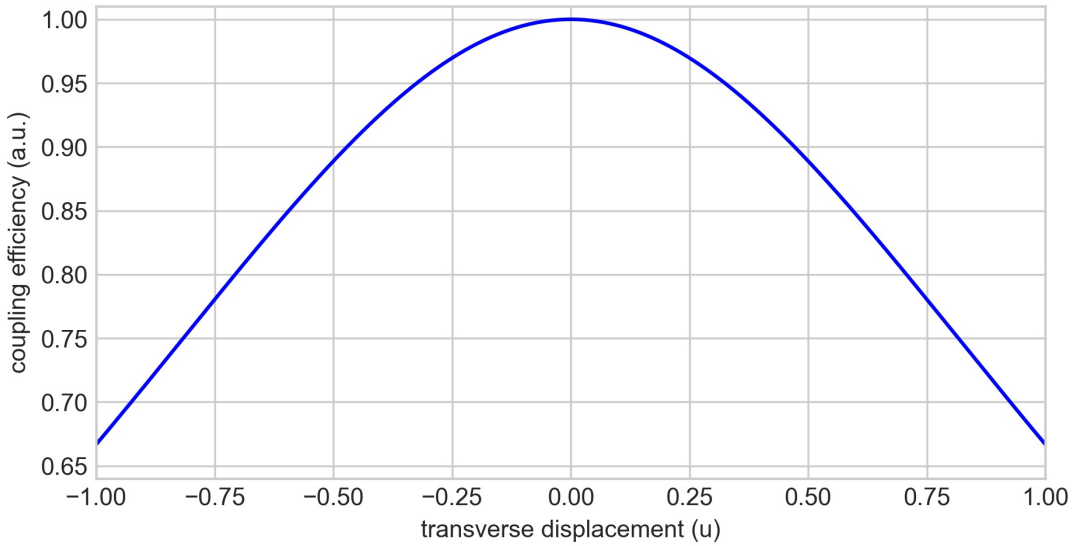

Figure 2.11: *Gaussian mode coupling efficiency as function of the transverse displacement: The Figure shows the excited power of the resonators Gaussian eigenmode depending on the transverse displacement* $du = \sqrt{2}dx/W(z) < 1$ *for an incident Gaussian beam.*

Rotations along the resonator axis can consequently be neglected in 1st order approximation, as stated by the paraxial approximation. To conclude, in 1st order approximation transverse misalignment results in 1st order Hermite-Gaussian mode coupling, while tilts can be neglected. Misalignments need to be corrected to improve the coupling to the desired transverse modes of the resonator. For a bow-tie resonator, finding the exact displacements can be challenging. Piezoelectric elements and stick-slip motors, used to control the alignment, are prone to hysteresis effects and statistical inaccuracies. Calibrations of such elements are usually determined by employing cavity resonances. Additionally, complicated resonator geometries, as well as previous beam transformations, for example mode-matching, chirp pulse amplification, and generally the guiding of the beam, make it difficult to achieve perfect alignment in a real setup. Slight misalignments are unavoidable and add up; manual alignment can be time consuming, prone to error and requires far off-resonance operation. This is where optimization algorithms can shine.

2.4 Femtosecond enhancement cavities

In the prior sections pulses and pulse trains were discussed in detail. In this section the passive amplification of multiple pulses, by effectively "overlapping" them inside a femtosecond enhancement cavity, will be studied [50]. In order to achieve optimal amplification of a pulse train, or frequency comb, not only one but many frequencies are required to be in resonance with the enhancement cavity. Considering Equation 2.12: $f_n = nf_{rep} + f_{ceo}$, the spacing between two adjacent teeth depends on the repetition rate of the pulses, which was visualized in Figure 2.2. In order to amplify the complete spectrum, this spacing must coincide with the FSR spacing, as illustrated in Figure 2.12. Now consider the resonance condition for the accumulated phase in one round-trip

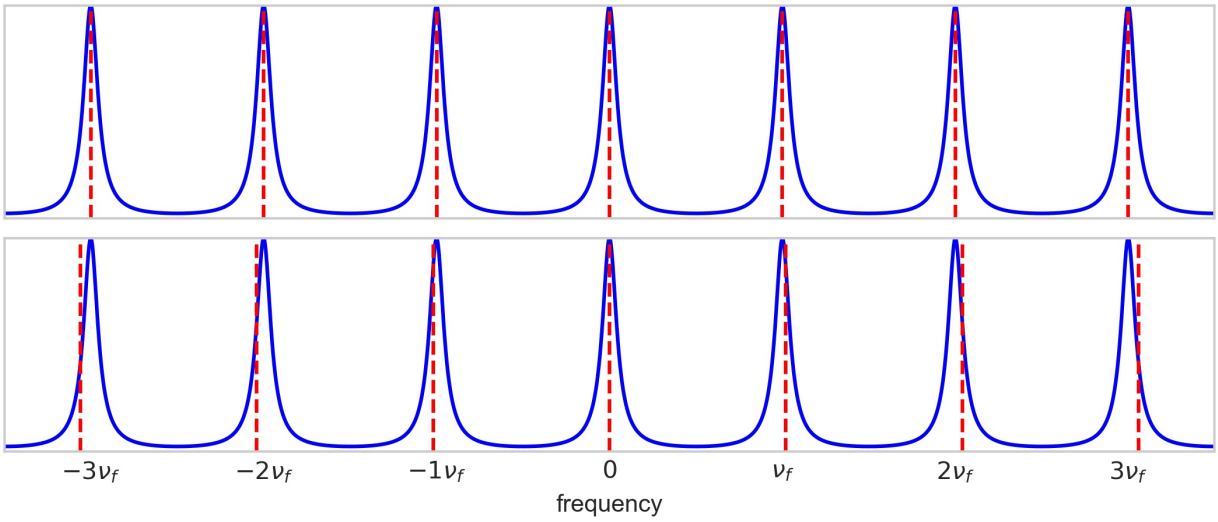

Figure 2.12: *Illustration of comb spacing in a fsEC for $\mathcal{F} = 10$, $k = 1$, and ignoring the Gouy phase: The frequency comb teeth are depicted in red, the cavity resonances in blue. The upper illustration depicts optimal alignment between the cavity resonances and the comb spacing. A small mismatch in spacing, as exaggerated in the lower illustration, will significantly reduce the enhancement, as the number of comb teeth reaches up to 10^5.*

from Equation 2.35, combining any additionally acquired phase in $\phi_d(f)$:

$$\phi = \frac{2\pi f L}{c} + \phi_d(f) = 2\pi q, \tag{2.61}$$

with f as the frequency. Rewriting the relation for the comb spacing results in:

$$n = \frac{f - f_{ceo}}{f_{rep}}. \tag{2.62}$$

Introducing a new integer $m = q - n$, both equations can now be combined yielding:

$$q = n + m = \frac{f - f_{ceo}}{f_{rep}} + m = \frac{fL}{c} + \frac{\phi_d(f)}{2\pi}. \tag{2.63}$$

Reordering and solving for the round-trip length L results in:

$$L_m(f) = \frac{c}{f_{rep}} + \frac{c}{f}\left(\frac{f_{ceo}}{f_{rep}} + m\right) - \frac{c}{2\pi}\frac{\phi_d(f)}{f}. \tag{2.64}$$

Each tooth frequency f is therefore resonant at a specific resonant length $L(f)$, as described in this equation. For $m = 0$ each tooth aligns with a cavity resonance at L_0, which is illustrated in Figure 2.12, neglecting the additional phase $\phi_d(f)$ and CEO frequency f_{ceo}. Consequently, at the length L_0 the frequency comb spectrum shares the

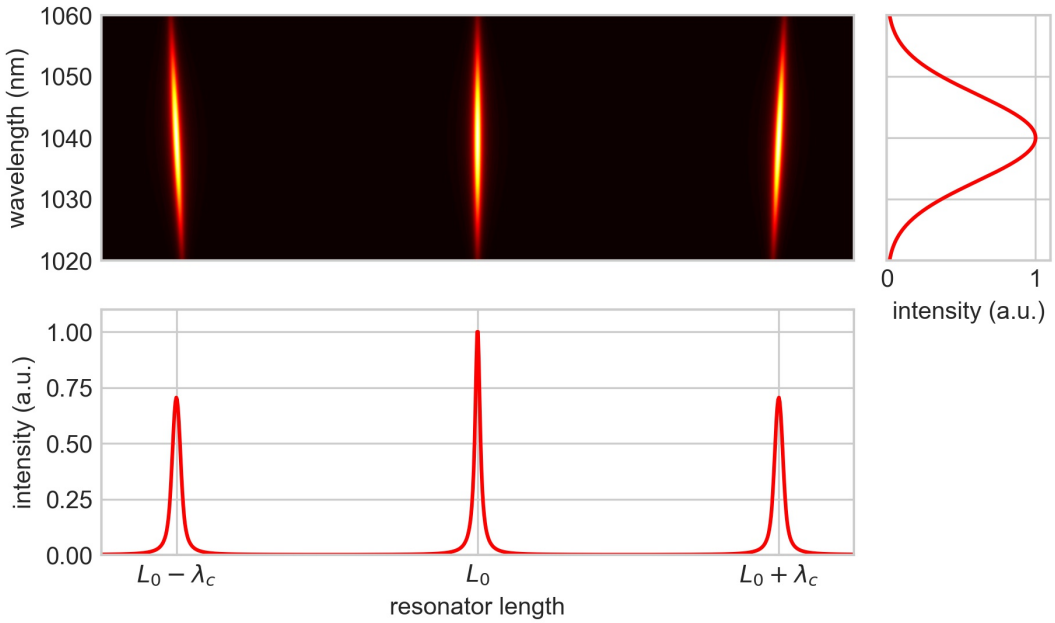

Figure 2.13: *Normalized total intensity of a frequency comb in a fsEC for $\mathcal{F} = 50, 10^3$ comb teeth, $\lambda_c = 1040$ nm, and $\phi_d = f_{ceo} = 0$: The top right figure displays the frequency comb spectrum with a standard deviation of $\sigma = 10$ nm. The top left shows the tilted resonances. The tilt is a result of the slight deviation in resonance length for higher longitudinal modes, depending on the wavelength. The sum over the intensity distribution for all comb modes results in the total intensity depicted in the lower half of the figure. As a result of the tilt, the resonances are broadened out and less intense.*

same resonance length for all teeth, resulting in optimal enhancement. At L_m, for $|m| > 0$, broadened resonances appear, as shown in Figure 2.13. These fsEC modes are longitudinal modes, as opposed to the transverse modes discussed in previous chapters. A relation for the total intensity can be calculated by summing over the intensity distributions for each comb tooth wavelength $\lambda_n = 2\pi c/\omega_n$ resulting in:

$$I_{tot}(L) = \sum_{n=0}^{n=10^5} \frac{A(\lambda_n - \lambda_c)}{1 + (2\mathcal{F}/\pi)^2 \sin^2(\pi L/\lambda_n)}, \tag{2.65}$$

where the intensity distribution from Equation 2.43 was utilized, the Gaussian envelope from Equation 2.5 describes the maximal intensity, and with the length dependent phase from Equation 2.61, neglecting the additional phase.

Until now, the phase shift introduced by the mirrors was neglected. As a wide range of frequencies are circulating the resonator, the mirror reflectivity is required to cover the whole spectrum and it is necessary to consider the so-called dispersion, which depends on the frequency. The dispersive phase can be expanded around the central frequency f_c of the comb, giving rise to:

$$\phi_d(f) = \phi(f_c) + \phi'(f_c)(f - f_c) + \frac{1}{2}\phi''(f_c)(f - f_c)^2 + \mathcal{O}(f), \tag{2.66}$$

$$\equiv \phi_0 + \phi_1(f - f_c) + \phi_2(f - f_c)^2 + \mathcal{O}(f). \tag{2.67}$$

In 0th order a constant phase shift ϕ_0 is added to the pulse, in 1st order the so-called group delay ϕ_1 is responsible for a time delay of the pulse envelope, and in 2nd order the group delay dispersion ϕ_2 leads to broadening of the pulse envelopes. The 0th order phase shift behaves similarly to the CEO phase, as it also shifts the carrier frequency maximum in respect to the envelope maximum. This can be corrected for, by adjusting the CEO phase accordingly. An initial pulse, that has accumulated the same amount of phase due to 0th order dispersion, will constructively interfere with a succeeding pulse, that has the same phase shift introduced by the CEO. The envelope delay caused by 2nd order dispersion can be canceled out, by adjusting the resonators round-trip length. Additionally, optimized mirrors with low dispersion can be installed, to further reduce 2nd order dispersion.

2.5 Optimization algorithms

2.5.1 Problem assessment

Automated optimization has taken over in all different aspects of research and industry alike [51]. Just as abundant as the applications of automated optimizations are, such is the diversity of optimization algorithms. Each problem has its own specifications, advantages, and disadvantages each favoring a different approach. This consequently also applies to the alignment optimization problem presented in this thesis. A suitable alignment optimizing algorithm must operate within the restrictions of the setup and physics, to achieve its objective of increasing the intensity of the desired Gaussian mode in a fsEC, by adapting its alignment. Suitable input parameters, which are processed by the algorithm, and output parameters, which are returned, have to be determined.

The alignment of the cavity operated in this thesis is controlled by piezoelectric stick-slip motors also known as inertia motors, which effectively change the angles of the mirrors step-wise. A piezoelectric element inside the motor is expanded, by applying high voltage. This expansion is slow enough to "stick" to the mechanism that is adjusting the tilt of the mirror, due to its static friction. The voltage is then quickly released and the piezoelectric element "slips" past the mechanism, as it overcomes the static friction in favor of kinetic friction, leaving the mechanism in its new position. The advantage of these type of actuators lies within their increased range, as the mechanisms position can be increased by a multitude of the elements expansion. On top of that, shutting of the power supply does not impact the actuator position. On the other hand, it is not straight forward to acquire its exact position. Tracking the amount of steps performed introduces errors due to hysteresis effects between forward and backward motions and statistical effects, as the element might fail to "stick" or "slip" from time to time, resulting in a missed step. The evaluation of the initial state for the determination of the absolute position is also challenging. Even with individual calibrations for each actuator, the error grows with each step and an additional method, such as the implementation of an interferometer or goniometer, is indispensable to determine the exact position. Therefore, steps were selected as an output parameter, while a more advanced setup could provide the algorithm with a precise position.

Continuing with the input parameters, the motor control should depend on the intensity of the Gaussian mode inside the resonator. The diagnostics of the setup provide two appropriate sources: charged-coupled device (CCD) cameras and photodiodes. A CCD camera can be used to find the intensity distribution of the TEMs inside the resonator, but distinguishing between different modes turned out to become rather demanding, as mode decomposition would have to be performed in real time. Image analysis involves finding the exact center, tilt and beam width in each plane, all of which are influenced by the subsequent optimization steps and the positioning of the camera. Furthermore, the desired close to resonance operation requires a continuous resonator length scan, as depicted in Figure 2.14, to distinguish between the fundamental Gaussian mode and

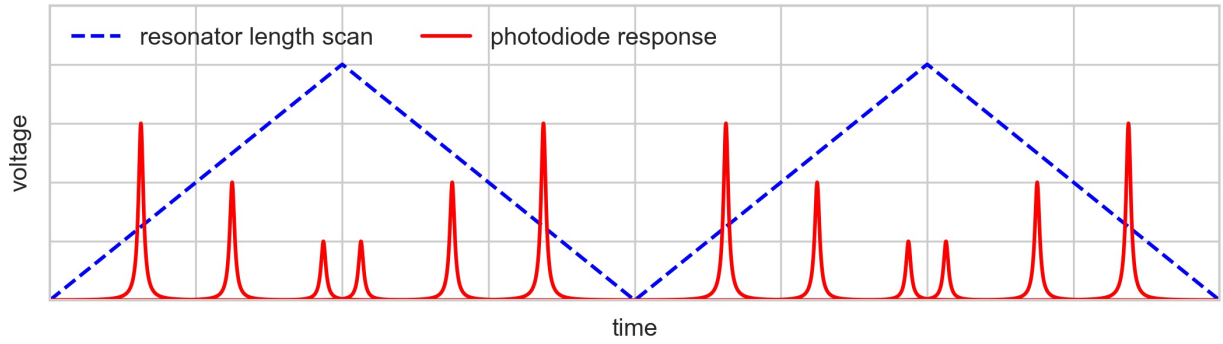

Figure 2.14: *Illustration of resonator length scan and photodiode response over time: The resonator length is being scanned continuously by a triangle voltage signal applied to a piezoelectric element. This element is directly changing the resonator length and has a smaller range than the stick-slip motors, in exchange for a quicker response time. The here illustrated transmitted intensity presents multiple* TEM_{nm} *in intensity decreasing order: the prominent one for* $n + m = 0$ *adjacent to the* $n + m = 1$*, and lastly the* $n + m = 2$ *mode. In this illustration no higher longitudinal modes are displayed. Both signals are synced and send to the algorithm as input parameters.*

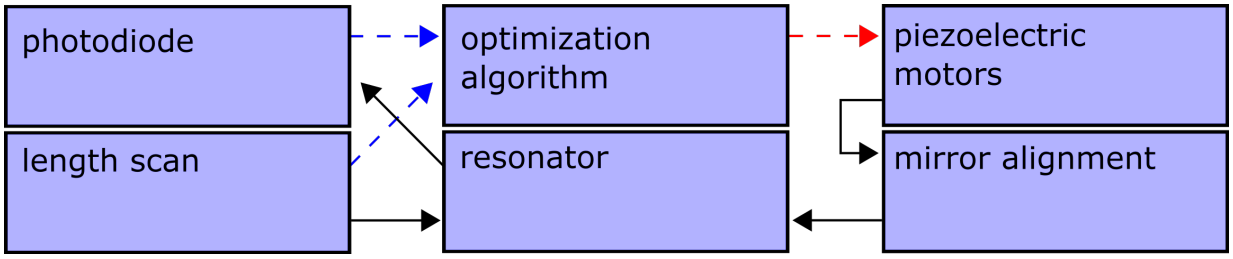

Figure 2.15: *Closed-loop optimization process: The blue arrows depict the input and the red one the output, which is determined by the algorithm. The length scan itself is not part of the closed loop.*

higher modes, which are supposed to be diminished. One solution would be to limit the cameras integration time to one scanning period and synchronize both. However, the only advantage of the CCD camera over the photodiode is the possibility to distinguish between higher TEMs with the same resonance frequency, due to the two-dimensional intensity distribution being unique. Since the bow-tie resonator in this thesis does operate with a lower mirror spacing than the $0.5z_0$ shown in Figure 2.9 and the intensity of higher modes drops off significantly, it is reasonable to assume that the Gaussian mode does not share its resonance with any other mode. Additionally, the optimization of the TEM_{00} is of interest, therefore the photodiode provides the more accessible fitness function and requires less computational power. As the length of the cavity is scanned the photodiode returns the TEM intensities as shown in Figure 2.14. Finally the photodiode is synchronized with the scanning frequency and can produce a suitable fitness func-

tion, while the CCD camera can be used to qualitatively visualize the different modes. A more advanced setup could analyze the camera images in real time and allow for optimizations of higher modes.

2.5.2 Hill climb algorithms

An algorithm suited for this type of optimization has to work without relying on the state the system is in, as it cannot reproduce any mirror positions. This premise leads to the exclusion of genetic algorithms (GA), which otherwise would provide an effective solution. The amount of input information is restricted to a few modes inside the scanning range, while vibrations can strongly influence the input. The amount of automated mirrors can be modified, resulting in multidimensional solution spaces. Based on these restrictions, a well suited type of optimization algorithms are given by the so-called hill climb (HC) algorithms [51]. A HC performs a local search around the current state and generally moves towards a favorable neighbor, until none provide favorable results. Although HCs are not systematic, they have their advantage in adaptability, amount of storage required, and they are often able to find reasonable solutions within a larger search space. Furthermore, the Gaussian mode intensity provides a single fitness function as an input, which is sufficient for a HC.

However, HC algorithms have their downside as well; they only search locally. Consequently, HCs can get stuck in local extrema, rigid slopes, or even plateaus. One possible state space is shown in Figure 2.16. A HC trying to maximize the fitness function and approaching from the left would get stuck in the rigid slope, due to the abundance of local maxima. On the other hand, a HC approaching from the right could get stuck on the plateau, since no neighbor provides a superior solution. Finally, a HC starting in the middle would have a chance to look for a superior neighbor to its right, which would lead it to the local maxima. To overcome these issues, a variety of HCs have been developed over the past. A popular adaptation is the so-called random-restart HC. As the

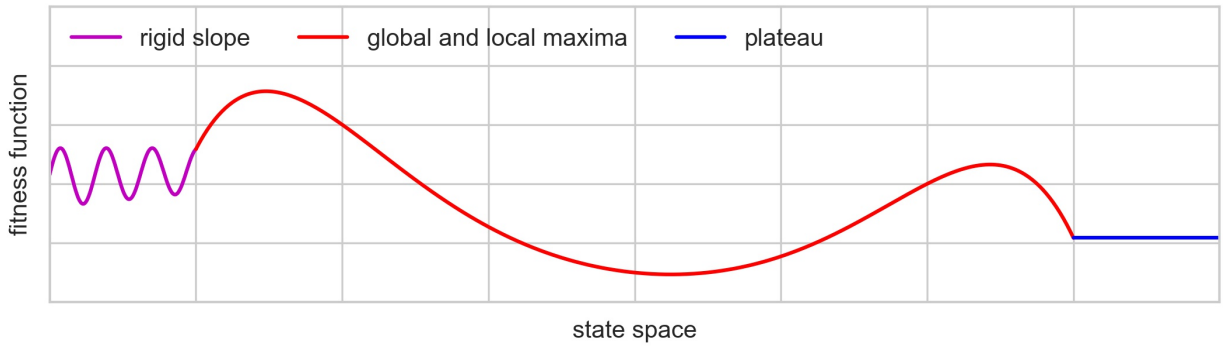

Figure 2.16: *State space for arbitrary fitness function: The displayed state spaces can be troublesome for a hill climb, as the algorithm can get stuck in a rigid slope, local maxima, or on a plateau.*

name suggests, it performs multiple HC, each time from a new and randomly selected initial state. Given enough time, the initial state must be close to the global maxima and the desired solution is found. As a trade-off more iterations are required, to find a solution. Transverse misalignment in first order approximation results in coupling

to first order TEM and the resulting coupling efficiency from Figure 2.11 depicts the corresponding fitness function. It can be deducted, that a random-restart HC is not necessary, since no local maxima are present. This has to be taken with a grain of salt. The assumptions made to derive the coupling efficiency do not include vibrations, higher mode coupling due to strong rotational displacement, beam waist misalignment, and it was assumed that a Gaussian mode is coupled in without any higher modes present. In order to verify the HC approach, the coupling efficiency has to be measured directly.

The explicit hill climb algorithm for this thesis will be explained in more detail in a following chapter. Each time a step is made, the intensity before and after the step are compared and, if the difference in intensity is smaller than the error due to intensity fluctuations, a step in the wrong direction can occur. This can be overcome by starting with a large step size and, each time the fitness function decreases, reducing the step size and inverting the direction. The HC effectively overshoots its target, turns around, and looks for the maximum in the opposite direction, this time with a reduced step size. This way fluctuations can be "jumped over" and only take effect when the step size becomes sufficiently small, at which point the HC is already in close proximity to the global maximum. Close to the global maximum this method loses its effectiveness, as the fitness function error becomes bigger than its gain, where the coupling efficiency gradient approaches zero.

2.5.3 Genetic algorithms

Genetic algorithms (GA) are a type of stochastic algorithm [51]. GA produce new states from two or more previous states. Starting off, the fitness of two parent states is determined, after which they get mixed up and the resulting fitness of the child state is compared to the parent state. The state of lowest fitness is then removed. Each generation, a new set of states is produced and given a sufficiently large random initial state space, each generation converges closer to the global extremum. Without the ability to reproduce a, comparisons between multiple states become impossible. Including an interferometer, to measure the exact mirror tilt after each step, could enable different variants of GA, for example differential evolution (DE), as viable optimization algorithms. But due to the vacuum, the setup is tight, expensive, and diagnostic becomes difficult and time consuming.

The implementation of a GA, more specifically DE, was attempted but failed to the above mentioned reasons. Even with implementation of calibration factors, the statistical error of the mirror tilt position lead to falsely reproduced previous states, as each iteration required a large amount of steps to reproduce multiple states, which could be distanced by more than 100 steps at a time. This quickly lead to degradation of the fundamental Gaussian mode instead of optimization and increased runtimes.

3 Experimental setup

3.1 Enhancement cavity

A schematic of the experimental setup is shown in Figure 3.1. The near-infrared frequency comb, at a repetition rate of $f_{rep} = 100$ MHz, is mode-matched and coupled into the bow-tie resonator. The frequency comb operated in this thesis can be extended into the XUV regime, by means of HHG [49]. To counteract the high absorption in air, an UHV chamber envelopes the resonator mirrors. One arm of the bow-tie geometry is folded by two additional flat mirrors, since the UHV chamber restricts the dimension of the setup and a round-trip length for the fsEC of ~ 3 m is required, which corresponds to the repetition rate f_{rep}. The transmitted light is picked up and divided by a beam splitter, and the intensity distribution is read out by a CCD camera (*Allied Vision Mako G-234B*), while the intra-cavity power is monitored by a photodiode. The resonator length can be controlled fast within a short range via a piezo chip (*HPCh 150/12-6/2*) mounted mirror and slower at a higher range via a piezo-controlled translation stage. The cavity length is scanned by the piezo chip through a signal produced by a *Red Pitaya*. The input coupling (IC) mirror and the piezo-controlled translation stage mirror, from here on referred to as PZT mirror, are placed inside piezo actuated mirror mounts. These actuators control the tilt of the mirrors in x-axis and y-axis and thus the alignment. Except for the piezo chip, all piezo actuators are controlled by "Physik Instrumente" (PI) devices. The optimization algorithm reads out an oscilloscope (*InfiniiVision DSOX2024A*) and returns the calculated output parameters to the stages, which control the mirror tilts. The oscilloscope is used to acquire a trace containing the synchronized intra-cavity power and the length scan signal. The scanning signal is first amplified by a factor of four before it is converted to high-voltage and fed to the piezo chip. The unamplified scanning signal and resonance power voltages are passed as an input to the optimization algorithm. The algorithm returns the output parameters, effectively controlling the IC and PZT mirror tilt and the resonator length in a closed-loop operation. The optimization algorithm can be monitored and controlled from a dedicated computer. The control software was written for this thesis and does not consists exclusively of the optimization algorithm. Control and read out for the resonator length piezo stage, oscilloscope trace, and camera image are implemented as well. This software will be discussed in more detail in the following chapter.

The setup could be expanded upon, by including the mode-matching telescope into the optimization algorithm. Furthermore, by adapting a faster synchronization method for the input parameters, the oscilloscope read out could be avoided. This read out tends to be time consuming, as the oscilloscope needs to be read out multiple times per algorithm iteration, slowing down the process considerably. The number of iterations per optimization is not affected and provides a more fitting quantity, to determine the optimization speed.

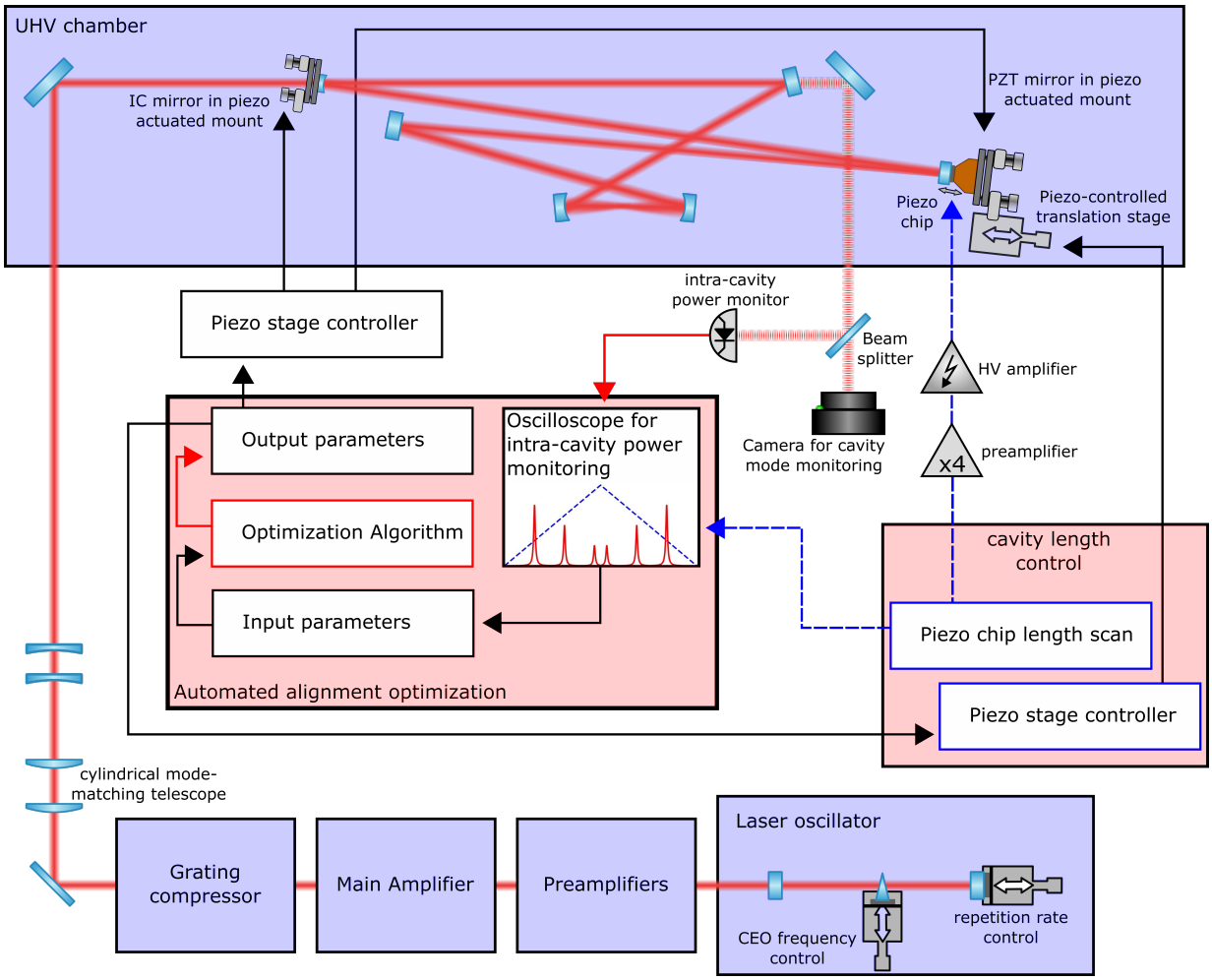

Figure 3.1: *Resonator and control hardware setup: The automated optimization setup retrieves the oscilloscope trace composed of the synchronized resonance power and the resonator length, as scanned by a piezo chip. For larger length adjustments, the PZT mirror is mounted onto a translation stage. The IC and the PZT mirrors are mounted on actuators, that control the mirror tilt in the x-axis and y-axis.*

3.2 Control software

The control software [52] was designed and written within the frame of this thesis for the purpose of automated alignment optimization. It is written in python, using the flask web framework, for the back-end and JavaScript, HTML, and CSS for the front-end. This application runs on a designated computer, which is physically connected to the oscilloscope, in the same network as the piezo elements and monitoring devices, and acts as a server. Clients can access the control application in their browser via the server IP, if they are connected to the same network. This allows multiple clients to control the application and observe the system at the same time. The application is not exclusively useful for the alignment optimization. It also allows the user to connect to and control any PI devices or Allied Vision cameras, that are located within same network, providing a convenient compilation of otherwise separated control software. Figure 3.2 depicts a screenshot of the graphical user interface (GUI) of the control application. Larger screenshots of the different parts follow in the next sections.

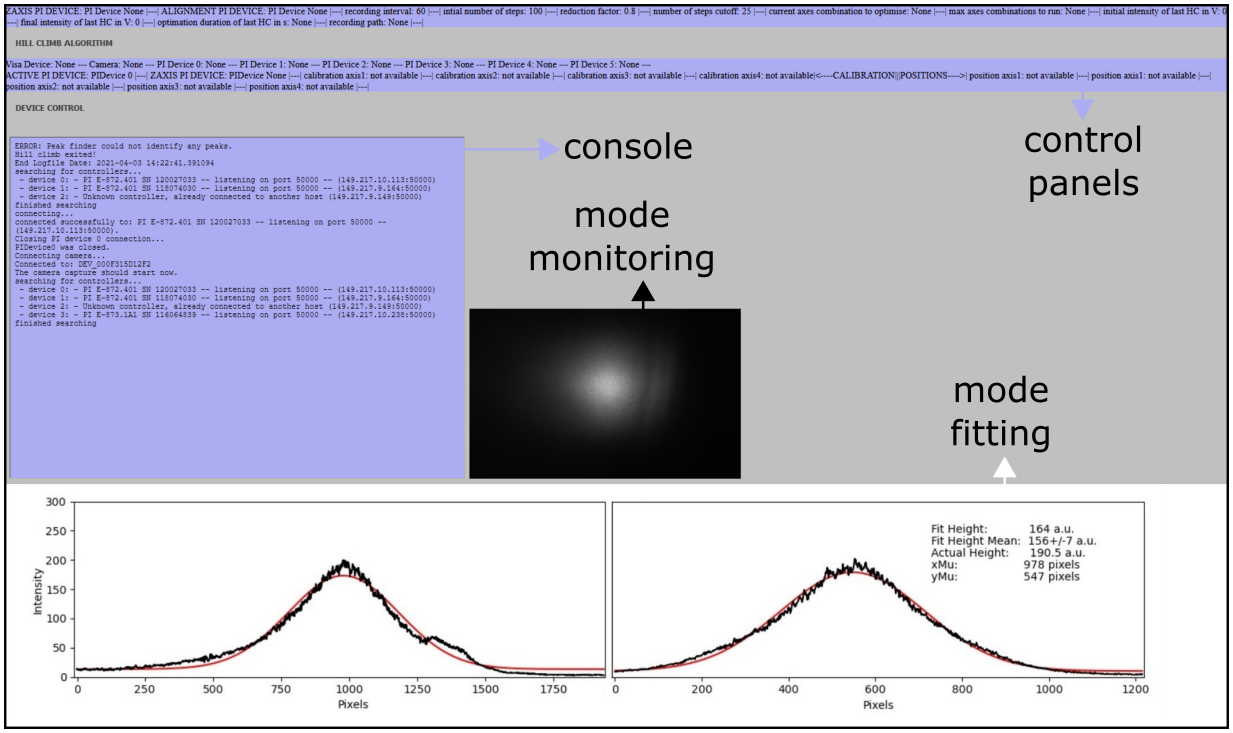

Figure 3.2: *Control application GUI screenshot: The control application can be divided into four parts: The control panels (here minimized), which display system settings and allow for user input. The console, where user inputs and system outputs are logged. The camera stream, where the cavity mode is monitored. And two figures, which display the mode fitting over both camera axes in real time.*

3.2.1 Hill climb control panel

The GUI control panels are depicted in Figure 3.3 and Figure 3.4. Clicking on the buttons *HILL CLIMB ALGORITHM* or *DEVICE CONTROL* will open up a section with further buttons and input fields, to control the application. On top of the panels various information is shown, shaded in blue.

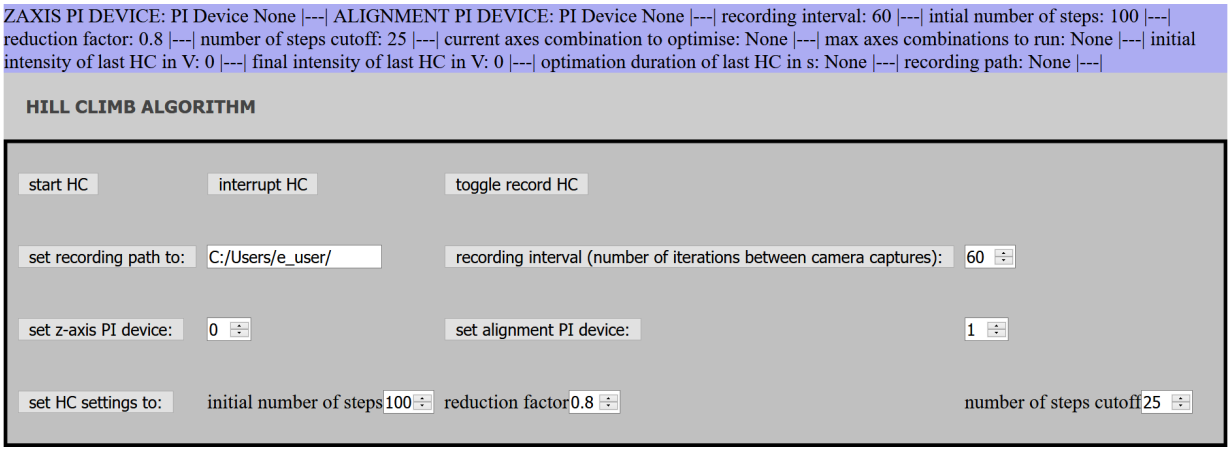

Figure 3.3: *Hill climb control panel: Here the HC settings can be controlled. The text boxes highlighted in light gray are buttons, while the area shaded in blue displays various settings.*

In the hill climb control panel, see Figure 3.3, the hill climb optimization can be started, halted, and a recording option can be toggled. This option will output a detailed log file along with camera images of the hill climbing process in a designated folder at the chosen path. The log file contains detailed information, such as the axis driven, the number of steps, iterations, intensities, warnings, runtime, and more. The recording interval can be set as well, to control the number of iterations between subsequent camera captures. Further down below, the z-axis device can be selected. This device will be used by the HC algorithm to control the resonator length. Similarly an alignment device can be set, which will be used to control the alignment. Finally the HC settings can be adjusted. These settings include the initial number of steps, the reduction factor, and the number of steps cutoff. These settings and their impact will be discussed in more detail in the following sections.

In the area highlighted in blue, various settings and results are updated and displayed in real time. The axes combination refers to the axes that are optimized per iteration, which is set to optimize each axis once by default. This can be adapted within the code, to optimize multiple axes per iteration or even the same axis multiple times in a row.

3.2.2 Device control panel

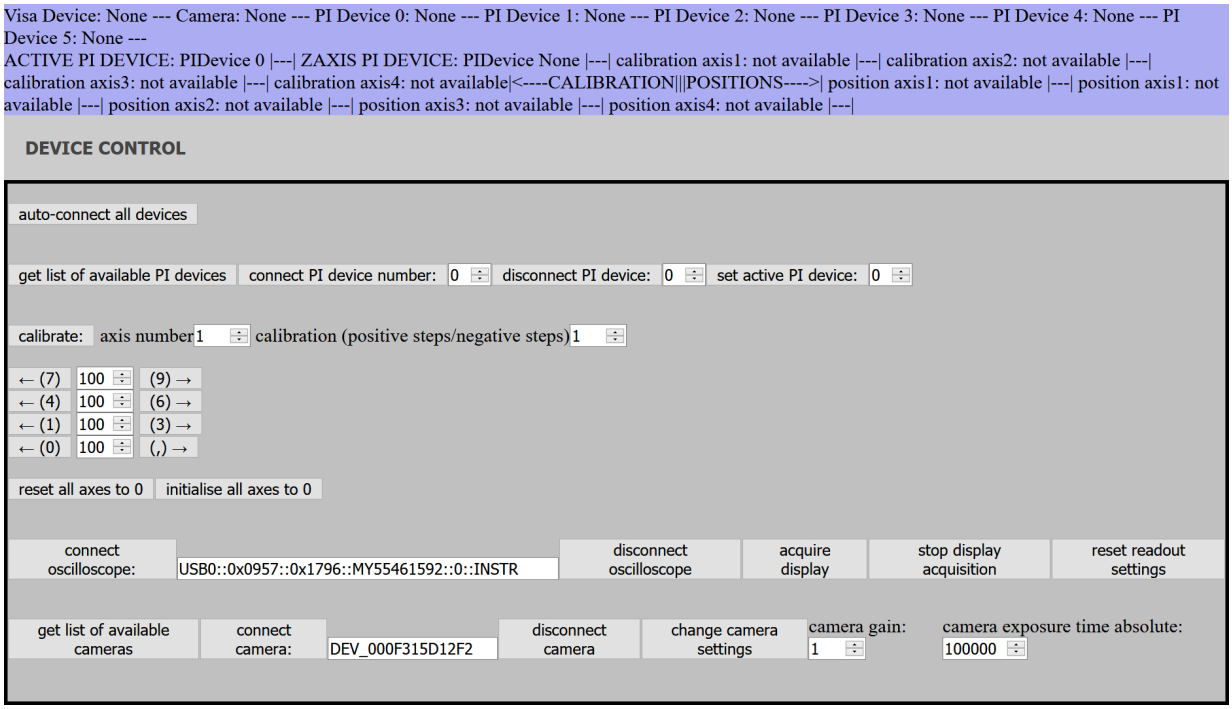

Figure 3.4: *Device control panel: This panel is used to control PI devices, oscilloscopes and cameras. As before, text boxes highlighted in light gray are buttons, while the area shaded in blue displays various settings.*

direction	axis 1	axis 2	axis 3	axis 4
negative	7	4	1	0
positive	9	6	3	.

Table 3.1: *Numeric keypad hotkeys used to control the active PI device axes: The number of steps per hotkey press can be set in the input field between the arrows.*

• The *preset auto-connect all devices* button utilizes a preset, to connect to the standard oscilloscope, camera, and PI devices. After using the preset connection, the HC can already be started, if the length scan is running and the mode to optimize is within the scanning range.

• To get a complete list of all PI devices located within the same network, including their IP address, MAC address, and connection status, the button *refresh list of PI devices* can be used. These PI devices can then be connected to or disconnected from.

• The *active PI device* setting is used to determine which device is actively controlled. The active device will be used for any manual adjustments: calibration, moving an axis, resetting all axes to their initial positions, and initializing all axes to their current positions.

• The calibration setting can be used, to calibrate positive steps to negative ones for the specific axis, as chosen in the *axis number* input field. If for example $n_{pos} = 9$ steps in one direction could be reversed by $n_{neg} = 10$ steps in the opposite direction, the resulting calibration factor would be 0.9. This calibration factor will be used by the application, when driving an axis. However, due to the statistical error caused by missed steps, after driving many steps the tracked position does not resemble the real position very well, despite calibrating.

• The arrow buttons are used to manually drive the axes of the active PI device by the number of steps displayed. Alternatively, it is possible to use the hotkeys, which are displayed in the brackets next to the arrows and in Table 3.1.

• Resetting all axes will physically drive all axes back to the position they were initialized in. This does respect the set calibration for these axes and, if no calibration is set, will likely not reproduce the initial state very well.

• The *initialize all axes to 0* button will set the position tracking of all axes to the position 0. This process does not physically move any piezo actuators.

• After connecting to an oscilloscope, the display can be acquired. This display will update in real time and depict the oscilloscope traces. As the readout is quite slow, the acquisition is as well. During the HC this acquisition will be halted automatically, to improve the applications performance.

• The application allows to connect via Ethernet to Allied Vision cameras in the same network. The gain and exposure time of a connected camera can be adjusted.

3.2.3 Console

The console, shown in Figure 3.5, allows the user to track the application processes. When any actions are performed, it will confirm said actions, give detailed information and warnings or error messages. The log messages include the updated list of available PI devices, driving an actuator, connecting any device, changing settings, and many more. The console output can be logged during hill climbing. If the *Toggle record HC* setting is turned on, recording of the console log will be enabled.

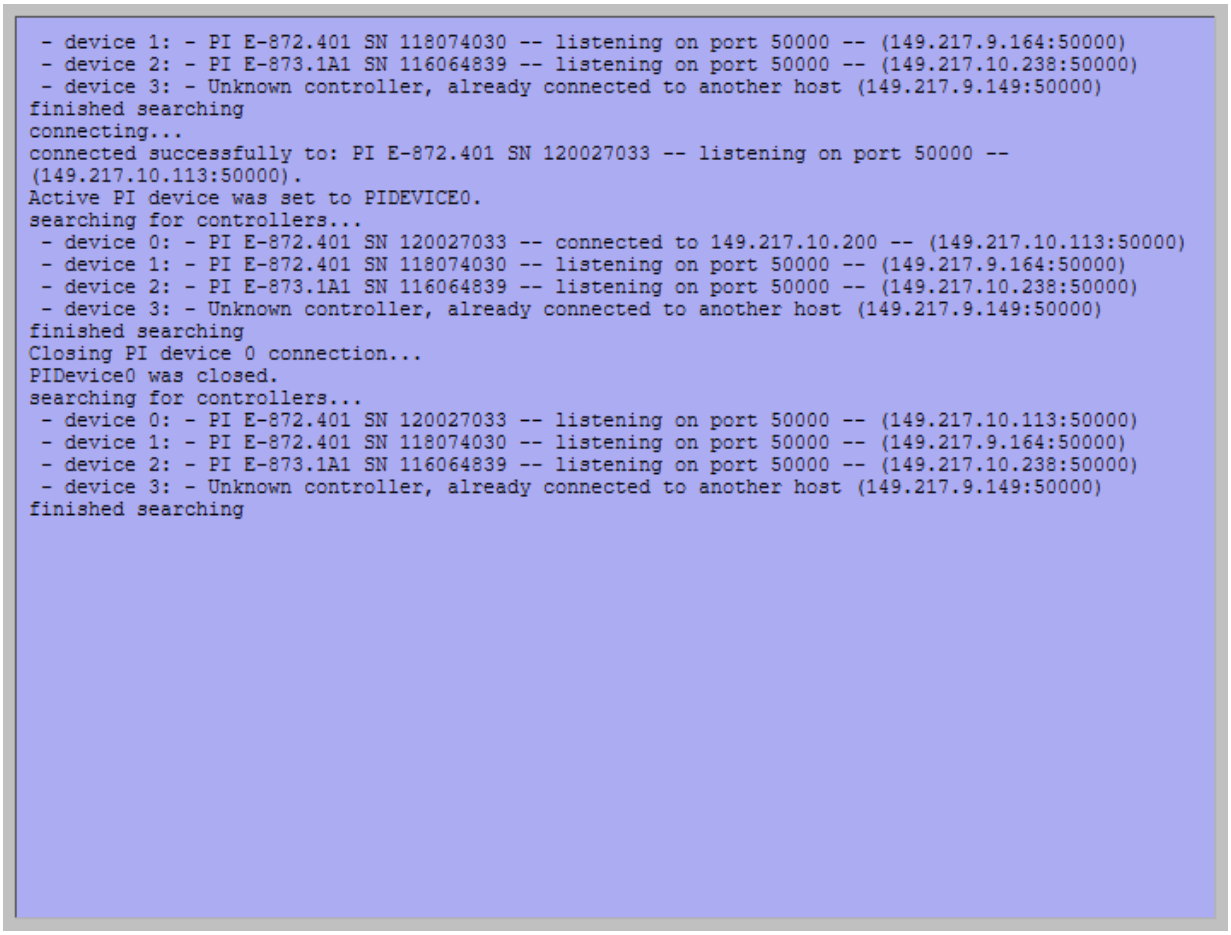

Figure 3.5: *Control software console: Here the application processes can be tracked. In this window the user successfully connected to and disconnected from the same PI device.*

3.2.4 Mode monitoring

The mode monitor starts when a camera is connected. The intra-cavity mode will be streamed and fitted in real time. A typical camera image can be seen in Figure 3.6.

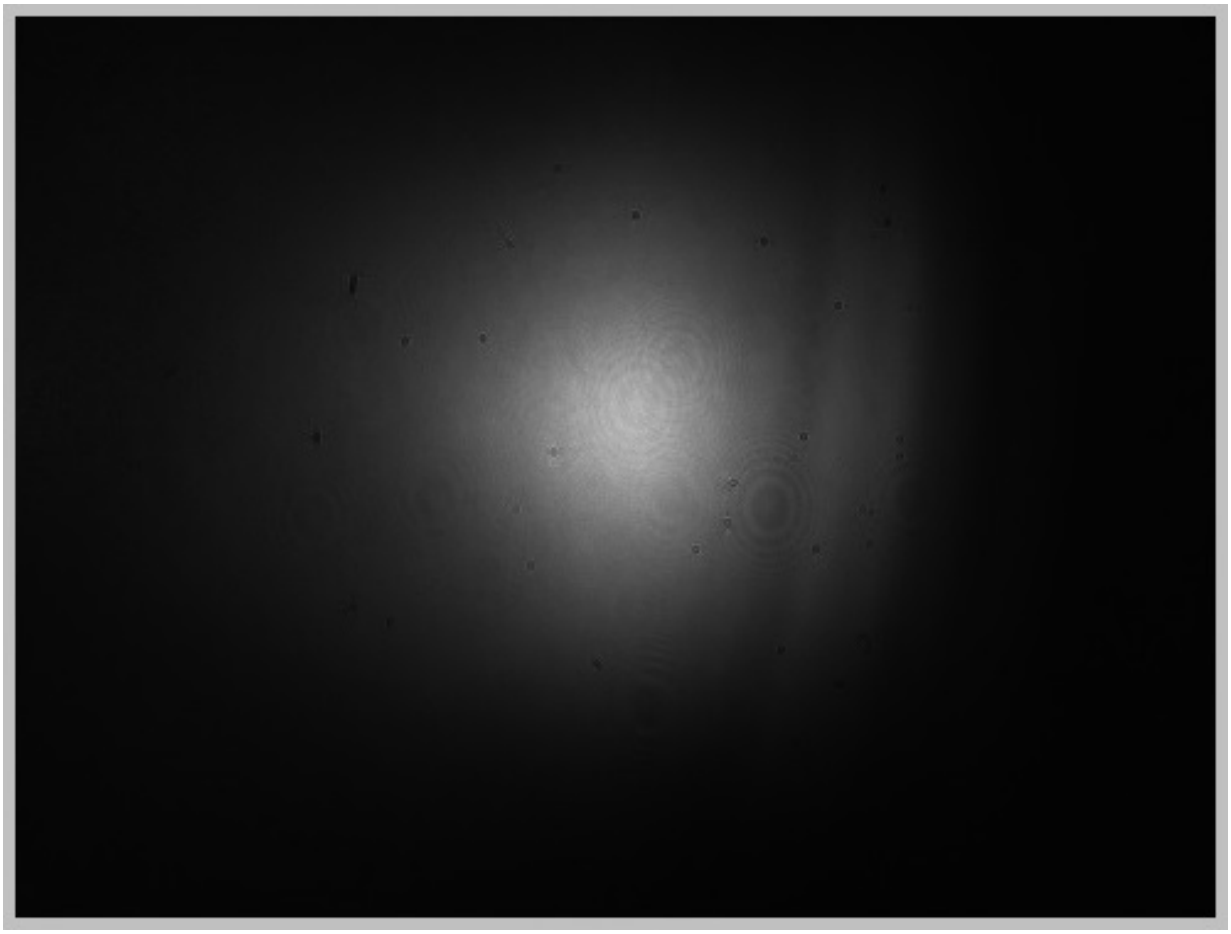

Figure 3.6: *Control software mode monitoring: The camera is capturing the intra-cavity Gaussian mode. The vertical lines on the right side of the mode are likely caused by diffraction off an unknown optical element.*

3.2.5 Mode fitting

The monitored mode is being analyzed in real time. For this, the intensity distribution is integrated over both camera image axes and fitted appropriately. The resulting mode fitting is depicted in Figure 3.7.

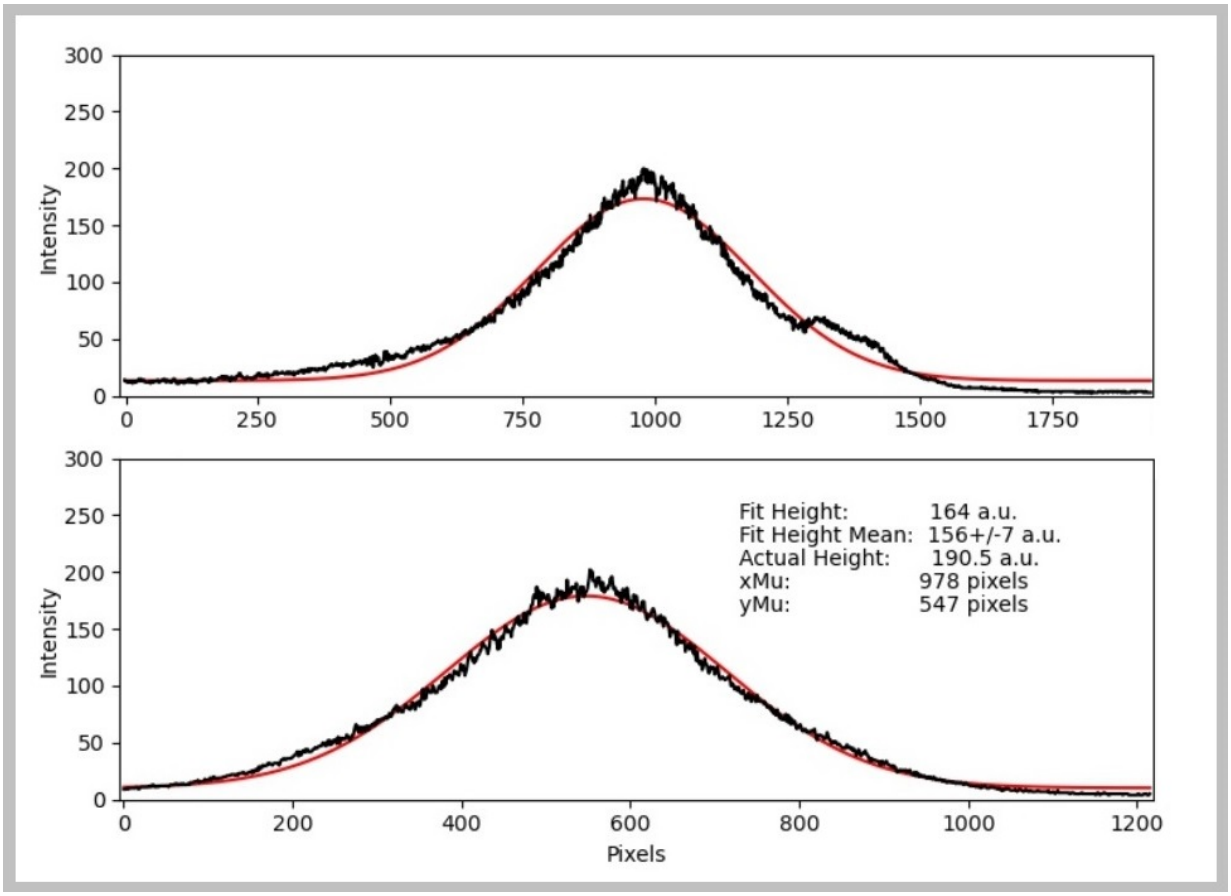

Figure 3.7: *Control software mode fitting: In the top right side of the lower image the fit parameters are updated and displayed. The fit height mean value results from an average over the past* 10 *fits, the actual height depicts the highest value of the intensity distribution.*

3.3 Optimization algorithm

3.3.1 Alignment optimization algorithm

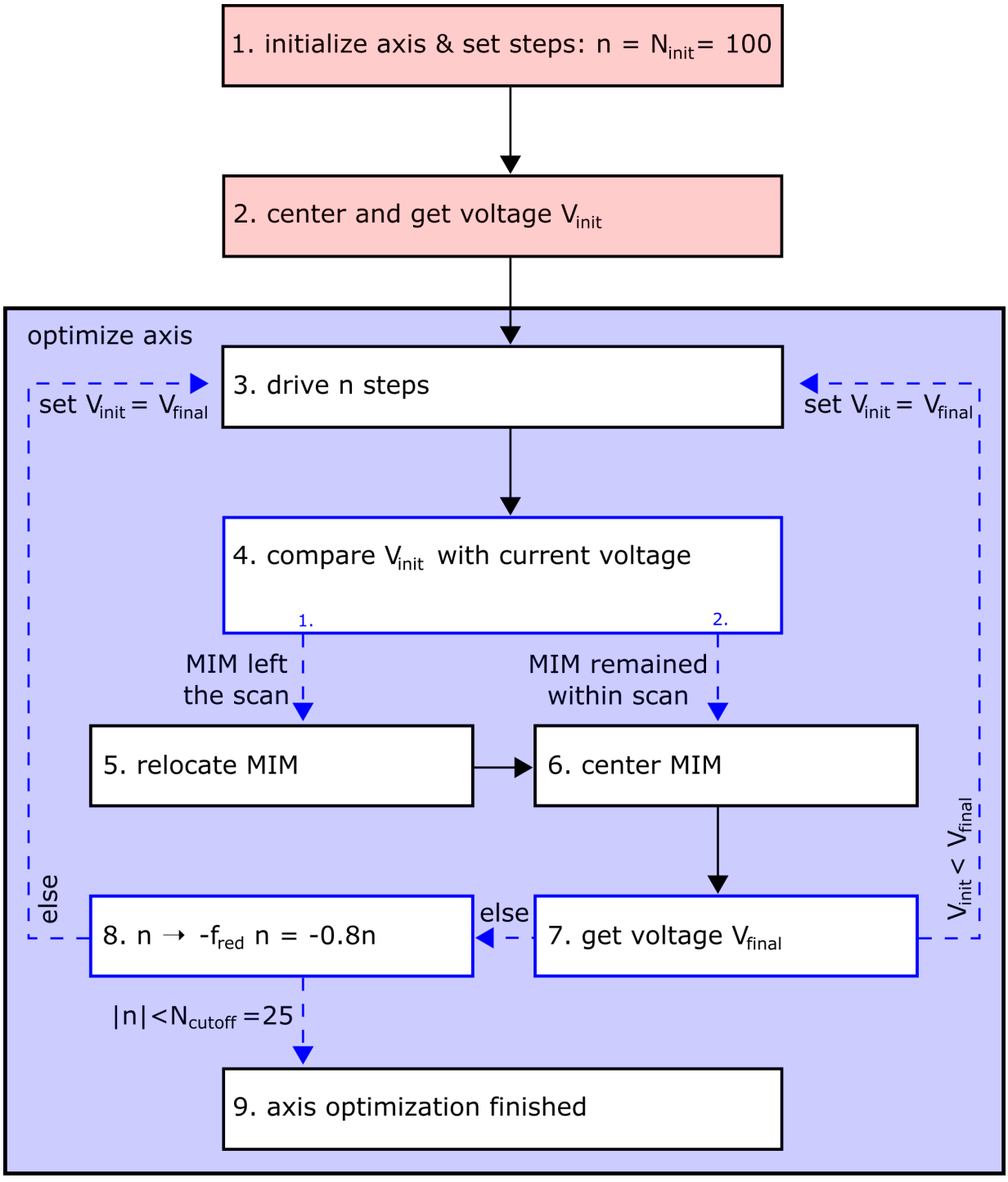

Figure 3.8: *Optimization algorithm flowchart: The dashed blue lines depict conditional paths.*

1. The algorithm cycles through all displayed steps separately for each IC and PZT mirror axis. The respective axis is initialized and the initial number of steps is set to $N_{init} = 100$.

2. The most intense mode (MIM) within the oscilloscope trace, see Figure 3.9, is determined, its position is centered with respect to the scan, and its voltage V_{init} saved. The centering process is explained in more detail in the upcoming section.

3. The previously initialized axis is now moved by n steps. This will impact the coupling of the incident mode to the resonator, as well as the resonator length. For sufficiently high n the MIM can leave the scan entirely.

4. The current MIM voltage V is compared to the initial voltage V_{init}. If $V < 0.65 V_{init}$ the algorithm determines that the mode must have left the scanning range, as $n \leq 100$ steps are not sufficient to decrease the intensity by 35%.

5. The MIM is relocated.

6. The MIM is centered.

7. The final MIM voltage V_{final} is determined and compared to V_{init} from the state before the step was made. If the voltage increased, the algorithm will loop back to step 3 and update the initial voltage. If the voltage decreased instead, the maximum is expected in the opposite direction, since the fit function is given by the coupling efficiency from Figure 2.11.

8. The algorithm will inverse the direction, reduce the step size by the reduction factor $f_{red} = 0.8$, and then loop back to step 3. If the absolute step size falls below the cutoff number of steps $N_{cutoff} = 25$, the hill climb for this axis has finished.

9. The respective axis has finished its optimization process and the process restarts for the next axis. When all axes have been optimized, the algorithm exits.

The algorithm input consists of the synchronized resonator length scan and the transmitted intensity, as produced by the oscilloscope and illustrated in Figure 3.9. This trace is then analyzed and a dictionary of modes is produced including the position within the trace, the peak intensity, and the modes width. Additionally, the cavity length, which is scanned by applying a voltage ramp to the piezo chip actuator, is analyzed to find the periodically reoccurring center position of the scanning signal within the trace.

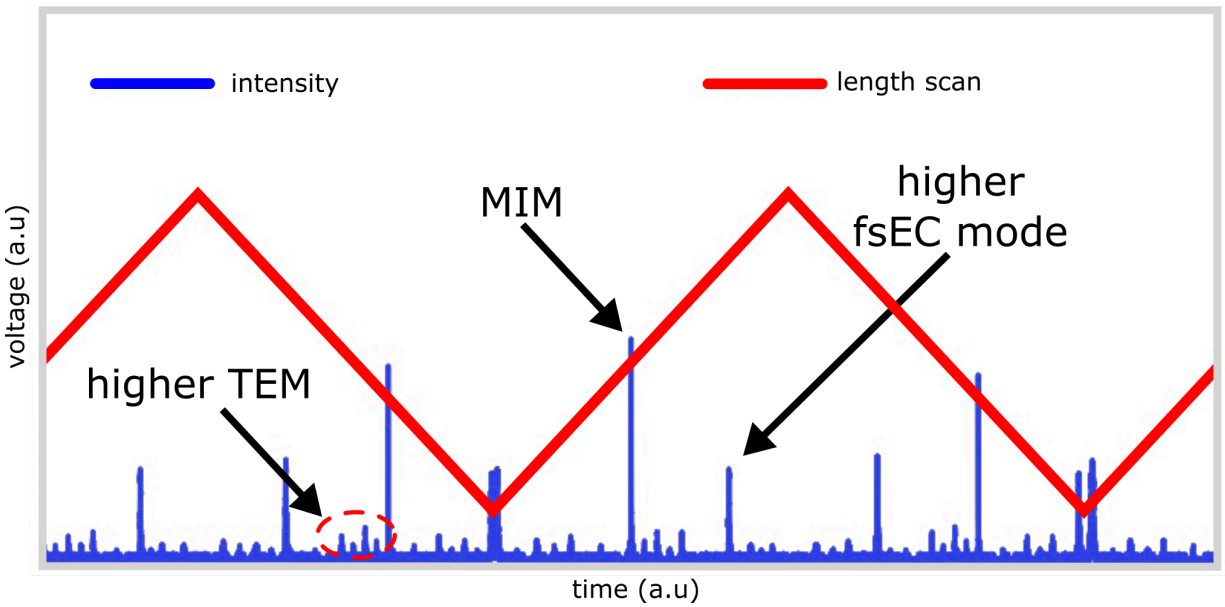

Figure 3.9: *Illustration of an oscilloscope trace: The oscilloscope trace is analyzed and the MIM voltage is determined by the algorithm. Usually, the MIM is the TEM_{00} mode. In case the algorithm starts on the higher TEM_{nm}, further displacement shifts the coupling to the $TEM_{n+1\ m+1}$, which would decrease the MIM intensity. Consequently, the direction would be reversed and the TEM_{nm} improved, until the $TEM_{n-1\ m-1}$ becomes the MIM. In this illustration the MIM is the TEM_{00} at a resonator length of L_0, which has already been centered in respect to the length scan. Also displayed are higher longitudinal fsEC modes and higher Hermite-Gaussian modes. These TEM are almost completely diminished, which implies that the resonator is well aligned. The fluctuations in intensity between the same modes at different scanning periods are largely caused by vibrations. These vibrations impact the resonator length, allowing for increased or decreased buildup of power inside the resonator. As a countermeasure, the algorithm determines the MIM voltage by averaging over multiple scanning periods. Alternatively the oscilloscopes time per division can be increased, at the cost of losing resolution.*

3.3.2 Relocation algorithm

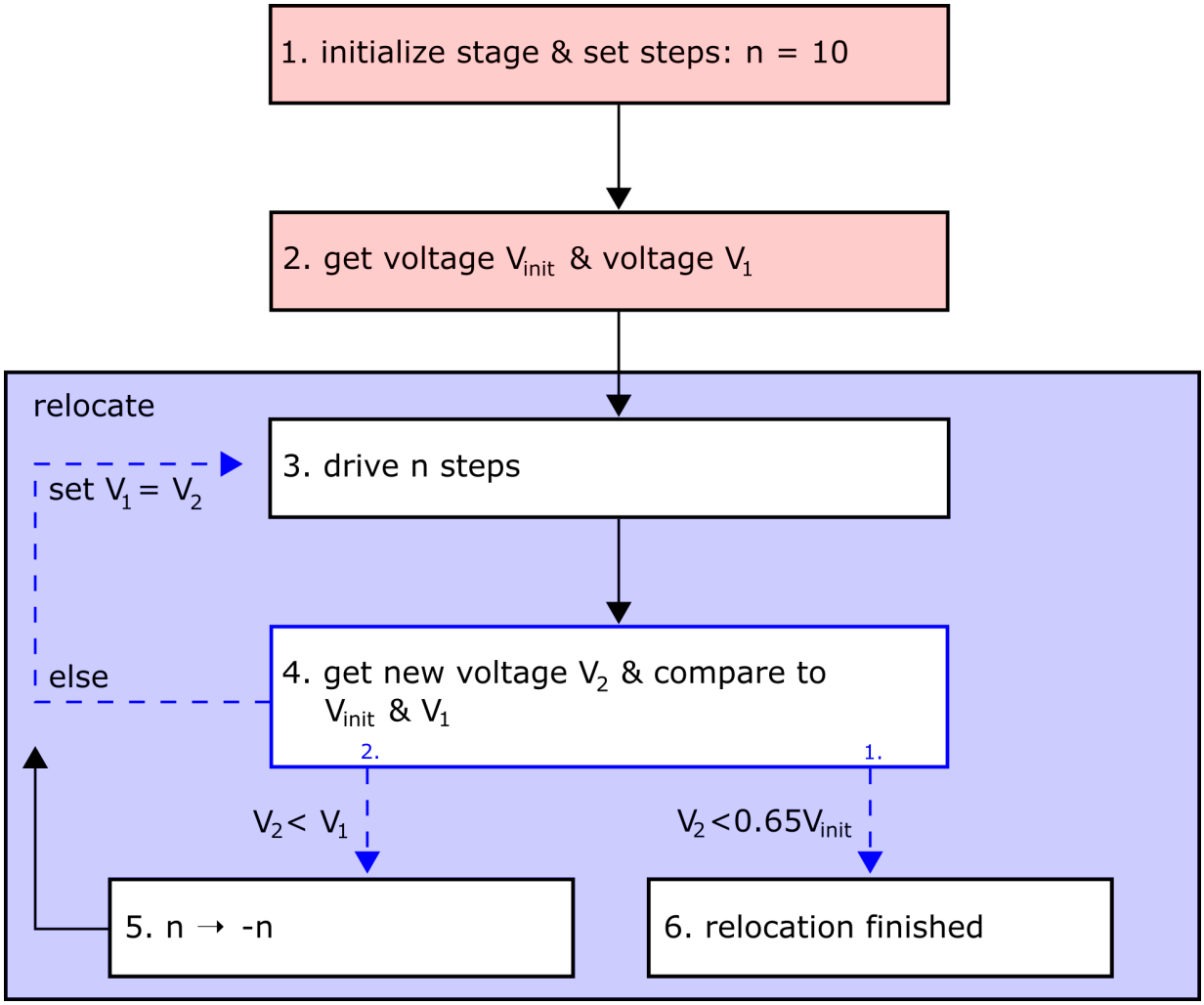

Figure 3.10: *Relocation algorithm flowchart: The relocation algorithm is a HC algorithm. It aims to relocate the MIM within the length scan by driving the resonator length, after losing the MIM, due to alignment adjustments. The dashed blue lines depict conditional paths.*

1. The relocation algorithm, as shown in Figure 3.10, begins by initializing the piezo-controlled translation stage, which is used to control the resonator length on a wider scale than the piezo chip. The number of steps to drive per iteration is set to $n = 10$.

2. The initial MIM voltage V_{init}, from before the axis was driven by the alignment optimization algorithm, is retrieved. This V_{init} is expected to be close to the MIM voltage after driving, as the mirror tilt per HC iteration is set to be sufficiently small. The relocation algorithm expects the new MIM voltage to be larger than $0.65V_{init}$. The initial MIM voltage is also saved as V_1.

3. The stage is driven by n steps. Consider the calculated intensity distribution from Figure 2.13. As the resonator length is changed by approximately the center wavelength of the frequency comb, the L_0 mode is replaced by the L_1 or L_{-1} mode as the MIM. Since the intensity decreases in both directions, another HC is applied to relocate the initial MIM.

4. The MIM voltage V_2 after driving is determined and compared to V_{init} and V_1. There are three different outcomes that need to be considered. Firstly, the algorithm checks if the initial MIM was relocated. Since it was impacted by the mirror tilt, its intensity could have either increased or decreased. The algorithm will accept an intensity decrease of up to 35%, to determine if the MIM was relocated. If the MIM was not relocated, the algorithm checks if $V_2 < V_1$, as this implies that the stage was driven in the wrong direction. Lastly, no significant change in MIM voltage is possible, if the length change was not sufficiently large, resulting in additional n steps in the same direction.

5. If the stage was driven in the wrong direction, the direction is reversed and the algorithm jumps back to step 3, after updating the voltage V_1.

6. The MIM is relocated within the length scan. Subsequently, the MIM needs to be centered within the length scan.

3.3.3 Centering algorithm

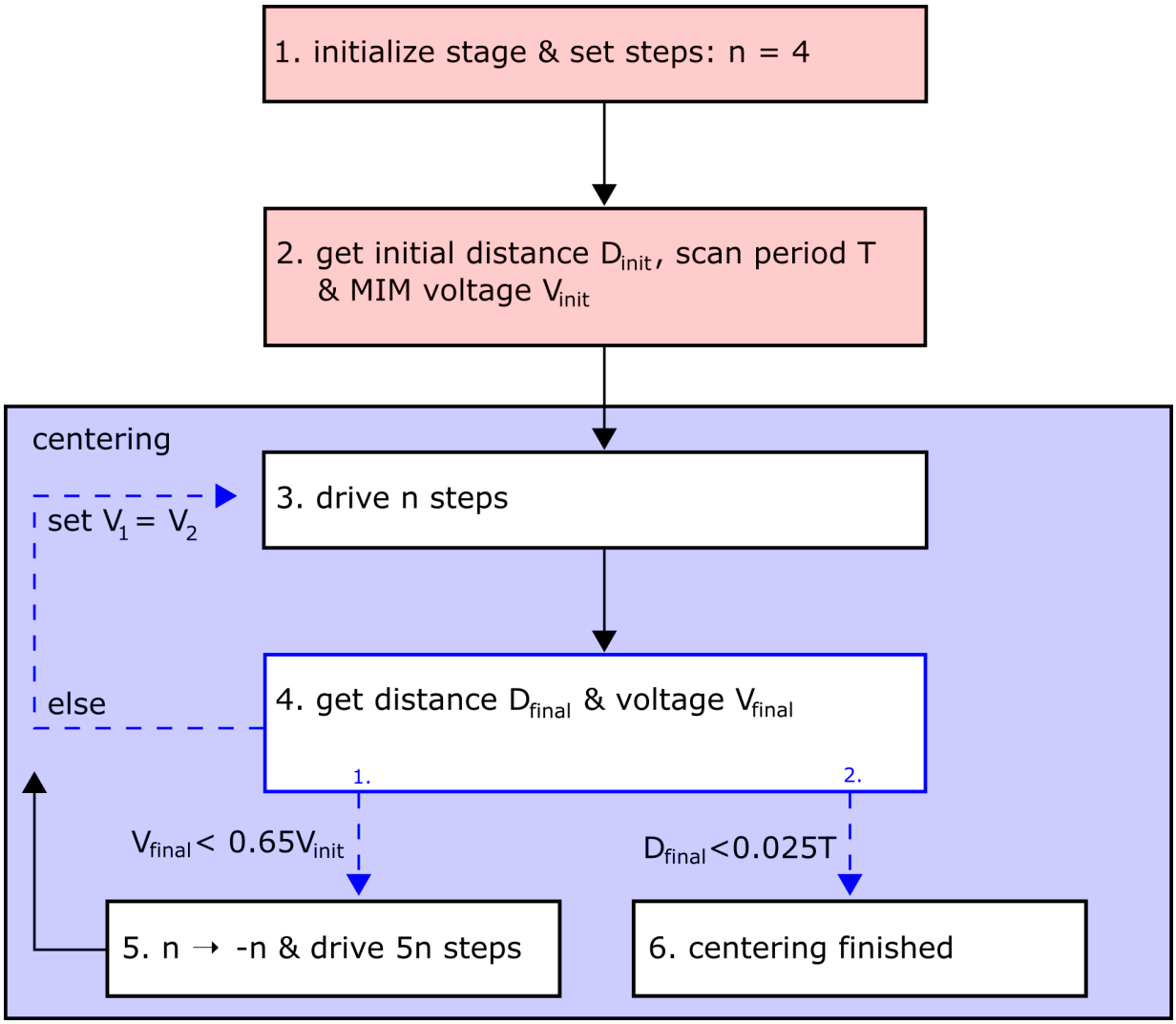

Figure 3.11: *Centering algorithm flowchart: In contrast to the alignment optimization and relocation algorithms, this algorithm searches for a minimal distance between the MIM and scan center. As before, the dashed blue lines depict conditional paths.*

1. The centering algorithm flowchart is shown in Figure 3.11. The translation stage is initialized and the number of steps to drive per iteration is set to $n = 4$.

2. The initial MIM position P_{MIM} and its closest center position P_{center} are determined. The scan itself consists of multiple center positions and the closest one to P_{MIM} is always the target position. The initial distance between both positions is calculated via $D = |P_{MIM} - P_{center}|$. The scanning period T is also retrieved for later usage. It is important to note that these positions correspond to the specific time within the oscilloscope

trace. The length scan determines the speed at which the length is scanned and consequently the time differences, referred to as distances, calculated by this algorithm.

3. The stage is moved by n steps. This will shift the resonances within the scanning range, by a smaller amount than the relocation algorithm did.

4. The centering algorithm searches for the optimal solution in one direction. If the distance increases after an iteration, the algorithm will not turn around right away. Since the search space is sufficiently small, a few steps are enough to either center the MIM or drive the MIM out of the scanning range. To determine which case set in, the final distance D_{final} and the final voltage V_{final} are analyzed.

5. If the MIM left the scanning range, the voltage will have dropped off significantly and, at more than 35% loss in voltage, the direction is reversed. To further accelerate the process, $5n$ steps are driven in the correct direction. This number was determined experimentally and shifts the MIM close to the center, resulting in faster centering.

6. As the distance between the MIM and scan center has been decreased to less than a fraction of the scanning period $D_{final} < 0.025T$, the centering has finished.

4 Analysis and discussion

4.1 Coupling efficiency

When it comes to hill climbs, the optimal fit function posses only one extremum. The coupling efficiency of the TEM_{00} provides the fit function for the hill climb optimization and was measured for each axis tilt of the IC and PZT mirrors. When a mirror is tilted, the length and resonator axis are impacted as well. Despite not altering the incident beam path, transverse displacement between resonator axis and incident beam is produced as a result, as the resonator axis changes in regard to the incident beam. Each mirror axis was tilted on purpose, driven past the optimal coupling, and stopped as soon as TEM_{10} or TEM_{01} coupling became dominant. The TEM_{00} power was measured every few steps during this measurement and the initial, optimal, and final intensity distributions were recorded, to visualize the Hermite-Gaussian modes. The coupling

mirror axis	beam width (μm)	fit parameter (step)	displacement per step ($\frac{\mu m}{step}$)
IC x	819	582 ± 13	1.40 ± 0.03
IC y	595	525 ± 19	1.13 ± 0.04
PZT x	819	277 ± 7	2.95 ± 0.07
PZT y	652	1198 ± 23	0.54 ± 0.01

Table 4.1: *Coupling efficiency calibration: The beam widths $W(z)$ are taken from the theoretical resonator geometry design and, in combination with the fit factors, the transverse displacement per step was calculated.*

efficiency was fitted to the results, as shown in Figure 4.1, and used to calibrate the transverse displacement per step made for each axis. Consider the coupling efficiency from Equation 2.59:

$$F(\mathrm{d}x) = \frac{1}{1 + (\sqrt{2}\,\mathcal{C}\,\mathrm{d}x/W(z)^2)/2}, \tag{4.1}$$

where the dimensionless transverse displacement $\mathrm{d}u$ was replace with the displacement $\mathrm{d}x$ and the transverse displacement per step $\mathcal{C} = W(z)/f$ according to:

$$\mathrm{d}u = \frac{\sqrt{2}}{W(z)}\,\mathcal{C}\,\mathrm{d}x = \frac{\sqrt{2}}{f}\mathrm{d}x, \tag{4.2}$$

with f as the fit parameter. The beam widths $W(z)$ at the mirror positions were taken from the theoretical resonator geometry design and, consequently, the transverse displacement per step could be determined as depicted in Table 4.1. These results need to be viewed critically. In the derivation for the coupling efficiency it was assumed that the transverse displacement stays significantly smaller than the beam width. The measurement and fit reach beyond that estimation, where a deviation from Equation 2.59 becomes evident, most likely caused by higher order coupling. This measurement

however confirms that the fitness function for the hill climb has a single maximum for displacements up to $1000\ \mu$m.

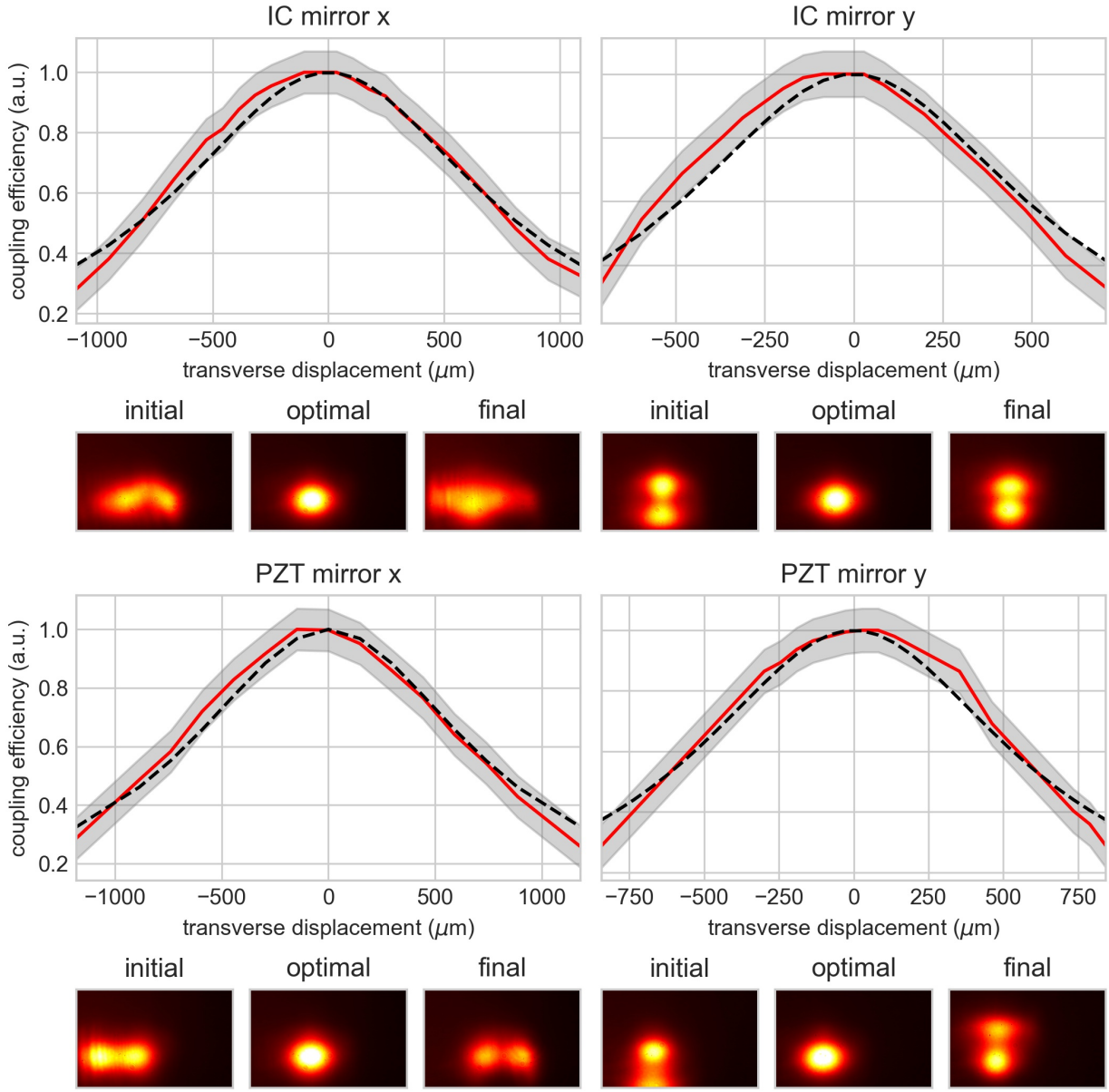

Figure 4.1: *Coupling efficiency calibration: In red the measured coupling efficiency of the TEM_{00}, as a function of the displacement, is shown. The black dashed line visualizes the fitted coupling efficiency. At initial, optimal, and final alignment, the intensity distributions were recorded and coupling to the TEM_{01} and the TEM_{10} is evident. The misalignment of the IC mirror x-axis resulted in diffraction, as the beam started to graze another setup element, manifesting itself as vertical lines in the distorted intensity distribution. These distortions did not affect the measured TEM_{00}.*

4.2 Length shifts due to axis tilts

When an axis is tilted, the resonator length is slightly affected as a byproduct. As a result, the scanning range is shifted and the desired modes, which are produced inside the fsEC at L_0, are no longer resonant within the scanning range. When it comes to the MIM, a higher longitudinal mode can replace the desired mode. This effect was measured and is shown in Figure 4.2, where the x-axis of the IC mirror was tilted by 100 ± 5 steps and thus a transverse displacement of 140 ± 8 μm was produced. The HC algorithm will automatically correct these shifts via the relocation algorithm.

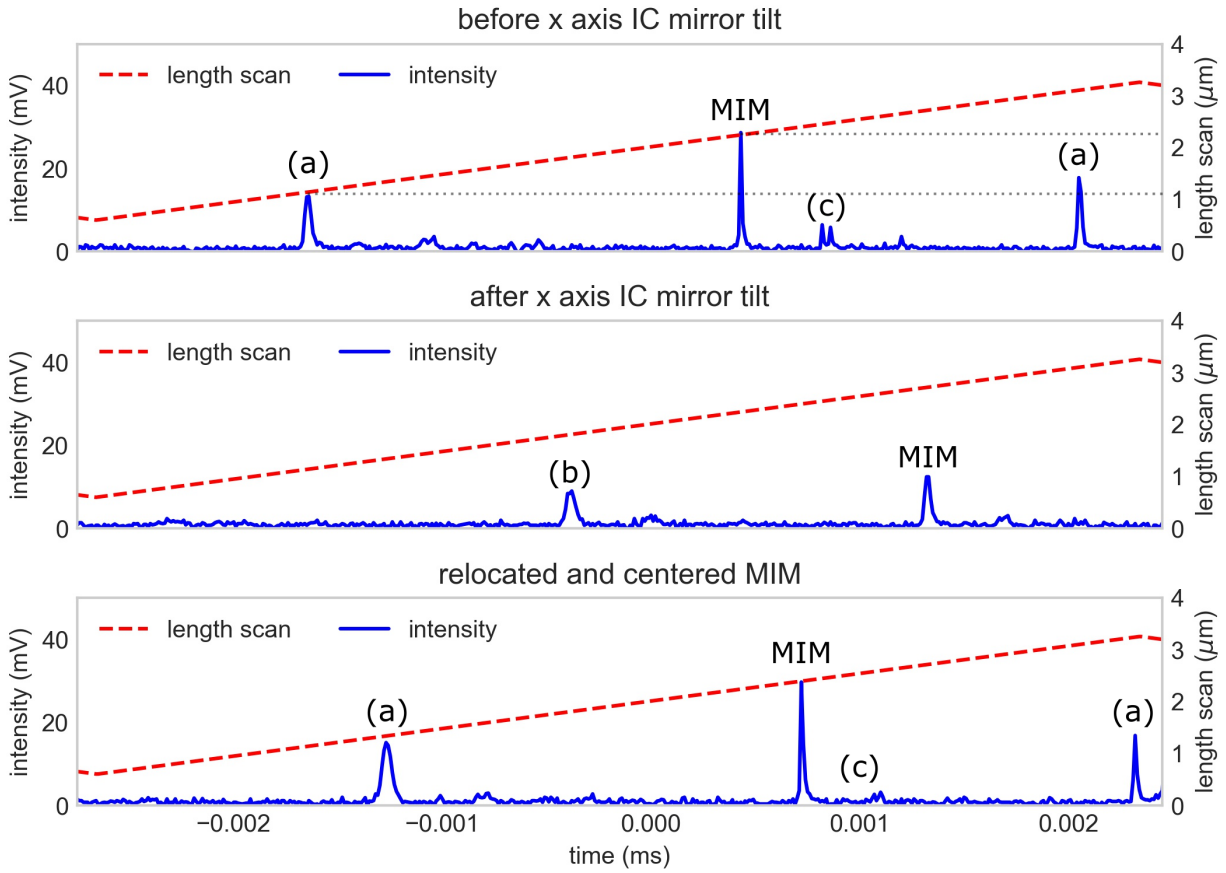

Figure 4.2: *Resonance shift cause by tilting the x-axis of the IC mirror by* 100 *steps: The laser operates at a central wavelength of* $\lambda_c = 1040$ *nm, which equals the spacing (dotted lines) between the fsEC modes. These longitudinal modes are marked with (a) and (b), corresponding to* $L_{\pm 1}$ *and* $L_{\pm 2}$*, respectively. Note the broadening of these longitudinal modes, as discussed in the theory section. The spacing between the TEM modes, marked with (c), is significantly smaller, as it depends on the Gouy phase and consequently on the mirror spacing, as calculated in Equation 2.38. After tilting the mirror, the* $L_{\pm 1}$ *mode replaces the* L_0 *mode as MIM. The resonator length shift is corrected utilizing the PZT mirror translation stage and the initial resonances are recovered and recentered after 40 steps. The higher TEM mode (c) is visibly reduced by this process, since the x-axis tilt improved the alignment.*

4.3 Length scan hysteresis effects

The resonator length is constantly swept by a piezo chip during the HC optimization process. Therefore, the centering algorithm is crucial, as the piezo element that scans the resonator length is prone to hysteresis effects. Additionally, towards the edges of the scan the linearity of the scan is impacted. Both effects manifest themselves in less resonator length change towards the edges of the scan, allowing for an increased buildup of power inside the resonator. The intensity can increase significantly, as shown in Figure 4.3. Since the optimization process strongly depends on comparing the same mode before and after each iteration, the algorithm centers the mode before determining its intensity. Failing to do so will significantly impair the algorithm, as will be presented in more detail in the following section. Vibrations can have a similar effect and are compensated for, by averaging over 3 traces per oscilloscope readout.

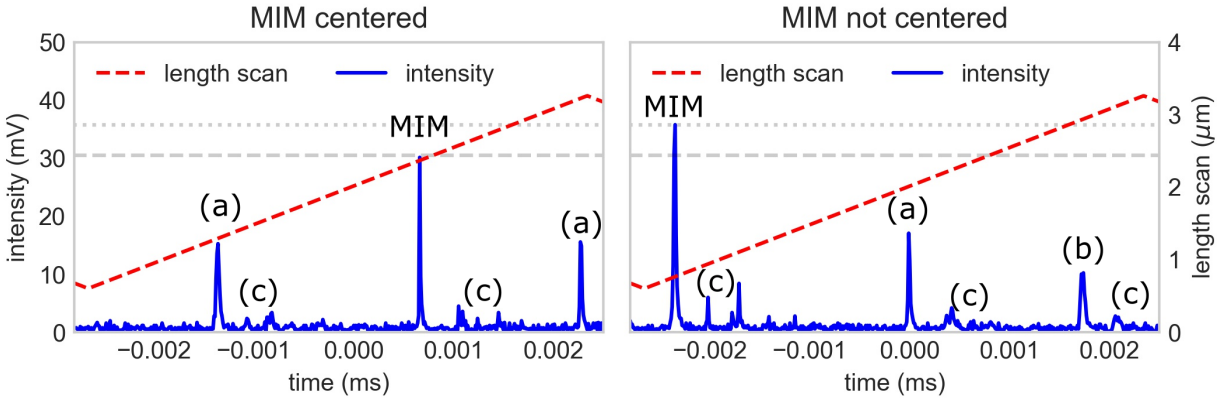

Figure 4.3: *Mode intensity at different positions within the length scan: Higher longitudinal modes are marked with (a) and (b), corresponding to $L_{\pm1}$ and $L_{\pm2}$, respectively. The TEM for $n+m=1$ and $n+m=2$ are marked with (c). Here the MIM voltage increased by $\sim 18\%$, due to not being centered. Additionally, it can be seen that vibrations caused the $L_{\pm1}$ mode to increase slightly in intensity.*

4.4 Hill climb optimization

The hill climb algorithm was applied to 11 different initial states, to highlight various challenges that had to be tackled by the algorithm. The intensity of the MIM was tracked, as well as the number steps made, the oscilloscope traces, and the intensity distribution of the modes. The optimizations were analyzed with respect to the iterations each optimization required, rather than their runtime. The number of iterations per optimization is unaffected by adaptions in data acquisition or processing speed. The typical runtime per optimization for the setup employed in this thesis ranges around $20 - 30$ min, limited by the readout time of the oscilloscope. The length scan amplitude before amplification was set to $U_{scan} = 2$. The initial number of steps, number of steps cutoff, and reduction factor were set to $N_{init} = 100$, $N_{cutoff} = 25$, and $f_{red} = 0.8$, respectively. The error for the mode intensities was determined to be ± 15 mV. The step error was determined to be $\pm 5\%$. The power of the incident beam varied between measurements, which does not impact the optimization process. A few measurements were selected, to illustrate the process and will be discussed in detail.

4.4.1 Optimization 1: Strong x-axis and y-axis misalignment

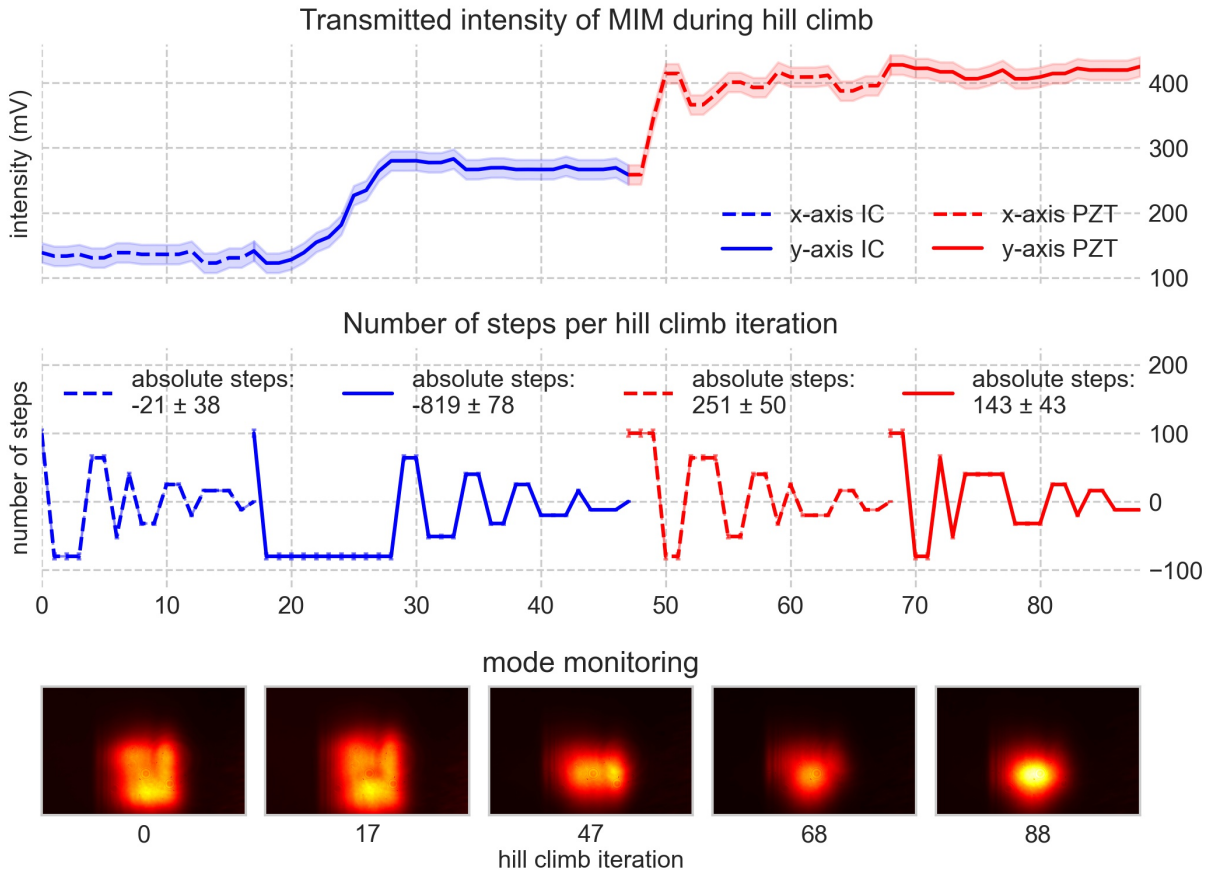

Figure 4.4: *Optimization 1: The uppermost figure displays the intensity increase of the Gaussian mode during the HC. In the middle, the steps per iteration are depicted along with the absolute steps. Lastly, the intensity distributions are displayed. Considerable alignment improvement can be observed especially for the y-axis of the IC mirror and the x-axis of the PZT mirror.*

Optimization 1 is visualized in Figure 4.4 and Figure 4.5. It stands out with the most misaligned initial state between all 11 optimizations. This is reflected in the largest number of iterations and largest intensity gain for this measurement.

The algorithm started with the IC mirror. No significant improvement could be achieved for the x-axis, as can be seen by comparing the initial intensity distribution with the intensity distribution after $N_{iter} = 17$ iterations. This is also reflected in the number of total steps made of $N_{steps} = -21 \pm 38$, which effectively implies no change in alignment within one sigma. Continuing with the y-axis, compared to the x-axis, almost double the amount of iterations $N_{iter} = 30$ were required, as this axis allowed for significant alignment improvement after a total of $N_{steps} = -819 \pm 78$ steps. The mode monitoring confirms this considerable improvement, by portraying the reduction of higher TEM

contributions. Figure 4.5 nicely visualizes the increase in TEM_{00} and TEM_{10} intensity, as well as the decrease in intensity of higher Hermite-Gaussian modes during the optimization of the IC mirror y-axis.

The algorithm continues with the PZT mirror. The x-axis allows for additional optimization by decreasing the intensity of the TEM_{10}. After $N_{iter} = 21$ iterations and $N_{steps} = -251 \pm 50$ steps this axis is optimized. Finally, a small adjustment to the y-axis of the PZT mirror is made, ending the optimization process. The algorithm adjusted the last axis by $N_{steps} = -143 \pm 43$ steps after $N_{iter} = 20$ iterations. The final intensity distribution mode monitoring appears misleadingly more intense than its predecessor, considering the minimal rise in intensity. This is likely linked to the integration time of the camera. As the integration time is set to roughly span one scanning period, a slight mismatch can lead to the same mode being captured twice in the same frame, thus resulting in more intensity. To conclude the first optimization, a significant increase in intensity of the Gaussian mode of $(304 \pm 34)\%$ was achieved within 88 iterations, demonstrating the successful application of the HC algorithm to the alignment optimization problem posed in this thesis.

Figure 4.5 gives more information on the input parameters of the optimization algorithm. The initial resonances are all of similar intensity and the algorithm struggles to distinguish these, especially while centering or relocating or when strong intensity fluctuations are present. The oscilloscope traces do also emphasize the decrease in intensity of higher Hermite-Gaussian modes. Especially the PZT mirror y-axis seems to have little influence on the desired Gaussian mode on first glance. Nonetheless, the HC diminished the TEM_{nm} coupling, with $n + m = 2$. Figure 4.4 shows quick ascents in intensity before plateauing, especially for the y-axis of the IC mirror. Two factors take part in this outcome: firstly, the minimal step size of $N_{cutoff} = 25$, which is reached after turning around eight times, and secondly the reduction factor of $f_{red} = 0.8$, by which the step size is decreased. The optimal setting of both depends on the stability and sensitivity of the resonator. A higher minimal step size can be chosen, if small amounts of steps have less effect on the intensity than vibrations do. The rate at which the step size decreases needs to be adjusted, to efficiently correct when overshooting the optimal position. Adjusting these parameters can decrease the total amount of iterations that are required to optimize the alignment, since plateauing can be avoided. The following measurements will partly present optimization without plateauing, which verifies the choice of parameters, despite occasional plateauing.

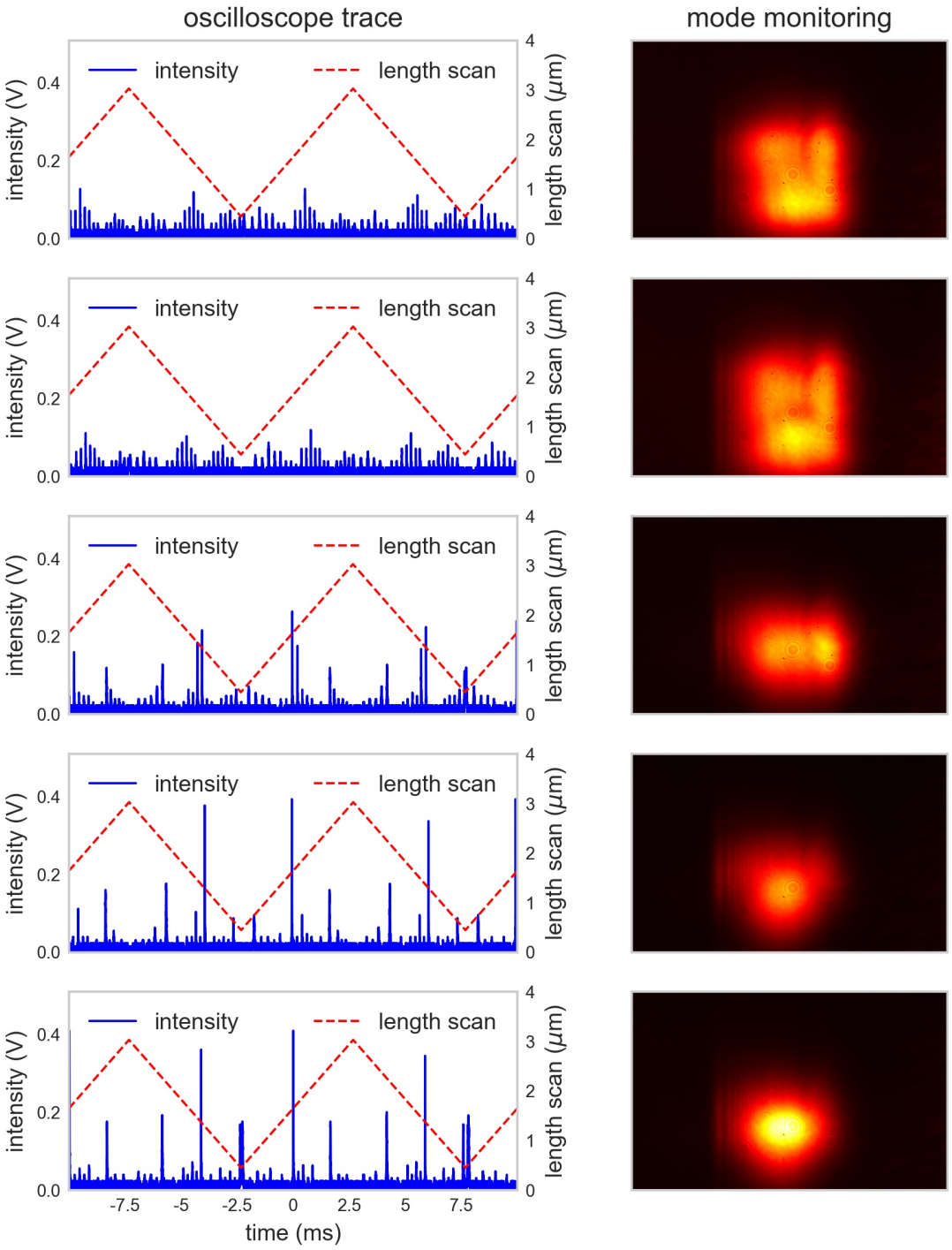

Figure 4.5: *Optimization* 1*: Oscilloscope traces: The left figures show the oscilloscope traces after each axis optimization, while the mode is being monitored on the right. The impact of optimizing the y-axis of the IC mirror and the x-axis of the PZT mirror is shown in row* 2*,* 3*, and* 4*. The traces do not just visualize the increase in intensity of the Gaussian mode, but also how the higher modes are being diminished.*

4.4.2 Optimization 2: Initially non-Gaussian MIM

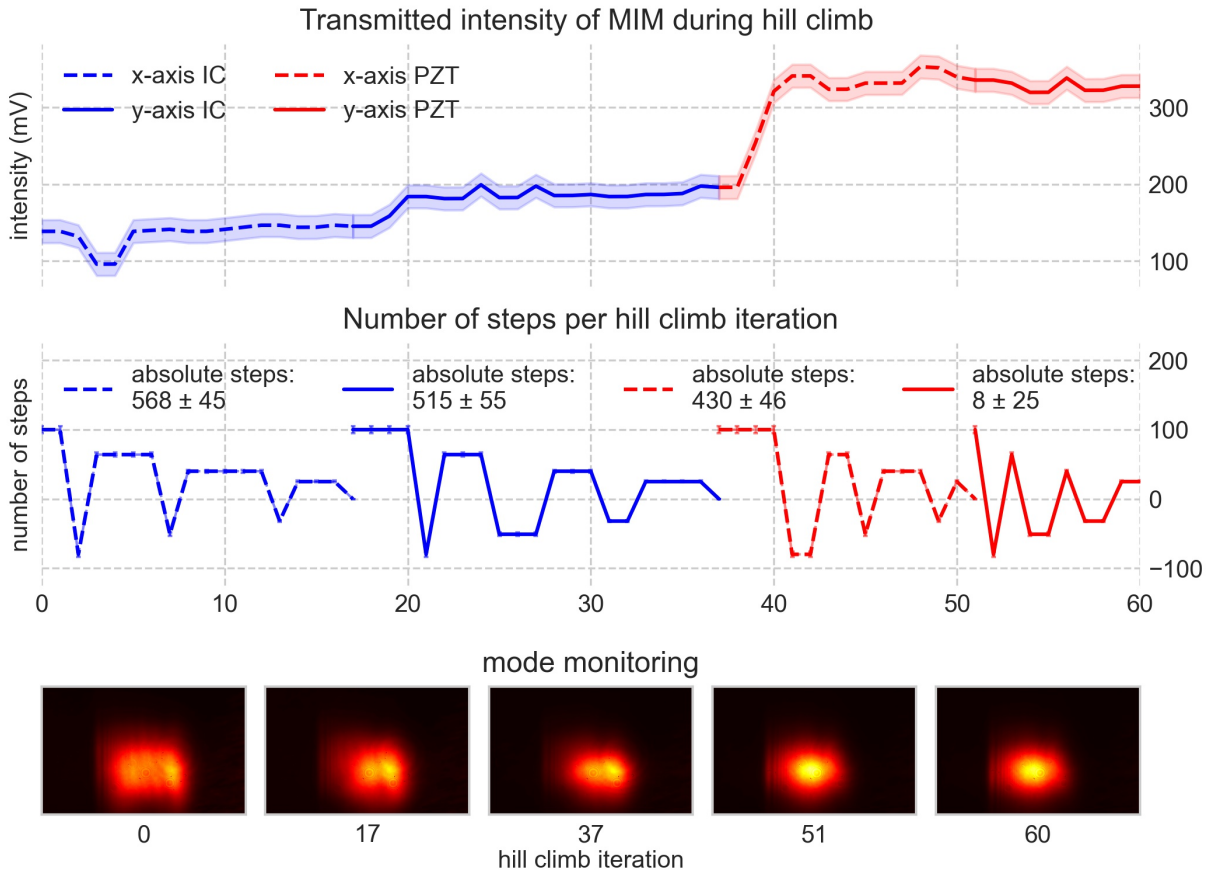

Figure 4.6: *Optimization 2: The initial intensity distribution consists mainly of higher TEM along the x-axis. The TEM_{10} is depleted when the x-axis of the PZT mirror is optimized, resulting in a dominant Gaussian mode.*

Figure 4.6 and 4.7 depict the second optimization. The initial intensity distribution consists mainly of higher TEM along the x-axis. This optimization started out with the TEM_{10} as MIM. Within the first $N_{iter} = 17$ iterations the Gaussian mode becomes the MIM, showing that the algorithm can correct the alignment when starting on the wrong MIM. This behavior can also be noticed in the first and third optimization.

The algorithm starts with the x-axis of the IC mirror, driving a total of $N_{steps} = 568 \pm 45$ steps. The MIM intensity seems to increase only slightly. The oscilloscope traces reveal that the initial MIM is not Gaussian, but rather a TEM mode with $n + m = 1$. As the alignment is adjusted, the desired Gaussian mode overtakes this TEM mode in intensity. The mode monitoring confirms, that initially the TEM_{10} is most dominant and after $N_{iter} = 17$ iterations the Gaussian mode takes over. Hereafter, the y-axis is optimized. Although neither the mode monitoring nor the MIM intensity show significant improvement, a total amount of $N_{steps} = 515 \pm 55$ steps were driven after $N_{iter} = 20$.

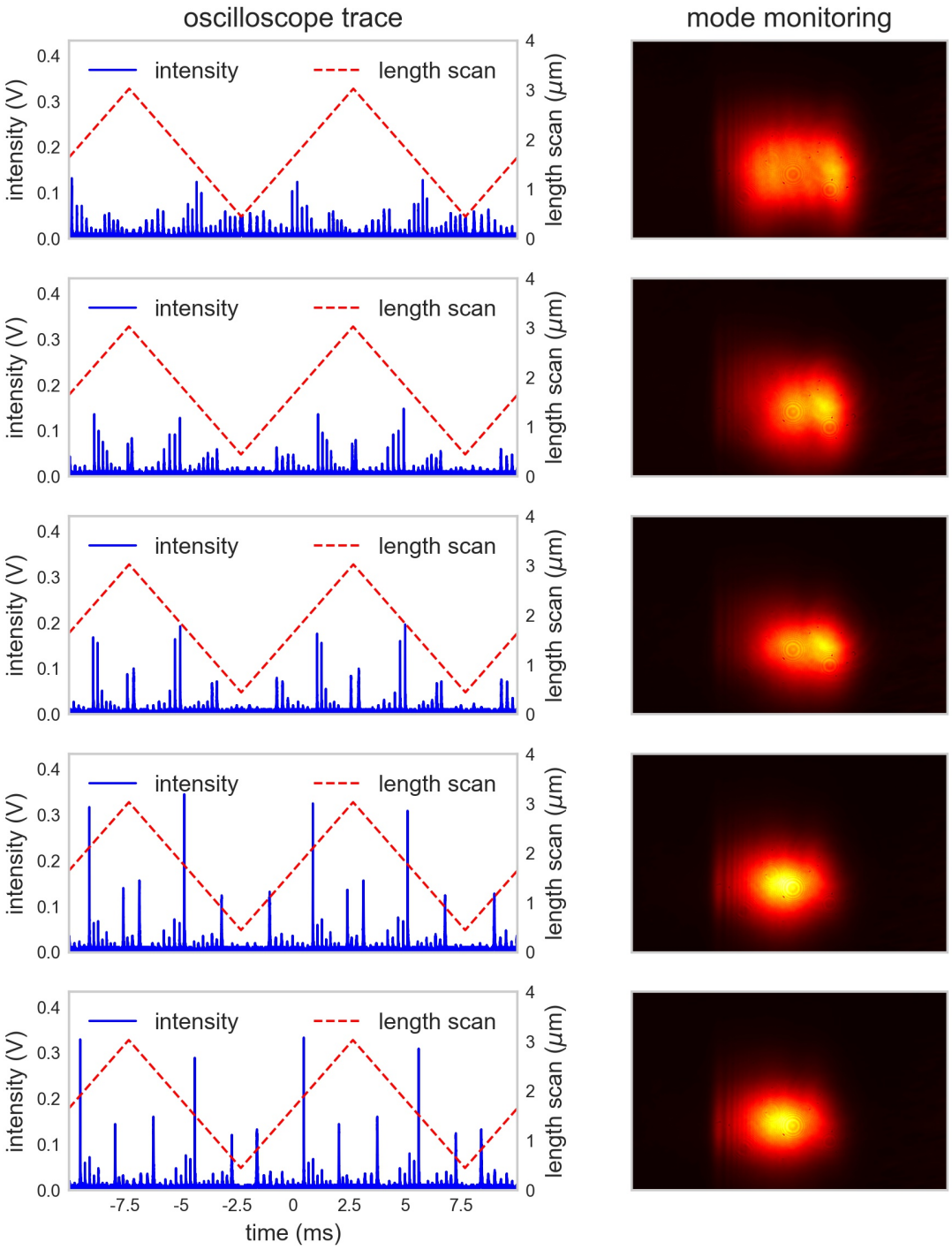

Figure 4.7: *Optimization 2: Oscilloscope traces: The first two axes impact the initial intensity only slightly, while shifting the MIM to the Gaussian mode and depleting higher TEM. The optimization of the last axis shows no improvement.*

The corresponding trace, shown in Figure 4.7, shows a slight increase in MIM intensity, while higher TEM with a sum of $n + m > 1$ were decreased significantly.

The subsequent x-axis optimization of the PZT mirror leads to the most dominant increase in intensity during this optimization. It strongly depletes the intensity of the TEM_{01} after $N_{steps} = 430 \pm 46$ and $N_{iter} = 14$. The algorithm moves to the last axis, where it is unable to achieve any additional improvement. After only $N_{iter} = 9$ iterations and $N_{steps} = 8 \pm 25$ the HC finishes.

This optimization required less iterations to find the optimized state after $N_{iter} = 60$ compared to the $N_{iter} = 88$ from the first optimization. This results from the more optimized initial state of the alignment. The optimization of the first two axes show, that the HC settings of $N_{cutoff} = 25$ and $f_{red} = 0.8$ are appropriate, despite the plateauing in intensity during the optimization of other axes.

4.4.3 Optimization 3 & 4: Importance of the centering algorithm

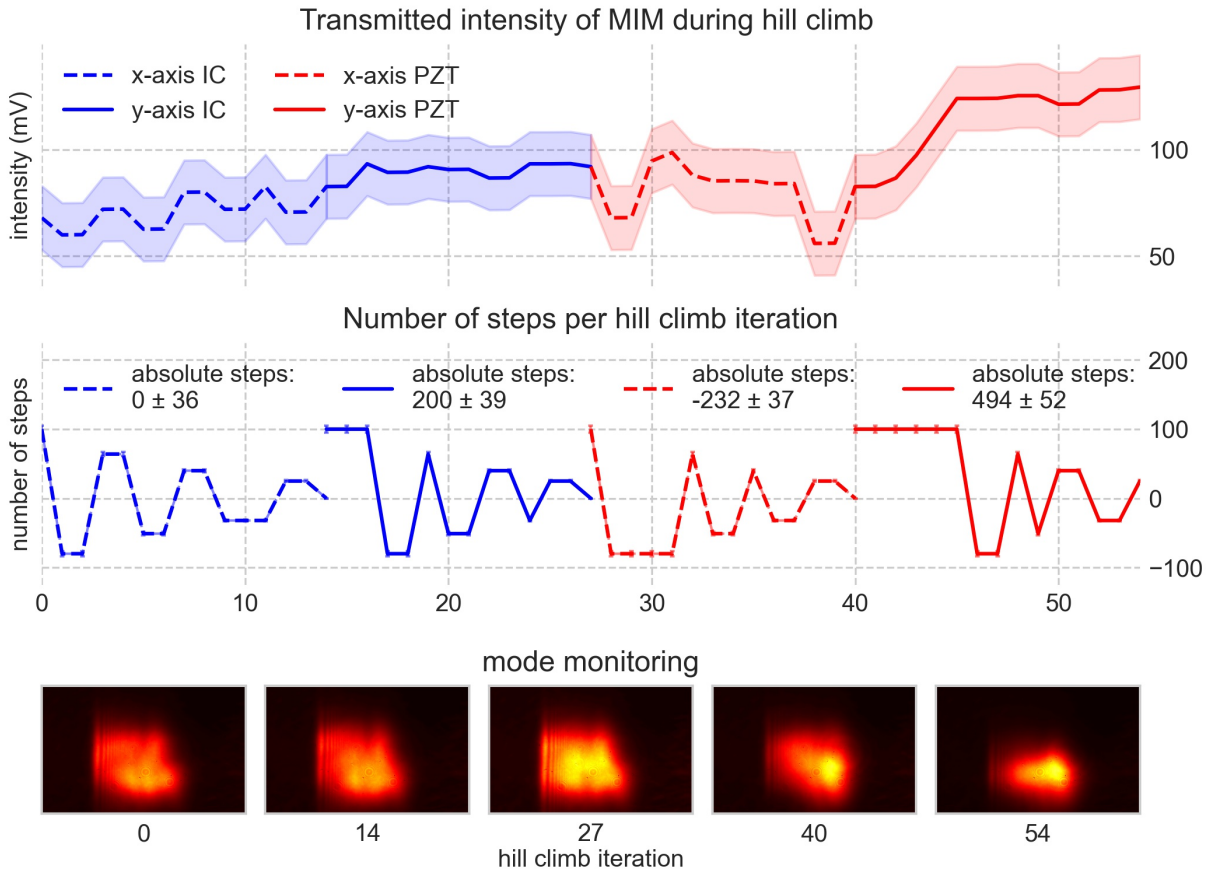

Figure 4.8: *Optimization 3: The algorithm is unable to center a MIM with a voltage of less than 100 mV. Despite this hindrance the algorithm manages to optimize the alignment.*

Optimization 3 and 4 emphasize the importance of the centering algorithm. As the voltage of the MIM was initially too low for the centering algorithm, optimization 3 ran without centering until a MIM voltage of more than 100 mV was achieved. This measurement is shown in Figure 4.8. The subsequent optimization 4 is depicted in Figure 4.9. Both measurements stand out, since they display the importance of the centering algorithm, as well as the effectiveness of repeated optimizations.

Both optimizations together achieved an increase of $(538 \pm 121)\%$ from the initial intensity of (68 ± 15) mV to the final intensity of (366 ± 15) mV. The x-axis optimization of the the IC mirror during optimization 3 significantly diminishes higher TEM and does not plateau right away as opposed to earlier measurements, again confirming that the HC settings are chosen appropriately.

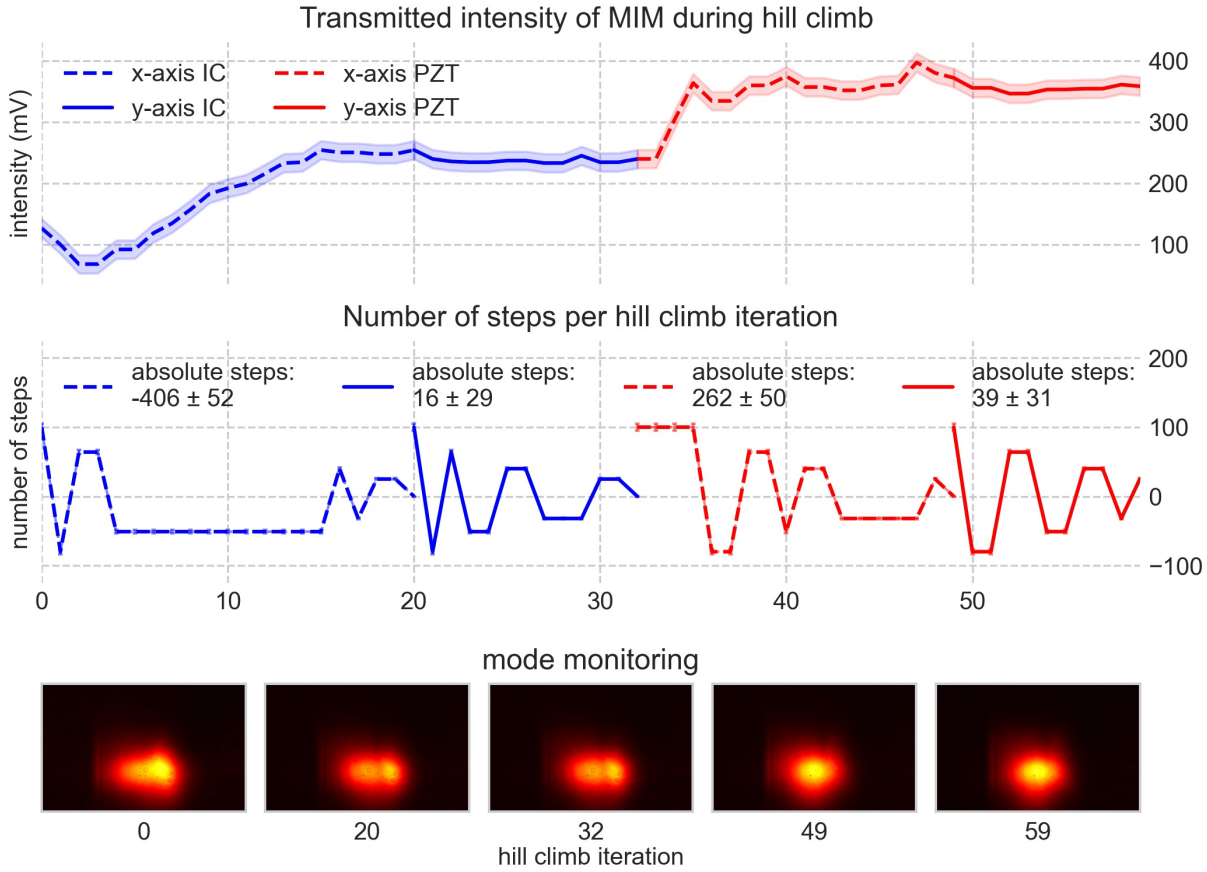

Figure 4.9: *Optimization 4: Optimization 3 is being continued in this optimization. Since the MIM voltage exceeds 100 mV, the algorithm is able to center, as opposed to measurement 3. Note that the last axis was already aligned properly, as the previous optimization already optimized this axis.*

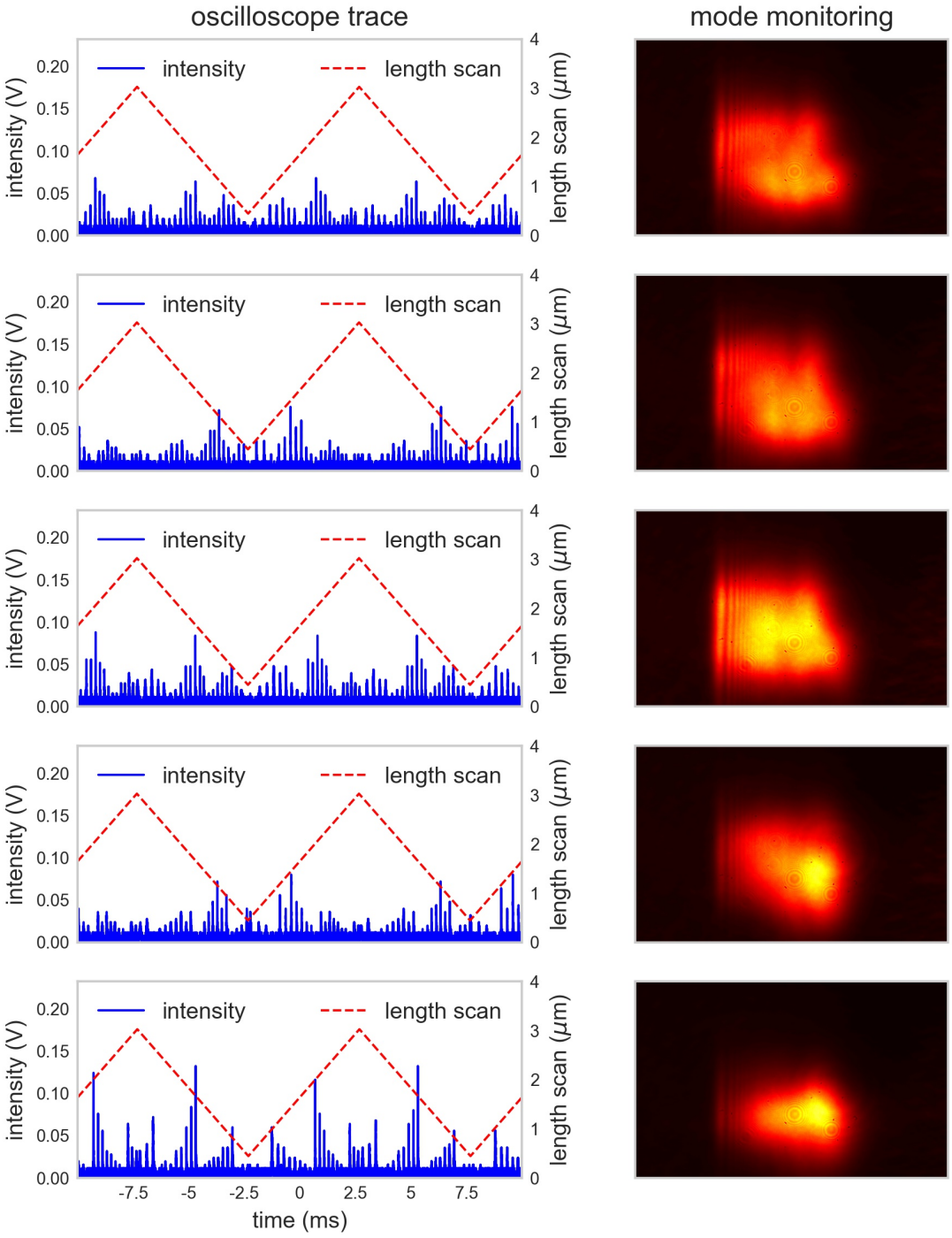

Figure 4.10: *Optimization 3: Oscilloscope traces: The optimization of the y-axis of the PZT mirror shifts the MIM from a higher TEM to the TEM_{00}, achieving sufficient MIM intensity for the relocation algorithm. As a consequence, the algorithm is able to center the MIM in the subsequent iterations.*

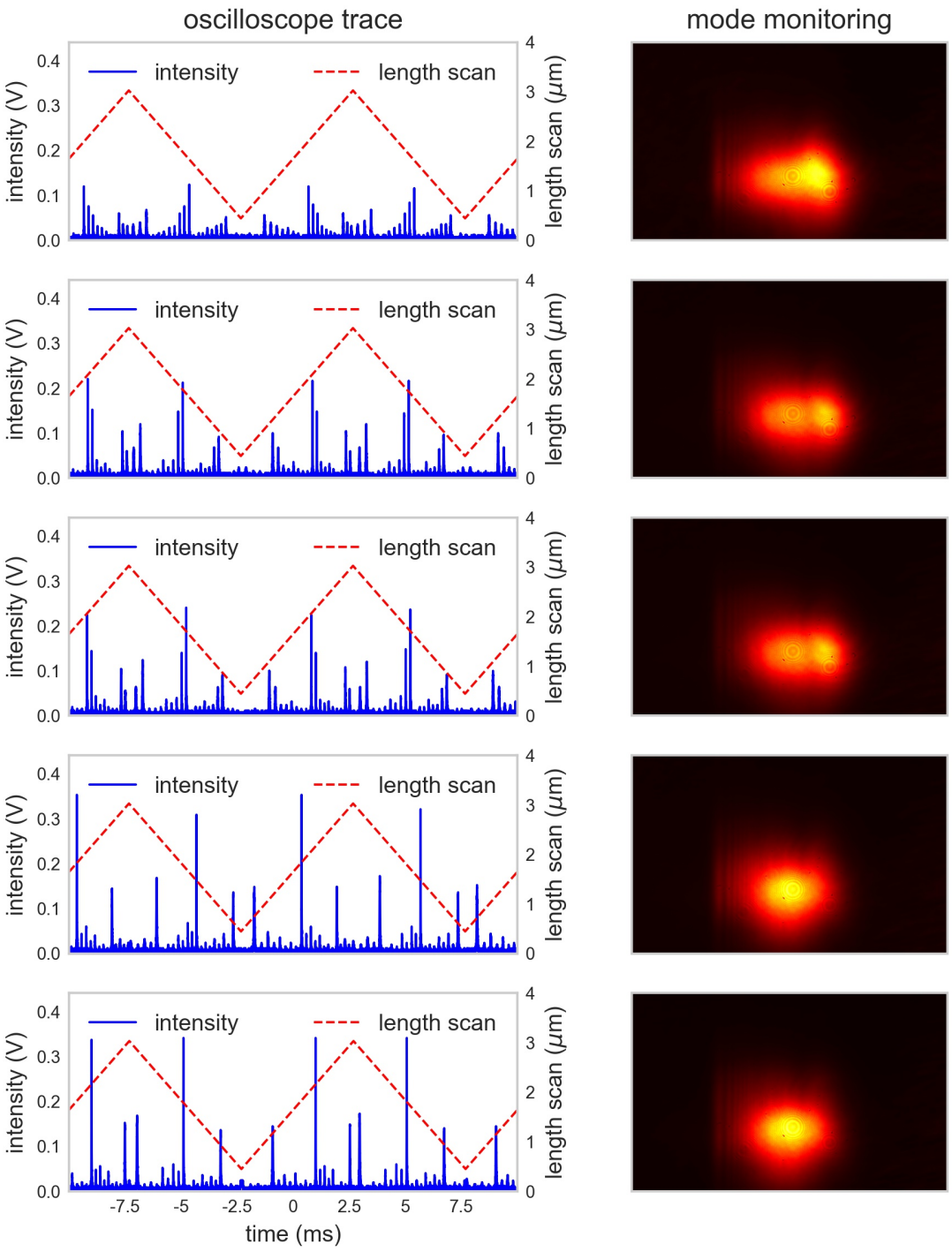

Figure 4.11: *Optimization* 4*: Oscilloscope traces: Optimization* 3 *is being continued in this optimization. Since the MIM voltage exceeds* 100 *mV, the algorithm is able to center, as opposed to optimization* 3*.*

4.4.4 Optimization 5: Improving a manually aligned mode

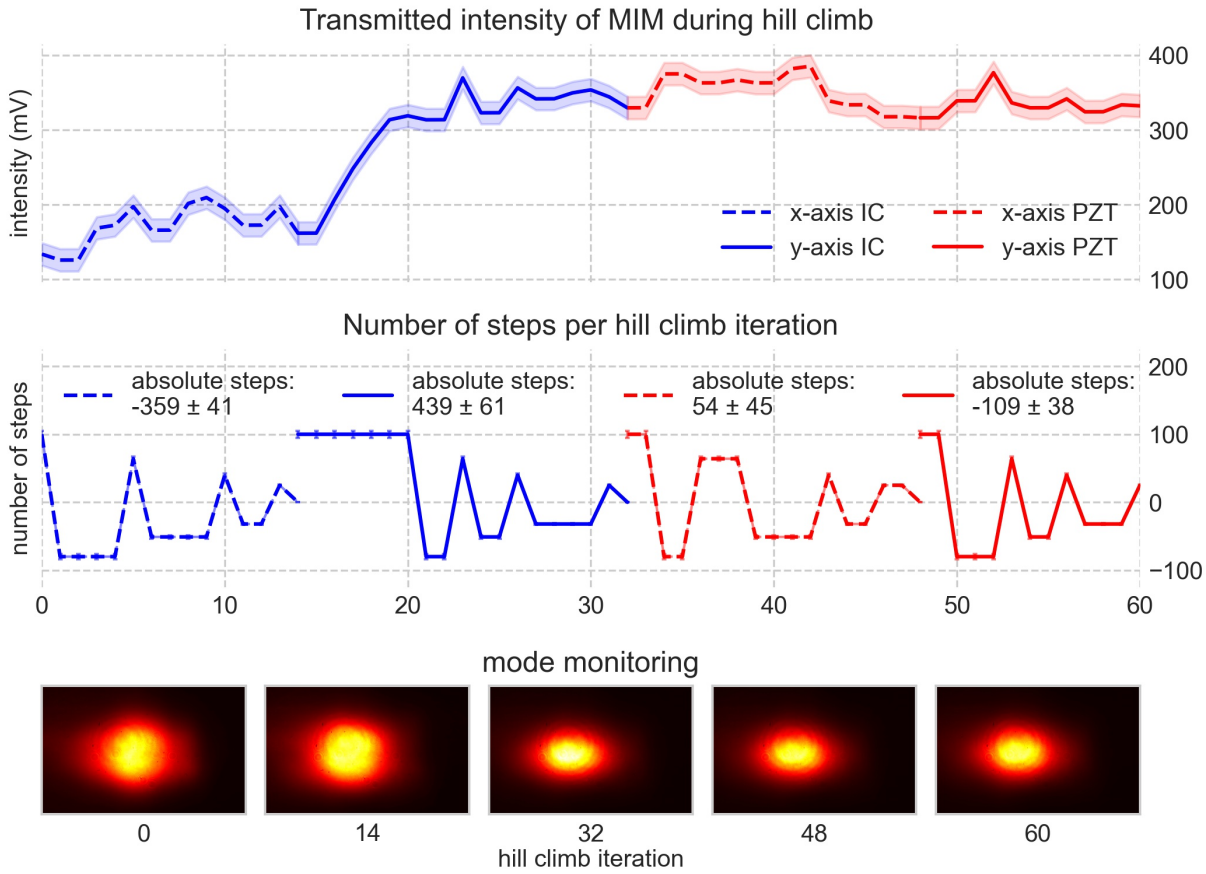

Figure 4.12: *Optimization 5: The initial alignment was manually adjusted.*

Optimization 5 presents the improvement of a previously manually aligned mode. Figure 4.12 depicts the initial intensity distribution. It becomes apparent, that the initial mode was adjusted manually, without consideration of the oscilloscope trace or astigmatism, which leads to a oval TEM_{00} at the mode monitoring. A gain of $(222 \pm 27)\%$ was achieved after $N_{iter} = 60$. This results in a gain per iteration of $(3.7 \pm 0.5)\%$, which lies above the average of the 11 optimizations that were recorded. This measurement highlights the difficulty of manual adjustments to the resonator alignment.

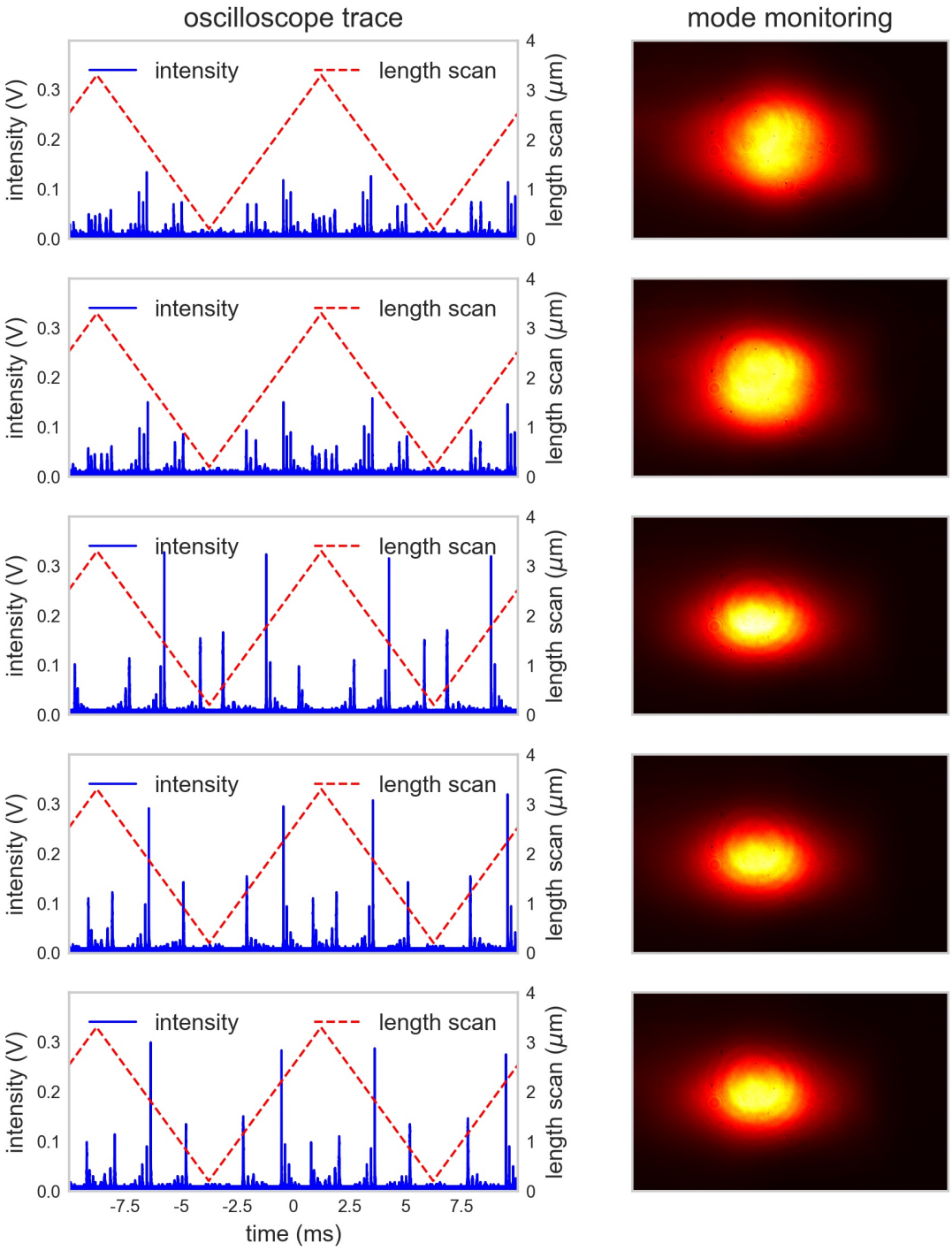

Figure 4.13: *Optimization 5: Oscilloscope traces: The trace visualizes the higher mode contributions, which are not as noticeable in the intensity distribution.*

4.4.5 Overview

In total 11 measurements were conducted. The first four measurements were ran at ambient pressure, while all consequent measurements were performed at UHV conditions. The initial and final intensity and intensity distributions are shown in Figure 4.14. Each optimization was successful in increasing the MIM intensity. Table 4.2 provides an overview of all measurements. The average gain strongly depends on the initial state of the setup, since an already optimized alignment does not allow for much gain. The number of iterations depends partly on the initial position, with a lowest possible number of iterations based on the initial step size, the reduction factor, and the number of steps cutoff. Therefore the gain per iteration provides a more reliable quantity, as it depends less on the initial state. The average gain per iteration over all measurements was calculated to be $(3.4 \pm 0.4)\%$. Note that the optimized alignment still contains higher TEM mode residue. This is largely a consequence of misaligned optical elements, which guide the beam into the fsEC and cannot be influenced by IC or PZT mirror adjustments.

measurement	initial MIM intensity (mV)	final MIM intensity (mV)	gain (%)	total iterations	gain per iteration (%)
1	139 ± 15	422 ± 15	304 ± 34	88	3.5 ± 0.4
2	139 ± 15	336 ± 15	242 ± 28	60	4.0 ± 0.5
3	68 ± 15	125 ± 15	184 ± 46	54	3.4 ± 0.9
4	127 ± 15	366 ± 15	288 ± 36	59	4.9 ± 0.6
5	370 ± 15	394 ± 15	106 ± 6	45	2.4 ± 0.1
6	134 ± 15	298 ± 15	222 ± 27	60	3.7 ± 0.5
7	303 ± 15	310 ± 15	102 ± 7	48	2.1 ± 0.1
8	129 ± 15	307 ± 15	238 ± 30	58	4.1 ± 0.5
9	129 ± 15	316 ± 15	245 ± 31	58	4.2 ± 0.5
10	177 ± 15	199 ± 15	112 ± 13	49	2.3 ± 0.3
11	228 ± 15	299 ± 15	131 ± 11	51	2.6 ± 0.2
average	$----$	$----$	198 ± 25	57	3.4 ± 0.4

Table 4.2: *HC optimization overview: The table depicts the initial intensity, final intensity, gain, total iterations, and gain per iteration for all measurements. Measurement* 1 *was the longest measurement with* $N_{iter} = 88$ *iterations and the highest gain. The shortest measurement finished after only* $N_{iter} = 45$ *iterations, showing almost no improvement.*

To conclude, the successful application of a hill climb optimization algorithm to the alignment problem of a fsEC was demonstrated. An average gain per iteration of $(3.4 \pm 0.4)\%$ was presented for $N_{init} = 100$, $N_{cutoff} = 25$, and $f_{red} = 0.8$ at a total of

11 measurements. It was also demonstrated that repeated measurements can further optimize the alignment. Figure 4.14 visualizes the improvement in intensity distribution for each measurement, showing that the optimization algorithm is able to optimize a wide range of initial settings, including intensity distributions that include diffraction patterns.

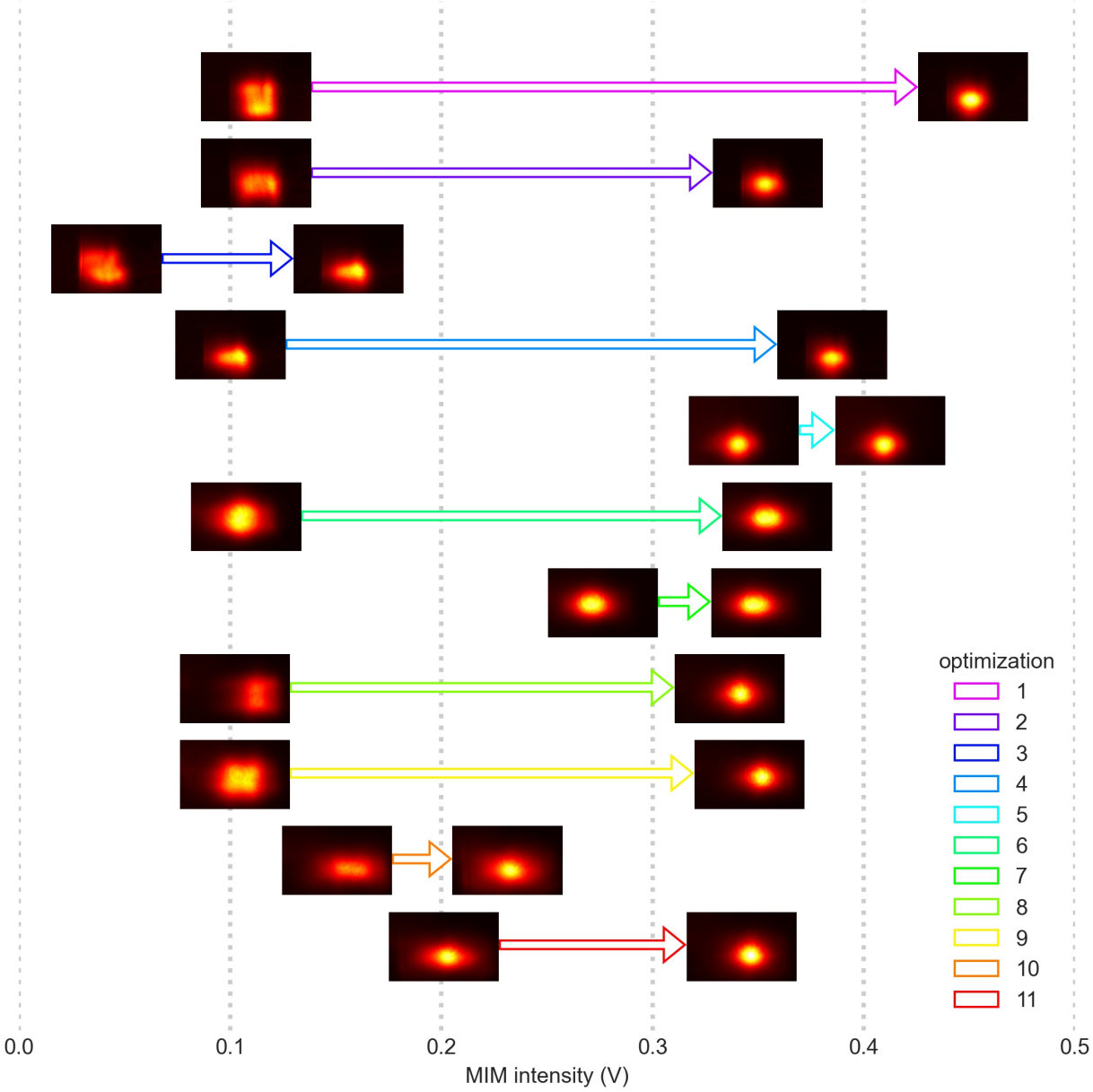

Figure 4.14: *HC optimization overview: The initial and final intensity of each measurement along with the intensity distributions are depicted. Various initial couplings were corrected, despite present diffraction patterns.*

5 Outlook

In this thesis the effective implementation of a HC optimization application has been presented and as it stands, further advances are within reach. A decrease in iterations per optimization, less residue of higher TEM in the final alignment, and specific mode selection are feasible.

The two most time consuming factors are the readout process of the oscilloscope, in regard to processing speed, and the relocation and centering of the MIM, when it comes to the time per iteration. The acquisition of the synchronized signal, consisting of the transmitted intensity and resonator length scan, could be directly read out from the corresponding sources, bypassing the oscilloscope. Regarding the time per iteration, the resonator length change could be reduced by implementing mirrors that rotate about the incidence point of the beam. Furthermore, goniometer and generally the precise determination of mirror tilts, would allow for less length change and the implementation of a GA for the optimization.

Currently two mirror tilts, namely the IC mirror and the PZT mirror, are being optimized. Expansion to further optical elements, such as the mode-matching telescope, would provide a cleaner end result, as higher TEM coupling could be further suppressed. Additionally, vibrations and fluctuations in laser intensity influence and limit the ability to optimize the alignment. Further decoupling of the optical setup from the UHV pumps might allow for more precision.

Finally, specific mode selection could be achieved. As the TEM are degenerate within the scan for equal sums of order, mode decomposition through the intensity distribution would be required for higher mode selection. "Overlapping" the camera images with theoretical calculations requires precise knowledge of the theoretical beam shape at the camera position, including tilts and astigmatism. After decreasing the optimization time, mode decomposition could be implemented without pushing optimization times to multiple hours.

6 Acknowledgments

I feel more than content with the results I have achieved during my time at the Max Planck Institute for Nuclear Physics. I have grown as a person and as a scientist, and am grateful to the people who stood by my side and made the COVID-19 pandemic more durable. I want to show special appreciation to:

Janko Nauta and Jan-Hendrik Oelmann,
who both had the patience to explain the intricacy of the experiment to me and also had the confidence in me to let me operate autonomous at our project. It was a pleasure to work with you.

Tobias Heldt and Nick Lackmann,
and everybody else, who took their time to proofread my thesis.

Moto Togawa,
who has always been an outstanding and grounding presence in my life. Thank you for letting me bounce countless ideas off of you, thank you for the discussions about physics, and last but certainly not least the amazing friendship over the years and hopefully years to come. I have learned a lot from you.

Khrystyna Totska,
for motivating and believing in me. Thank you for being at my side and supporting my ideas.

References

[1] M. Tanabashi et al. "Review of Particle Physics". In: *Phys. Rev. D* 98 (3 Aug. 2018), p. 030001. DOI: 10.1103/PhysRevD.98.030001. URL: https://link.aps.org/doi/10.1103/PhysRevD.98.030001.

[2] A. Einstein. "Die Feldgleichungen der Gravitation". In: *Sitzungsberichte der Königlich Preußischen Akademie der Wissenschaften (Berlin)* (1915), pp. 844–847.

[3] Planck Collaboration et al. "Planck 2015 results - I. Overview of products and scientific results". In: *A&A* 594 (2016), A1. DOI: 10.1051/0004-6361/201527101. URL: https://doi.org/10.1051/0004-6361/201527101.

[4] Saul Perlmutter. "Nobel Lecture: Measuring the acceleration of the cosmic expansion using supernovae". In: *Rev. Mod. Phys.* 84 (3 Aug. 2012), pp. 1127–1149. DOI: 10.1103/RevModPhys.84.1127. URL: https://link.aps.org/doi/10.1103/RevModPhys.84.1127.

[5] Andrei D Sakharov. "Violation of CP invariance, C asymmetry, and baryon asymmetry of the universe". In: *Soviet Physics Uspekhi* 34.5 (May 1991), pp. 392–393. DOI: 10.1070/pu1991v034n05abeh002497. URL: https://doi.org/10.1070/pu1991v034n05abeh002497.

[6] ATLAS Collaboration et al. "Observation of a new particle in the search for the Standard Model Higgs boson with the ATLAS detector at the LHC". In: *Physics Letters B* 716.1 (2012), pp. 1–29. ISSN: 0370-2693. DOI: https://doi.org/10.1016/j.physletb.2012.08.020. URL: https://www.sciencedirect.com/science/article/pii/S037026931200857X.

[7] David DeMille, John M Doyle, and Alexander O Sushkov. "Probing the frontiers of particle physics with tabletop-scale experiments". In: *Science (New York, N.Y.)* 357.6355 (Sept. 2017), pp. 990–994. ISSN: 0036-8075. DOI: 10.1126/science.aal3003. URL: https://doi.org/10.1126/science.aal3003.

[8] M. S. Safronova, D. Budker, D. DeMille, Derek F. Jackson Kimball, A. Derevianko, and Charles W. Clark. "Search for new physics with atoms and molecules". In: *Reviews of Modern Physics* 90.2 (June 2018). ISSN: 1539-0756. DOI: 10.1103/revmodphys.90.025008. URL: http://dx.doi.org/10.1103/RevModPhys.90.025008.

[9] P. A. M. Dirac. "A New Basis for Cosmology". In: *Proceedings of the Royal Society of London Series A* 165.921 (Apr. 1938), pp. 199–208. DOI: 10.1098/rspa.1938.0053.

[10] E. A. Milne. "Relativity, Gravitation, and World-Structure". In: *Philosophy* 11.41 (1936), pp. 95–97.

[11] V. V. Flambaum. "Variation of Fundamental Constants". In: *AIP Conference Proceedings* (2006). ISSN: 0094-243X. DOI: 10.1063/1.2400630. URL: http://dx.doi.org/10.1063/1.2400630.

[12] J. K. Webb, J. A. King, M. T. Murphy, V. V. Flambaum, R. F. Carswell, and M. B. Bainbridge. "Indications of a Spatial Variation of the Fine Structure Constant". In: *Physical Review Letters* 107.19 (Oct. 2011). ISSN: 1079-7114. DOI: 10.1103/physrevlett.107.191101. URL: http://dx.doi.org/10.1103/PhysRevLett.107.191101.

[13] P. Tzanavaris, M. Murphy, John Webb, Victor Flambaum, and Stephen Curran. "Probing variations in fundamental constants with radio and optical quasar absorption-line observations". In: *Monthly Notices of the Royal Astronomical Society* 374 (Nov. 2006). DOI: 10.1111/j.1365-2966.2006.11178.x.

[14] Jonathan B. Whitmore and Michael T. Murphy. "Impact of instrumental systematic errors on fine-structure constant measurements with quasar spectra". In: *Mon. Not. Roy. Astron. Soc.* 447.1 (2015), pp. 446–462. DOI: 10.1093/mnras/stu2420. arXiv: 1409.4467 [astro-ph.IM].

[15] J. C. Berengut and V. V. Flambaum. "Manifestations of a spatial variation of fundamental constants in atomic and nuclear clocks, Oklo, meteorites, and cosmological phenomena". In: *EPL (Europhysics Letters)* 97.2 (Jan. 2012), p. 20006. ISSN: 1286-4854. DOI: 10.1209/0295-5075/97/20006. URL: http://dx.doi.org/10.1209/0295-5075/97/20006.

[16] J Terrien. "News from the International Bureau of Weights and Measures". In: *Metrologia* 4 (1968), pp. 41–45. DOI: 10.1088/0026-1394/4/1/006.

[17] P. O. Schmidt, T. Rosenband, C. Langer, W. M. Itano, J. C. Bergquist, and D. J. Wineland. "Spectroscopy Using Quantum Logic". In: *Science* 309.5735 (2005), pp. 749–752. ISSN: 0036-8075. DOI: 10.1126/science.1114375. eprint: https://science.sciencemag.org/content/309/5735/749.full.pdf. URL: https://science.sciencemag.org/content/309/5735/749.

[18] T. Rosenband, D. B. Hume, P. O. Schmidt, C. W. Chou, A. Brusch, L. Lorini, W. H. Oskay, R. E. Drullinger, T. M. Fortier, J. E. Stalnaker, S. A. Diddams, W. C. Swann, N. R. Newbury, W. M. Itano, D. J. Wineland, and J. C. Bergquist. "Frequency Ratio of Al+ and Hg+ Single-Ion Optical Clocks; Metrology at the 17th Decimal Place". In: *Science* 319.5871 (2008), pp. 1808–1812. ISSN: 0036-8075. DOI: 10.1126/science.1154622. eprint: https://science.sciencemag.org/content/319/5871/1808.full.pdf. URL: https://science.sciencemag.org/content/319/5871/1808.

[19] H. G. Dehmelt. "Monoion oscillator as potential ultimate laser frequency standard". In: *IEEE Transactions on Instrumentation and Measurement* IM-31.2 (1982), pp. 83–87. DOI: 10.1109/TIM.1982.6312526.

[20] D. J. Wineland, Wayne M. Itano, J. C. Bergquist, and Randall G. Hulet. "Laser-cooling limits and single-ion spectroscopy". In: *Phys. Rev. A* 36 (5 Sept. 1987), pp. 2220–2232. DOI: 10.1103/PhysRevA.36.2220. URL: https://link.aps.org/doi/10.1103/PhysRevA.36.2220.

[21] V. A. Dzuba, V. V. Flambaum, and J. K. Webb. "Calculations of the relativistic effects in many-electron atoms and space-time variation of fundamental constants". In: *Physical Review A* 59.1 (Jan. 1999), pp. 230–237. ISSN: 1094-1622. DOI: 10.1103/physreva.59.230. URL: http://dx.doi.org/10.1103/PhysRevA.59.230.

[22] M. G. Kozlov, M. S. Safronova, J. R. Crespo López-Urrutia, and P. O. Schmidt. "Highly charged ions: Optical clocks and applications in fundamental physics". In: *Rev. Mod. Phys.* 90 (4 Dec. 2018), p. 045005. DOI: 10.1103/RevModPhys.90.045005. URL: https://link.aps.org/doi/10.1103/RevModPhys.90.045005.

[23] J. C. Berengut, V. A. Dzuba, V. V. Flambaum, and A. Ong. "Highly charged ions withE1,M1, andE2 transitions within laser range". In: *Physical Review A* 86.2 (Aug. 2012). ISSN: 1094-1622. DOI: 10.1103/physreva.86.022517. URL: http://dx.doi.org/10.1103/PhysRevA.86.022517.

[24] J. C. Berengut, V. A. Dzuba, and V. V. Flambaum. "Enhanced Laboratory Sensitivity to Variation of the Fine-Structure Constant using Highly Charged Ions". In: *Phys. Rev. Lett.* 105 (12 Sept. 2010), p. 120801. DOI: 10.1103/PhysRevLett.105.120801. URL: https://link.aps.org/doi/10.1103/PhysRevLett.105.120801.

[25] J. C. Berengut, V. A. Dzuba, V. V. Flambaum, and A. Ong. "Optical Transitions in Highly Charged Californium Ions with High Sensitivity to Variation of the Fine-Structure Constant". In: *Phys. Rev. Lett.* 109 (7 Aug. 2012), p. 070802. DOI: 10.1103/PhysRevLett.109.070802. URL: https://link.aps.org/doi/10.1103/PhysRevLett.109.070802.

[26] M. S. Safronova, V. A. Dzuba, V. V. Flambaum, U. I. Safronova, S. G. Porsev, and M. G. Kozlov. "Highly Charged Ions for Atomic Clocks, Quantum Information, and Search for α variation". In: *Phys. Rev. Lett.* 113 (3 July 2014), p. 030801. DOI: 10.1103/PhysRevLett.113.030801. URL: https://link.aps.org/doi/10.1103/PhysRevLett.113.030801.

[27] Andrei Derevianko, V. A. Dzuba, and V. V. Flambaum. "Highly Charged Ions as a Basis of Optical Atomic Clockwork of Exceptional Accuracy". In: *Phys. Rev. Lett.* 109 (18 Oct. 2012), p. 180801. DOI: 10.1103/PhysRevLett.109.180801. URL: https://link.aps.org/doi/10.1103/PhysRevLett.109.180801.

[28] S. Schiller. "Hydrogenlike Highly Charged Ions for Tests of the Time Independence of Fundamental Constants". In: *Phys. Rev. Lett.* 98 (18 Apr. 2007), p. 180801. DOI: 10.1103/PhysRevLett.98.180801. URL: https://link.aps.org/doi/10.1103/PhysRevLett.98.180801.

[29] Morton A Levine, R E Marrs, J R Henderson, D A Knapp, and Marilyn B Schneider. "The Electron Beam Ion Trap: A New Instrument for Atomic Physics Measurements". In: *Physica Scripta* T22 (Jan. 1988), pp. 157–163. DOI: 10.1088/0031-8949/1988/t22/024. URL: https://doi.org/10.1088/0031-8949/1988/t22/024.

[30] Sven Bernitt. "Resonante Anregung astrophysikalischer Röntgen-Übergänge in hochgeladenen Eisenionen mit dem Freie-Elektronen-Laser LCLS". In: (Apr. 2013). DOI: https://doi.org/10.11588/heidok.00015218. URL: http://www.ub.uni-heidelberg.de/archiv/15218.

[31] L. Schmöger, O. O. Versolato, M. Schwarz, M. Kohnen, A. Windberger, B. Piest, S. Feuchtenbeiner, J. Pedregosa-Gutierrez, T. Leopold, P. Micke, A. K. Hansen, T. M. Baumann, M. Drewsen, J. Ullrich, P. O. Schmidt, and J. R. Crespo López-Urrutia. "Coulomb crystallization of highly charged ions". In: *Science* 347.6227 (2015), pp. 1233–1236. ISSN: 0036-8075. DOI: 10.1126/science.aaa2960. eprint: https://science.sciencemag.org/content/347/6227/1233.full.pdf. URL: https://science.sciencemag.org/content/347/6227/1233.

[32] P. Micke, T. Leopold, S. A. King, E. Benkler, L. J. Spieß, L. Schmöger, M. Schwarz, J. R. Crespo López-Urrutia, and P. O. Schmidt. "Coherent laser spectroscopy of highly charged ions using quantum logic". In: *Nature* 578.7793 (Jan. 2020), pp. 60–65. ISSN: 1476-4687. DOI: 10.1038/s41586-020-1959-8. URL: http://dx.doi.org/10.1038/s41586-020-1959-8.

[33] D. W. Allan. "Statistics of atomic frequency standards". In: 1966.

[34] Sonja Bernitt, Gregory Brown, Jan Rudolph, René Steinbrügge, A Graf, M Leutenegger, S Epp, Sita Eberle, Katharina Kubicek, Volkhard Mäckel, M Simon, Elmar Träbert, E Magee, C Beilmann, N Hell, S Schippers, Alfred Müller, S Kahn, A Surzhykov, and José Crespo López-Urrutia. "An unexpectedly low oscillator strength as the origin of the Fe XVII emission problem". In: *Nature* 492 (Dec. 2012), pp. 225–8. DOI: 10.1038/nature11627.

[35] Steffen Kühn et al. "High Resolution Photoexcitation Measurements Exacerbate the Long-Standing Fe XVII Oscillator Strength Problem". In: *Phys. Rev. Lett.* 124 (22 June 2020), p. 225001. DOI: 10.1103/PhysRevLett.124.225001. URL: https://link.aps.org/doi/10.1103/PhysRevLett.124.225001.

[36] M. Togawa et al. "Observation of strong two-electron–one-photon transitions in few-electron ions". In: *Phys. Rev. A* 102 (5 Nov. 2020), p. 052831. DOI: 10.1103/PhysRevA.102.052831. URL: https://link.aps.org/doi/10.1103/PhysRevA.102.052831.

[37] J. N. Eckstein, A. I. Ferguson, and T. W. Hänsch. "High-Resolution Two-Photon Spectroscopy with Picosecond Light Pulses". In: *Phys. Rev. Lett.* 40 (13 Mar. 1978), pp. 847–850. DOI: 10.1103/PhysRevLett.40.847. URL: https://link.aps.org/doi/10.1103/PhysRevLett.40.847.

[38] David J. Jones, Scott A. Diddams, Jinendra K. Ranka, Andrew Stentz, Robert S. Windeler, John L. Hall, and Steven T. Cundiff. "Carrier-Envelope Phase Control of Femtosecond Mode-Locked Lasers and Direct Optical Frequency Synthesis". In: *Science* 288.5466 (2000), pp. 635–639. ISSN: 0036-8075. DOI: 10.1126/science.288.5466.635. eprint: https://science.sciencemag.org/content/288/5466/635.full.pdf. URL: https://science.sciencemag.org/content/288/5466/635.

[39] R. Holzwarth, Th. Udem, T. W. Hänsch, J. C. Knight, W. J. Wadsworth, and P. St. J. Russell. "Optical Frequency Synthesizer for Precision Spectroscopy". In: *Phys. Rev. Lett.* 85 (11 Sept. 2000), pp. 2264–2267. DOI: 10.1103/PhysRevLett.85.2264. URL: https://link.aps.org/doi/10.1103/PhysRevLett.85.2264.

[40] R. Jason Jones, Kevin D. Moll, Michael J. Thorpe, and Jun Ye. "Phase-Coherent Frequency Combs in the Vacuum Ultraviolet via High-Harmonic Generation inside a Femtosecond Enhancement Cavity". In: *Phys. Rev. Lett.* 94 (19 May 2005), p. 193201. DOI: 10.1103/PhysRevLett.94.193201. URL: https://link.aps.org/doi/10.1103/PhysRevLett.94.193201.

[41] Jeffrey L. Krause, Kenneth J. Schafer, and Kenneth C. Kulander. "High-order harmonic generation from atoms and ions in the high intensity regime". In: *Phys. Rev. Lett.* 68 (24 June 1992), pp. 3535–3538. DOI: 10.1103/PhysRevLett.68.3535. URL: https://link.aps.org/doi/10.1103/PhysRevLett.68.3535.

[42] J. Nauta, J.-H. Oelmann, A. Borodin, A. Ackermann, P. Knauer, I. S. Muhammad, R. Pappenberger, T. Pfeifer, and J. R. Crespo López-Urrutia. "XUV frequency comb production with an astigmatism-compensated enhancement cavity". In: *Optics Express* 29.2 (Jan. 2021), p. 2624. ISSN: 1094-4087. DOI: 10.1364/oe.414987. URL: http://dx.doi.org/10.1364/OE.414987.

[43] Eric Black. "An introduction to Pound?Drever?Hall laser frequency stabilization". In: *American Journal of Physics* 69 (Jan. 2001), pp. 79–87. DOI: 10.1119/1.1286663.

[44] R. L. Barger, M.S. Sorem, and J.L. Hall. "Frequency stabilization of a cw dye laser". In: *Applied Physics Letters* 22.11 (1973), pp. 573–575. DOI: 10.1063/1.1654513. eprint: https://doi.org/10.1063/1.1654513. URL: https://doi.org/10.1063/1.1654513.

[45] R. W. P. Drever, J. L. Hall, F. V. Kowalski, J. Hough, G. M. Ford, A. J. Munley, and H. Ward. "Laser phase and frequency stabilization using an optical resonator". In: *Appl. Phys. B* 31.2 (1983), pp. 97–105. DOI: 10.1007/BF00702605.

[46] H. Nosato, Y. Kasai, M. Murakawa, T. Itatani, and T. Higuchi. "Automatic adjustments of a femtosecond-pulses laser using genetic algorithms". In: 3 (2003), 2096–2101 Vol.3. DOI: 10.1109/CEC.2003.1299931.

[47] Florian Schepers. "Modal reconstruction of transverse mode-locked laser beams". In: (2020), 2096–2101 Vol.3. DOI: https://doi.org/10.1007/s00340-020-07513-5.

[48] Bahaa E A Saleh and Malvin Carl Teich. *Fundamentals of photonics; 3rd ed.* Wiley series in pure and applied optics. New York, NY: Wiley, 2019.

[49] Janko Nauta. *An extreme-ultraviolet frequency comb enabling frequency metrology with highly charged ions*. Heidelberg, 2020. URL: http://archiv.ub.uni-heidelberg.de/volltextserver/28798/.

[50] Arthur K Mills, T J Hammond, Matthew H C Lam, and David J Jones. "XUV frequency combs via femtosecond enhancement cavities". In: *Journal of Physics B: Atomic, Molecular and Optical Physics* 45.14 (July 2012), p. 142001. DOI: 10.1088/0953-4075/45/14/142001. URL: https://doi.org/10.1088/0953-4075/45/14/142001.

[51] Stuart Russell. *Künstliche Intelligenz; 3rd ed.* 2012. ISBN: 978-3-86894-098-5.

[52] Patrick Knauer. *Alignment Optimization Webapp*. https://git.mpi-hd.mpg.de/XUV-Spectroscopy/Cavity-Alignment-Webapp. 2021.

Statement

I declare that this thesis has been composed solely by myself and that it has not been submitted, in whole or in part, in any previous application for a degree. Except where stated otherwise by reference or acknowledgment, the work presented is entirely my own.

Heidelberg, April 29, 2021 Patrick Arthur Knauer